FIELD INDUCED HOT ELECTRON EMISSION FROM COMPOSITE METAL-INSULATOR-METAL MICROSTRUCTURES

Ningsheng Xu, BSc

A Thesis submitted for the Degree
of Doctor of Philosophy

Aston University

September, 1986

ASTON UNIVERSITY

FIELD INDUCED HOT ELECTRON EMISSION FROM COMPOSITE METAL-INSULATOR-METAL MICROSTRUCTURES

Ningsheng Xu, BSc

A Thesis submitted for the Degree of Doctor of Philosophy, 1986

SUMMARY

An investigation has been undertaken into the physical process of field-induced hot-electron emission (FIHEE) from composite metal-insulator-metal (MIM) microstructures on the surface of vacuum-insulated, high-voltage, broad-area electrodes. In particular, a field electron emission imaging technique has shown that there are two types of emission image; typically, 70% of sites give an array of diffuse spots, whilst the remainders have a segmental-like structure. Detailed studies have been made into the sites showing this segmental structure. A high resolution hemispherical spectrometer has shown that the energy distribution of electrons emitted from a single segment has a single-peak spectrum, where both the full-width at half maximum (FWHM) and the spectral shift below cathode Fermi level depend on the applied field and the choice of segment. A new spatially-resolved energy-selective analysis technique, based upon the high resolution spectrometer, has revealed: (i) the geometrical parameters of an image segment are field-dependent; (ii) the current density in a given segment has its maximum value at the sharply-defined convex edge; (iii) the energy distribution (FWHM and shift), measured at constant field, shows a spatial variation within a given segment. These findings are interpreted in terms of a qualitative emission model which assumes that MIM microstructures occur naturally on the surface of electrodes, and that field-induced hot electrons have to undergo a coherent scattering process at the edges of the top metal layer before being emitted into the vacuum. This model is shown to be further supported by simulation studies using "artificial" sites formed by graphitic carbon.

**Key words: Prebreakdown electron emission.
High-voltage vacuum insulation.
Field induced hot electron emission.
Electron spectrometry.**

CONTENTS

LIST OF FIGURES

Figure No. **Page No.**

LIST OF TABLES

CHAPTER ONE

INTRODUCTION

1.1. The limitation of vacuum for insulating high voltage

The high-voltage (HV) vacuum-insulation capability of broad-area electrodes is an important technological consideration in the design of a wide variety of devices and instruments, e.g. X-ray tubes, RF resonance cavities, power vacuum switches, electron microscopes, particle accelerators and separators etc. [1]. Generally speaking, the performance of a HV gap is limited by an operational risk of "sparking" or "arcing" between two electrodes; this phenomenon is known as "breakdown", where the gap resistance effectively falls to zero. For some devices, a breakdown event is an irreversible process resulting in permanent electrode damage and degradation in the performance of the gap. In other applications, although the disaster may be avoided, the precautions that have to be taken are generally very expensive [1]. Thus, solving the breakdown problem is of very great technological importance, and consequently there have been many research programmes directed towards understanding the fundamental physical processes that give rise to a breakdown event [1,2].

It is now believed that for gaps < 5 mm and fields of 10-30 MV/m and under ultra-high vacuum conditions, the initiation of a breakdown event is associated with "prebreakdown" current [1,2]. In fact, the prebeakdown current has been shown to arise from a localized electron emission process and this thesis is focussed on a fundamental study of the physical origin of this prebreakdown electron emission phenomenon.

1.2. "Cold" metallic electron emission versus field-induced "hot" electron emission

Up to a decade ago, prebreakdown currents were attributed to the quantum mechanical "cold" metallic electron emission mechanism analysed by Fowler and Nordheim [3]. However, to apply this model it was neccessary to assume the exsistence of isolated microprotrusions or whiskers on the surface of broad-area electrodes; i.e. in order to explain how the emission could occur at anomalously low macroscopic gap fields of 10-30 MV/m [4,5]. The strongest evidence in favour of this model was the fact that the externally measured current-voltage characteristic of a vacuum gap generally gave a linear Fowler-Nordheim (F.N.) plot, whose slope provided a means of estimating the geometrical field enhancement factor β of the associated microprotrusion. Significantly though, it was freqently noted that such plots predicted unrealistically high β-factors [1]: on the technological level, it was also noted that electrode polishing rarely had the desired effect of removing the supposed microprotrusions.

As will be discussed in chapters 2 and 3, the last decade has seen more and more direct evidence which appears to contradict the above model. In particular in situ scanning electron microscopy studies [5] have failed to reveal any surface features of the type that would be neccessary to give rise to the sort of high local field enhancement factor β (~ 100-1000) required by the microprotrusion model. In contrast, both the experimental findings and theoretical considerations suggested that the emission process had "non-metallic" rather than "metallic" properties. On the basis of this early evidence it was proposed that the emission stemmed from a field-induced hot electron emission (FIHEE) mechanism that was associated with insulating inclusions or particles on the surface of electrodes [1]. However, a great deal of more recent experimental evidence, which will be presented in chapters 3 and 5, suggests that there exist emission regimes other than that assumed by this early model. In particular, a more sophisticated micropoint anode probe technique due to Fischer and co-workers [6], incorporated with a scanning Auger probe and scanning electron microscopy facilities, has revealed that an emission site often contains foreign metallic element, although the superficial structure appears to be insulated from the metallic substrate. A field emission imaging technique incorporating a new spatially resolved spectral analysis capability (see chapter 4) has also shown that there are two types of emission image , which in turn, suggests that at least two kinds of emission regime might exist. This latter finding, and other complementary experimental results, will be fully described in chapter 5. An analysis of these experimental data is described in chapter 6, where it is suggested that a similar FIHEE mechanism operates at an alternative type of emission regime.

1.3. Experimental approaches

The experimental technique which has been used for the major part of this investigation is a field emission energy spectrometry. In common with its extensive application in studies of field emission from metals, semiconductors and absorbates on metals [7], where it has revealed many fundamental physical processes, the technique has similarly provided a great deal of valuable information about the physical mechanism operating at emission sites on the surface of broad-area electrodes (see chapters 2 and 3).

The facility used in this experimental research programme was particularly veratile, being based upon an UHV (< 10^{-10} mbar), high resolution (< 30 meV), hemispherical deflection electron energy analyzer, incorporating a field emission imaging system and an automatic specimen scanning system. With this system it was possible to mechanically probe the electron energy spectrum at any desired location in the emission image, and this capability provided important information about the emission process. By extending this principle to include an automated electronic image scanning facility, coupled with a selective tuning of the spectrometer, it has been possible to produce a new spatially-resolved energy-selective analysis technique. In particular, it has been possible to obtain a visual "picture" of how electrons of a given energy are spatially distributed over an emission image. This instrumental development represents a central contribution of the thesis, and the associated electron optical and electronic system will be fully described in chapter 4.

To supplement this basic analytical system, subsidiary systems have also been developed for studying the effects of photo and thermal stimulation on the emission process. These experiments are described in chapter 5, whilst the physical significance of the important findings that emerged from them will be considered in chapter 6.

1.4. Theoretical considerations

Two further important objectives of this thesis are (a) to provide a critical review of existing theories that have been proposed to explain the basic emission process, and (b) to indicate how they need to be refined, or changed, in order to account for the present experimental findings. Accordingly, chapter 3 presents three recently proposed models and the critical comments on them. Subsequently the electron-phonon interaction mechanisms, the coherent scattering phenomenon of hot electrons at the edge of the top metal electrode of a MIM microstructure and the related theory are discussed [8]. Having provided a framework for discussion, chapter 6 considers how the present data can be best interpreted. In particular, it is assumed that there are MIM microstructures that occur naturally on the surface of high-voltage electrodes. After a switch-on process, permanent conducting channels are assumed to be electroformed in the insulating layer, which bridge the top metal layer and the underlying metal substrate and promote a field-induced hot electron mechanism similar to that proposed by Latham et al [9]. Hot electrons generated within the high field region in the insulating medium close to the top metal layer have to undergo a coherent scattering process in the top metal layer of a metal-insulator-vacuum triple junction in order to escape into vacuum. As a result, they give rise to a characteristic type of emission image that consists of arc-like elements, i.e., similar to that found by Simmons et al [8] with purpose-fabricated MIM devices. Thus, the top metal layer will be "transparent" to these electrons. On the other hand, there will also exist electrons that experience incoherent scattering processes in the top metal layer, but may nevertheless still be field emitted into vacuum. Consequently, the associated electron energy spectra have been shown to share many of the characteristics found for the MIV emission regime [9].

CHAPTER TWO

PREBREAKDOWN ELECTRON EMISSION FROM VACUUM-INSULATED HIGH-VOLTAGE ELECTRODES

In this chapter we shall review some of the more important experimental findings that have recently emerged from studies of the prebreakdown conduction phenomenon: more extensive details and references can be found either in the book by Latham [1] or in the review of Noer [2]. From this review, we shall see how a field-induced hot-electron emission mechanism, associated with some form of composite microstructure is thought to be responsible for the prebreakdown electron emission.

2.1. Experimental evidence of metallic microprotrusion hypothesis

Experiments on extended-area electrodes began at the turn of this century. From the early work, particularly that of Millikan and co-workers [10,11], it was shown for example that field electron emission could be obtained from a tungsten electrode in a rather poor vaccum system with fields ranging from 1 to 5 x 10^7 V/m, but after annealing at 2700 K, the cooled cathode could withstand a field of 4 x 10^8 V/m. Furthermore, light spots were also observed on the anode, which suggested that the electron emission originated from a few localized cathode sites. From these observations, Millikan concluded that the emission came from localised regions of the cathode having either a low work function, due to chemical impurities, or where there was a high local field produced by surface roughness.

With the introduction of ultra high vacuum (UHV) techniques, a cathode surface could be more clearly defined by eliminating the contamination from either the vacuum system or residual gases. The birth of the Fowler-Nordheim theory [3] also greatly influenced the thinking about the field emission phenomenon. This theory, which will be discussed in detail in the next chapter, applies quantum mechanical concepts to explain field electron emission from ideal metal surface;

namely by assuming that an electron tunnels from the metal through the surface potential barrier into the vacuum. For tunnelling to occur, theory needs a minimum field of ~3×10^9 V/m, in order to obtain a surface barrier with a width that is comparable to the electron wavelength in the metal. The theory also predicts that a plot of ln (I/F^2) versus $1/F$ (conventionally referred to as a F.N. plot) will be a straight line, where I is the emission current and F is the applied field. For non-planar electrode geometries, it was necessary to introduce a field enhancement factor β to describe the microscopic surface field F over the emission area: thus $F = \beta(V/D)$, where D is a gap spacing between anode and cathode, and V is the voltage applied between them. Thus a F.N. plot will have a slope whose value is inversely proportional to β, and an intercept that is dependent upon $\ln(A_e\beta^2)$, where A_e is the emitting area. Boyle et al [12], in particular, tried to experimentally confirm these predictions using a crossed wire electrode geometry in UHV, and found that their results gave a good straight line fit to a F.N. plot, although the field enhancement factor β was unexpectedly found to vary with the electrode gap spacing. Neverthless they found that their experimental findings were shown to be broadly consistent with an explanation based on the presence of a small metal protrusion on the cathode surface.

Little & Smith [13] and Tomasche & Alpert [14] obtained further evidence that apparently supported the microprotrusion hypothesis, by directly observing the profile of an electrode surface using a transmission electron microscope. Little and co-workers [13,15] showed that for a range of electrode materials, including tungsten, aluminium, stainless steel, Kovar, nickel, silver and copper, "used" cathode surface, as seen in profile electron micrographs, were typically found to have wiskers which could give high enough β factors for F.N. type of field emission to occur: significantly, no such features were observed before the application of an electric field. They also noted that the emission was independent of temperature up to ~1000 K, and independent of illumination with visible light, which were assumed to verify that the emission did not originate from areas having an extremely low work function.

2.2. Experimental evidence against the metallic microprotrusion hypothesis

As new experimental techniques have been developed, a great variety of effects have been observed that are at odds with the microprotrusion hypothesis. Amongst these are: the curved and variable nature of F.N. plots, the switch-on, the characteristic noise and instabilities of prebreakdown currents, the variations of current over extended time intervals, the ignition-hysteresis phenomenon, as reported by Powell and Chatterton [16] and microdischarges [17]. In particular, Cox [18] and Hurley [19] reported on examples of electrode combinations that gave non-linear Fowler-Nordheim current-field relationships. Cox [18] made a large number of tests on 14 mm diameter copper-chromium alloy vacuum switch contacts which were set 6 mm apart to form a plane-paralled gap and under a vacuum of 2×10^{-10} mbar. He found that about 1% of tests produced unstable emission with the irreversible hysteresis-like I-V characteristics illustrated in figures 2.1 and 2.2. Hurley's work on O.F.H.C. copper, using a pointed anode probe [19], showed the existence of two types of site which he termed "a" and "b" sites. The "a" sites generally gave straightline F.N. plots and produced breakdown and resultant site destruction for currents $> 5 \times 10^{-5}$ A. The "b" sites, on the other hand, were characterized by their negative resistance, shown by the I-V plot of figure 2.3. With these sites, breakdown could occur

Fig. 2.1 An I-V plot showing the irreversible "hysteresis-like" characteristic. (from Cox [18]).

---

randomly in a current range of 10^{-5} to 10^{-3} A without destruction of the emitting site.

Strong evidence against the metallic microprotrusion model was also provided by Cox et al [20,21], who developed an anode probe hole technique for locating emission sites on a broad-area electrode

Fig. 2.2 Fowler-Nordheim and Richardson-Schottky plots of the I-V data represented in figure 2.1. (from Cox [18]).

---

surface. By scanning the cathode with respect to the anode probe hole, each site position could be determined to an accuracy of 0.1 mm in the initial attempt [20], and to 10 μm in the refined technique incorporated within a S.E.M. [21]. A notable early finding of the technique involved the use of a simulated site consisting of a tungsten tip embedded in an extended planar copper surface [20], where the emission was found to originate from a position close to, but definitely separated from the artificial protrusion. Later, in an UHV S.E.M., the important technological finding emerged that dust particles are frequently the cause of many emission centres. Furthermore, it was shown that these could largely be prevented by setting up a specimen from cleaning bath situated right next to the S.E.M. that was itself located in a clean room. Subsequently, sites were found at cracks or grain boundaries, as shown in figure 2.4, or at the specimen edge: this latter occurence was despite attempts at reducing field enhancement near the specimen edges by profiling the electrodes [21]. However, the study did not reveal any surface micro-features of a particle associated with emission that could result in the field enhancement factor predicted by a F.N. plot.

From this evidence, it was concluded that the metallic microprotrusion model could not provide an adequate explanation of the emission phenomenon. Furthermore, the evidence suggested that mechanisms could be operating at emission sites that might be more complicated than those assumed by the simple F.N. theory. Accordingly, several new dedicated analytical studies, described in the following section, were initiated to obtain more precise information about the material nature of emission sites and the associated emission mechanism.

2.3. Experimental evidence of non-metallic emission from insulating inclusions

From this new generation of experiments, the work of Cox [21],

Fig. 2.3 I-V characteristics of typical b sites. (from Hurley [19]).

Fig. 2.4 A map of the emission current in the anode plane and SEM photograph showing the emitting area. (from Cox [21]).

Hurley & Dooley [22,23], Allen & Latham [24], Athwal & Latham [5,25,26], Bayliss & Latham [9] and Fischer & Niedermann [27], in particular, provided a deverse body of evidence in favour of a non-metallic emission mechanism associated with insulating-like particles. Thus, as described above, the first interesting experiment resulted from the anode probe hole technique of Cox [21] for the direct identification of an emission site in a S.E.M. Another approach that has been very successful in directly identifying emission sites in a S.E.M is the micropoint anode technique of Athwal & Latham [25]. The principle of this technique is to systematically scan the anode probe set a certain gap from a broad-area electrode for detecting an emission site. By using gradually finer anode tips, the resolution of the technique could reach 3-4 μm, and with the aid of a built-in X-ray spectroscopy capability, it was possible to obtain information about the topographical nature and chemical composition of emitting particles. Thus, a range of elements, including Al, Au and Ag were identified as being associated with these structures. As can be seen from figure 2.5, emitting particles typically appear bright seen under the S.E.M., which suggested that they might be composed of insulating oxide compounds; however, this was only speculation since the X-ray spectroscopic technique was unable to identify oxygen. As with the technique of Cox [21], this study again found no evidence of sharp metallic emitters: in fact, in a control experiment it was shown that electrons were preferentially emitted from particles even in the presence of deliberatly created metallic asperities [25].

More recently, Niedermann et al [27] have employed this micropoint anode technique in their advanced field emission surface analytical facility and obtained some very interesting results from the studies on extended area niobium cathodes. Thus, they have conclusively

Fig. 2.5 A scanning electron micrograph showing an emitting particle (i.e. that, within the marked circle, has bright appearance). (from Athwal & Latham [25]).

An open-shutter photograph of an electrically stressed planar high voltage gap showing both anode and cathode spots. Also shown arrowed are flares and discharge tracks emanating from cathode-spots.

Fig. 2.6 "K" spots of light and discharge tracks. (from Hurley & Dooley [23]).

confirmed that the electron emission is associated with the presence of anomalous particles, or inclusions, on the cathode surface. Also, with a high resolution scanning Auger electron probe, they have identified a range of chemical elements, in particular, oxygen and carbon which could not be identified by X-ray spectrometry technique used by Athwal & Latham [25]. With an UHV pre-preparation chamber, including an in-situ specimen heating facility, they have demonstrated that emission sites are destroyed by heat treatment, and have been able to produce well-defined, field emission free surfaces up to fields > 100 MV/m that have proved ideal for simulation studies. This work has also revealed that, under certain conditions, accumulation of carbon and sulphur can produce strong emission. Further details of these findings will be presented in the next section.

A different type of experimental approach to the study of other physical processes associated with emission sites was carried out by Hurley & Dooley [22,23]. They investigated the spots of light which could appear on cathode surfaces when a prebreakdown current was flowing (see figure 2.6); i.e. the same phenomenon that was briefly noted by Klyarfell and Pokrovskya-soboleva [28]. The typical optical spectrum obtained from a cathode spot is shown in figure 2.7, and was attributed by the authors to electroluminescence produced by the action of the electric field on semiconducting or insulating surface inclusions. This was confirmed by measureing the variation of emitted light intensity with the applied-voltage, and showing that this followed the Alfrey-Taylor law which is characteristic of electroluminescent cells [29]. In a later experiment, Hurley [30] directly demonstrated that electron emitting sites on copper electrodes were in fact the source of the electroluminescence.

The electron spectroscopy studies reported by Allen & Latham [24], Spectrum of light emitted from a single cathode spot: 4·8 mm gap, 61 kV DC.

Fig. 2.7 The spectrum of light from a cathode spot. (from Hurley [22]).

Electron energy spectrum obtained from (i) a reference tungsten emitter and (ii) a site on a broad-area copper cathode. The position of the Fermi level (FL) of each emitter is also shown. Electron energy in eV, 0·2 eV/div, is *x* axis (going from high energy to low energy left to right). Electron current per unit energy is *y* axis.

Fig. 2.8 Electron energy distributions of a reference tungsten emitter and of an emission site on the surface of broad-area electrdes. (from Allen & Latham [24]).

Athwal & Latham [25,26], and Bayliss & Latham [9] represent the most comprehensive experimental investigation into the physical origin of prebreakdown electron emission. The earliest, and probably the most important result is reproduced in figure 2.8, and revealed several important differences between the F.E.E.D. of clean metallic emitter (shown in figure 2.8i) and that obtained from a typical broad-area emitter. Thus,

a) all electrons are emitted from electronic states that are well bellow the cathode Fermi level,

b) the half width (F.W.H.M.) is considerably broader than for the metallic emission processes,

c) the spectrum is more symmetrical, i.e. lacking the sharp high energy edge which characterises the metallic F.E.E.D´s, and

d) spectra frequently exhibited a multi-peak structure.

Later, Athwal & Latham [25] found that the spectral shift and the half width are both strongly field-dependent.

In more recent experiments, which included an emission imaging technique, Bayliss & Latham [9,31,32] showed firstly that an emission site is often composed of several distinct electron sources, or sub-sites, (see figure 2.9). Secondly, it was found that the electron energy spectra measured from any sub-site is single-peaked, such as shown in figure 2.10, and has properties that closely resemble those reported earlier by Athwal & Latham (see figure 2.11). It is also noted that an I-V plot of a sub-site revealed a characeristic that has a contact-bulk limited transition. All of these findings provided both strong experimental evidence against a simple metallic emission model and much new information about physical process operating at the typical emission regime. In fact, they led to an energy band model which was able to explain most of the well known properties of

Fig. 2.9 An emission image of a site. (from Bayliss & Latham [9]).

Fig. 2.10 A sequence of electron spectra of a sub-spot. (from Bayliss & Latham [9]).

---

prebreadown emission current in terms of a hot electron mechanism that occured at a localized site involving a MIV (metal-insulator-vacuum) micro-regime. The most recent and sophisticated form of this model will be discussed in more detail in a coming chapter.

Aston University

Illustration removed for copyright restrictions

Fig. 2.11 (a) The variation of the spectral shift (S) and half width (f) with applied field. (b) The F.N. plot of a sub-site. (from Bayliss & Latham [9]).

2.4. Experimental evidence of non-metallic emission involving particles other than insulating inclusions

As experimental techniques were refined, more and more experimental evidence was collected that strongly questioned whether all emission sites operate by the above MIV mechanism. For example, the micropoint anode probe study of Athwal & Latham [5], already described above, had shown that an emitting particle frequently contained metallic elements but with its superficial structure being apparently electrically insulated from the substrate electrode. More recently, Niedermann et al [6,27] employed a similar technique, but incorporating a high resolution scanning Auger probe, in a detailed study of 12 sites on 8 niobium specimens which were prepared in different cleaning procedures. As shown in refs. 6 and 27, their results have again revealed that most emitting particles contain metallic elements, although they could not tell from their results whether these particles are wholly metallic or also include a subvolume of non-metallic material. Another Auger analysis of an emitting site was carried out by Bayliss [32], in which he used a high resolution mapping technique described in section 4.2.8, to firstly locate an emitting region. The specimen was then transported to a Kratos XSAM 800 Auger analysis facility, where the site was found to contain more than 40% of carbon, as seen from the Auger read-out tabulated below:

Element	% Concentration
S	2.54
Cl	3.29
C	44.22
O	11.89
Cu	38.06

These data were considered to indicate that the likely composition of the site was a mixture of a copper compound (mainly copper oxide) and carbon.

Experimental observations also exist which directly suggest that some emission regimes are associated with a MIMV (metal-insulator-metal-vacuum), rather than a MIV, microstructures. For example, during his experiment on an intentionally oxidized copper specimen, Bayliss [32] found that if a test electrode suffered a flash-over, there was a dramatic increase in the density of emission sites. This effect is illustrated by the "before" and "after" high resolution site maps of figure 2.12, which were recorded respectively at current levels of 4 μA and 40 μA with a same voltage of 6 kV. On the basis of an Auger analysis of the cathode surface, these sites are believed to be associated with "splashed" droplets of metallic anode material: it was also considered likely that the droplets would be insulated from the substrate cathode by the thick oxide layer. There is also evidence from studies of prebreakdown electron emission from broad-area high voltage electrodes that carbon, as an artificially deposited local impurity, can stimulate the emission of electrons at anomalously low fields. This effect was first reported by Athwal et al [33], who showed that a small pencil "dot" or a drop of colloidal graphite (Aquadag) of diameter of 0.2 mm could promote field emission at a gap field of as low as 4 MV/m. Furthermore, as can be seen from figure 2.13, the typical electron spectra measured from these sites are shown to have either a single or multi-peak structure. More important, however, the spectral peaks are seen to be shifted to energies below the cathode Fermi level, whilst the scanning electron microphotograph of figure 2.14 shows that, in common with naturally occuring sites, the emitting particles have a bright appearance; i.e.

Fig. 2.12 High-resolution maps of the emission site distribution recorded at a constant field of 12 MV/m "before" (a) and "after" (b) a flash-over event. (from Bayliss [32]).

---

suggesting that the emission regime involves some form of non-metallic blocking layer. Niedermann et al [32] have recently confirmed the above findings by depositing graphitic carbon particles onto the surface of an electrode which had been heat-treated, and was emission-

Single and multi-peak spectra successively recorded at (a) 7.2 MVm^{-1} and (b) 8.4 MVm^{-1} from an Aquadag site on a niobium electrode.

Fig. 2.13 Electron spectra of an artificial graphitic-carbon site. (from Athwal et al [33]).

Fig. 2.14 A scanning electron micrograph of a "pencil" site. (from Athwal et al [33]).

free up to field of 100 MV/m. As can be seen from a comparision of figure 15 (a) and (b), they were able to demostrate that every visible particle becomes strong emitting centre. It is also important to note that similar experimental results were obtained when graphitic carbon particles were deposited on an anodized cathode which had an oxide layer of thickness of 1300 Å.

The experimental results described above clearly demonstrate that carbon is frequently associated with an emitting site. In fact, there is a growing body of experimental evidence which suggests that carbon itself, in certain forms, is strongly emissive. In particular, filamentary carbon fibres have been extensively studied as micro-point field emission electron sources [35,36,37,38], and in the form of a felt weave, as extended cold-cathode electron sources [39]. Copious field emission has also been observed from bulk specimens of pyrolytic graphite [40]. There is also evidence from studies of prebreakdown electron emission from broad-area high voltage electrodes that carbon, as a localized impurity, can stimulate the emission of electrons in the same field range. For example, carbon was found by Niedermann et al [6] to be responsible for 20% of the emission sites found on an as-introduced niobium specimen and for many of the new sites created after annealing up to 800° C. In general, these latter sites were associated with carbon particles that "appeared" on the surface following annealing; however, even some non-emitting carbon particles that existed on the surface before the treatment also become emitting after annealing up to 800° C. In fact, it has been long known that carbon concentrations exist at grain boundaries on broad-area electrodes [41], or on a metal surface as a normal impurity [42]. Thus, it is not supprising that, during a heating process, they shall diffuse to the surface and accumulate as micron-sized particles.

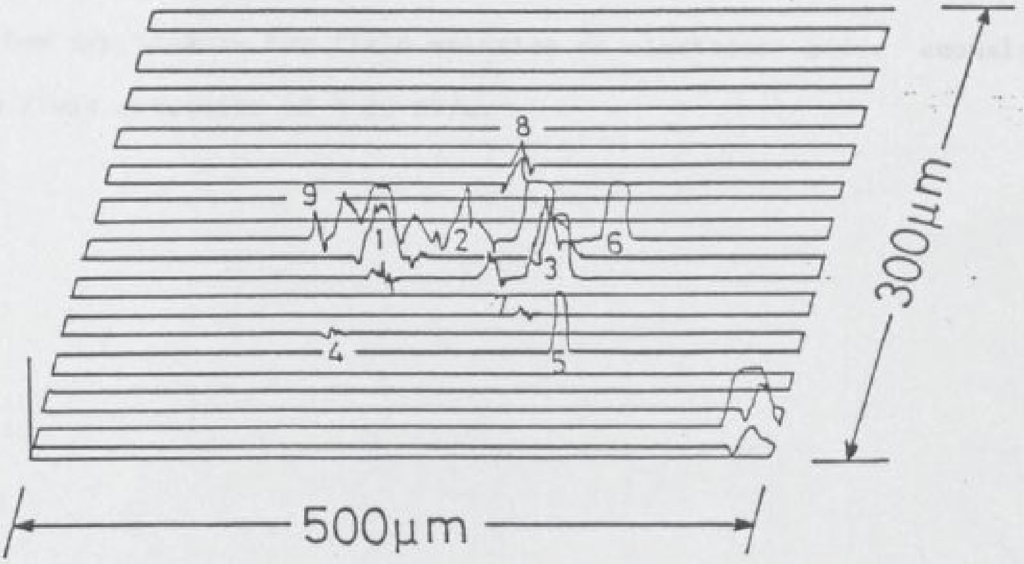

FIG. (a) High-resolution FE scan of region of deposit C7, pure Nb cathode. Maximum anode-cathode voltage 2 kV, d 20 µm.

FIG. (b) SEM photograph of the deposit where the FE scan of Fig. (a) was made, with the positions of emission sites indicated. (Numbers correspond to those on Fig. (a))

Fig. 2.15 The high resolution map of the emission site distribution and the SEM photograph of the graphitic carbon particles artificially deposited showing the corresponding positions of the sites andthe particles.(from Niedermann [27]).

However, it remains a very important question to investigate how carbon can promote the field emission of electrons under anomalously low field condition of 5-20 MV/m.

CHAPTER THREE

FIELD INDUCED "COLD" AND "HOT" ELECTRON EMISSION

In parallel with the development of experimental studies of the prebreakdown electron emission that have been described in last chapter, the theoretical understanding of the prebreakdown emission phenomenon has also been up-dated. Although the Fowler-Nordheim theory [3] was able to satisfactorily explain the experimental findings obtained for conventional metallic emission, it has not been found to provide an adequate account of the prebreakdown electron emission that originates from broad-area electrodes. Accordingly, several new models of the emission process have been recently introduced, and among these, the field-induced hot electron emission model in particular has been shown to successfully explain most of the existing experimental observations. Nevertheless, we shall, in this chapter, start with briefly reviewing the theoretical considerations relating to the metallic electron emission process embraced by the Fowler-Nordheim (F-N) theory: we shall then be in a position to compare its predictions with the experimental findings obtained from broad-area electrodes. Subsequently, other recent models that have been proposed to explain the physical origin of prebreakdown electron emission will be outlined and compared in their versaltility and sophistication with the field-induced hot electron FIHEE model. Finally, this FIHEE model will be further refined by taking a more fundamental physical account of the latest ideas on the behavious of hot electrons.

3.1. Conventional "metallic" field electron emission

3.1.1. The field emission from an ideal metal surface: the Fowler-Nordheim tunnelling model

Field electron emission from an ideal metal surface has been satisfatorily described by the Fowler-Nordheim theory, as fully derived either in the original paper [3] or in modern reviews such as those of Good & Müller [43] and Van Oostrom [44]. For the purpose of this thesis, it will be sufficient to only give a brief description of the theory, and quote its important conclusion, namely the Fowler-Nordheim FN equation.

In fact, the FN equation results from the application of quantum mechanics to a simple model consisting of an infinite atomically-clean metal surface that is subjected to a high external electric field. This physical picture can be illustrated as in figure 3.1, which represents the quantum mechanical tunnelling of electrons through the Schottky modified surface potential barrier [45]. It is also assumed, that within the metal, the "Free Electron" theory holds and the space outside the metal is vacuum. To derive a relation between the emission current density J and applied electric field F, Fermi-Dirac statistics is first applied to calculate the electron supply function $N(W_x)dW_x$, which is the flux of electrons incident on the surface that have normal energy components between W_x and $W_x + dW_x$. Secondly, the electron transmission coefficient $D(W_x)$, representing the probability of electrons being transmitting through the barrier is obtained by solving the Schrödinger equation using the WKB approximation [1,2,3]. Finally, the emitted electron density J is deduced by summing over all possible electron energies, i.e.

$$J = e\int_{\mathrm{all}\ E} D(W_x)N(W_x)dW_x \tag{3.1}$$

For temperatures of T < 300 K, the basic Fowler-Nordheim equation then is expressed in the form

$$J = \frac{1.54 \times 10^{-6} F^2}{\varphi\, t^2(y)} \exp\left[\frac{-6.83 \times 10^9 \varphi^{1.5} v(y)}{F}\right] \tag{3.2}$$

where F is the surface electric field and φ the work function of the

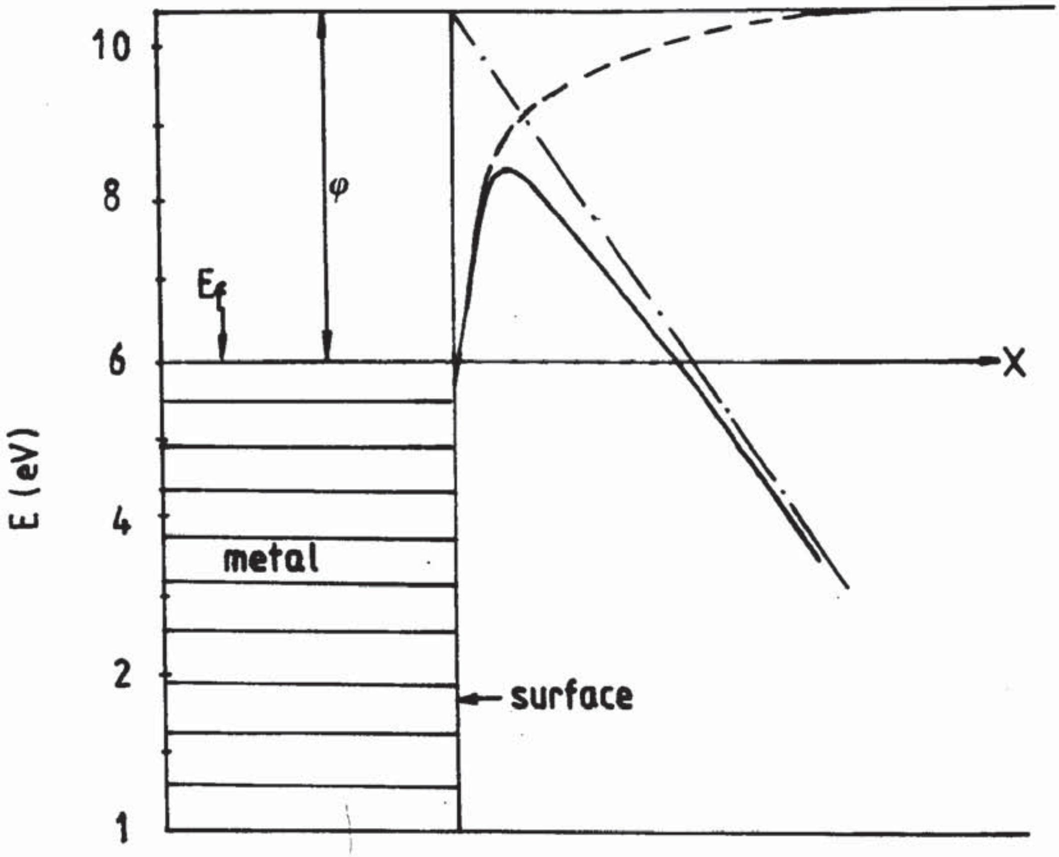

Fig. 3.1 A schematic representation of metallic field electron emission.

emitting surface; t(y) and v(y) are tabulated dimensionaless elliptic functions [43,44,46,47] of variable $y = 3.79 \times 10^{-5} \times F^{1/2}/\varphi$. For the stable range of emission currents, i.e. corresponding to $1 \times 10^{9} < F < 6 \times 10^{9}$ V/m, $t(y) \approx 1$ and $v(y) = 0.956 - 1.062y^2$. Substituting these approximations into equation 3.1, and rearranging, gives the most useful form of the FN equation, viz.

$$J = 1.54 \times 10^{-6} \left\{ \frac{10^{4.54\,\varphi^{-1/2}}}{\varphi} \right\} F^2 \exp\left[\frac{-6.53 \times 10^{9} \varphi^{3/2}}{F} \right] \quad (3.3).$$

However, in most practical emission regimes, particularly a broad-area electrode, the field is locally enhanced at some surface features (e.g. protrusions or wiskers) by a factor of β over the emitting area A_e. Therefore, for an uniform field over the emitting region

$$\beta = F_{mic}/F_{mac} \quad (3.4)$$

where F_{mic} is the locally enhanced field and F_{mac} is the macroscopic gap field. For a plane-parallel electrode gap, F_{mac}=V/D, where V is the potential difference applied between the anode and the cathode with a gap spacing D. Thus, for an enhanced emission from a plane cathode,

$$F_{mic} = \beta \frac{V}{D} \qquad (3.5).$$

Hence, the resulting emission current will be given by subsitituting F_{mic} and A_e into (3.3),

$$I = A_e \times 1.54 \times 10^{-6} \times \left\{ \frac{10^{4.54\,\varphi^{-1/2}}}{\varphi} \right\} \frac{(\beta V)^2}{D^2} \exp\left[\frac{-6.53 \times 10^{9} \varphi^{3/2} D}{V} \right] \qquad (3.6)$$

It follows that if the current-voltage characteristic of a gap with a single emitter is plotted in the form of ln (I/V^2) versus $(1/V)$, referred to as an F.N. plot, the result will be a straight line with slope

$$m = -6.53 \times 10^{9} \times \varphi^{3/2} \times (D/\beta) \qquad (3.7)$$

and intercept

$$c = \mathrm{In}\ 1.54 \times 10^{-6} \times \left[\frac{10^{4.54\,\varphi^{-1/2}}}{\varphi} \right] \frac{A_e \beta^2}{D^2} \qquad (3.8)$$

Thus, since D is known and φ of the emitter can be assumed to have the bulk metal value, the slope of the F.N. plot will give a measure of β factor of the emitter; this may then be substituted into equation 3.8 to determine the emitting area A_e. This forms the basis of the metallic microprotrusion model mentioned in last chapter.

3.1.2. The energy distribution of electrons field emitted from a clean metal surface

It is now known that all exerimentally measured energy spectra of field emitted electrons give the Total Energy distribution [48]. A theoretical derivation of this function has been made by Young [49] using the Free Electron theory. For this, he defined the following new parameters:

N(W,E)dWdE = Number of electrons incident upon the surface per unit area per second, with a total energy in the range E to E+dE, and having an x-energy component that is normal to a surface in the range W to W+dW,

P(W,E)dWdE = N(W,E)D(W)dWdE which is the number of electrons in the given energy ranges transmitted through the barrier.

where, the Total Energy distribution will be given by the following relation:

$$P(E)dE = \int_W WP(W,E)dWdE \qquad (3,9).$$

Young [49] showed that

$$P(E)dE = \frac{4\pi m D_p}{h^3} \exp(-c) \frac{\exp(E-E_f/D_p)dE}{1+\exp(E-E_f/K_b T)} \qquad (3.10),$$

where

$$c = \frac{4e^{1/2}(2m\varphi^3)^{1/2}}{3\hbar F} v(y) \qquad (3.11)$$

and

$$D_p = \frac{\hbar e^{1/2} F}{2(2m\varphi)^{1/2}} \frac{1}{t(y)} \qquad (3.12)$$

with the other parameters having the form previously defined, and where $E_f = -\varphi$. Both the Normal and Total energy distributions obtained by Young are shown in figure 3.2 for three different temperatures. It should also be noted that, under certain circumstances, the behaviour of electrons in metals do not obey the assumption of the Free Electron theory, and this sometimes is revealed

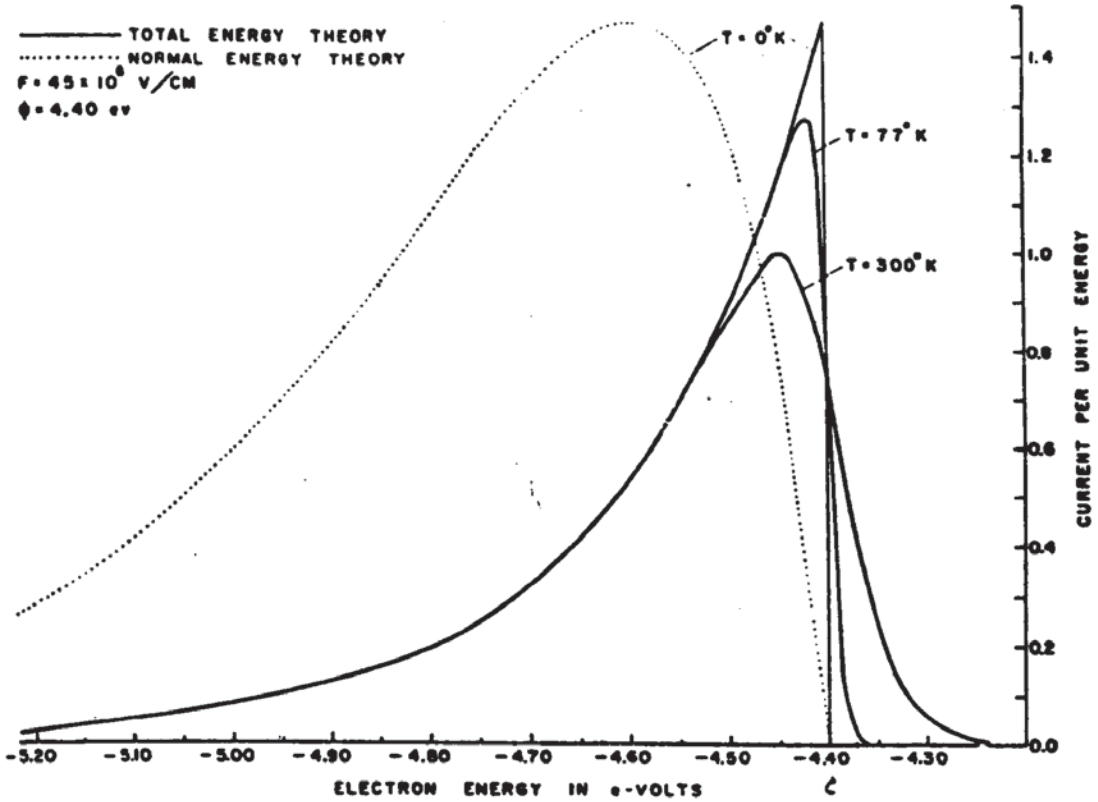

a) Total- and normal-energy distributions for field emitted electrons. The 300°K curve is arbitrarily normalized.

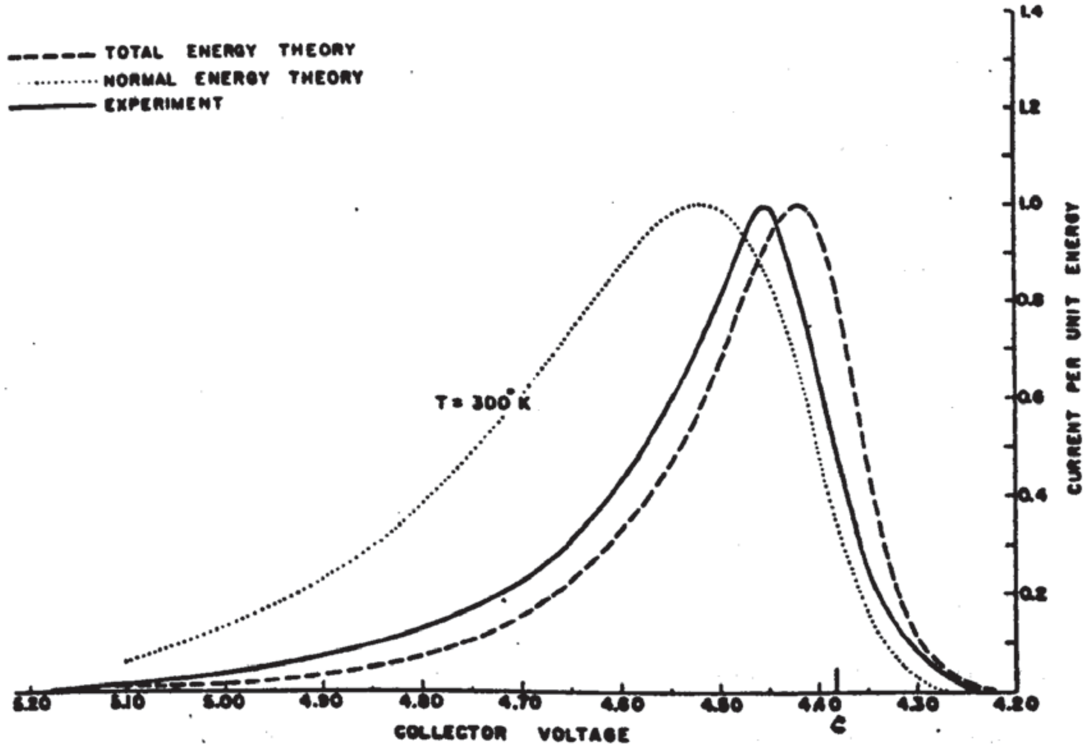

b) Theoretical and experimental total-energy distributions of field-emitted electrons at room temperature. The theoretical normal-energy distribution is shown for comparison. All three curves are arbitrarily normalized.

Fig. 3.2 Metallic Total and Normal Energy distributions.
((a) from Young and Müller [102], (b) from Young [49]).

in experiments. However, these phenomena will not be considered in further detail here, since they are beyound the interest of this programme; for the interested reader, the effects have been fully described by Modinos [7].

3.1.3. The field emission image obtained from a clean metal surface

Electrons field emitted from clean metal surface can be imaged using the diode arrangement shown in figure 3.3 where the phosphor-coated fluorescent screen doubles as the anode of the device. In order to obtain the very high fields necessary for field electron emission at low temperatures ($> 3 \times 10^9$ V/m), the emitting surface (cathode), must have a high curvature so that there is sufficient geometrical enhancement for emission to be obtained, when only a moderate voltage is applied between the cathode and the anode (i.e.the screen). For this purpose, field emitters are made from fine wires etched to a sharp tip with a radius of between 100 to 2000 Å. To obtain the high resolution, the screen must be curved, where for a typical emitter, one can readily achieve a resolution of ~25 Å. The magnification factor is proportional to the ratio of tip-screen distance,and the tip radius, and in practice is typically of the order of 10^5. This is the basis of the field emission microscope invented by Müller [50]. Since the principles of field emission microscopy, as well as many examples of its utility, can be found in a number of excellent review articles and books [43,51,52], we shall here only summarise the essential results obtained from field emission microscopy. A projection micrograph of a tungsten emitter, taken by Müller [53] is reproduced in figure 3.4, where the dark regions correspond to single-crystal planes of high work function (low emission) and the light regions to planes of low work function (high emission). The indexing of the planes can be established from the

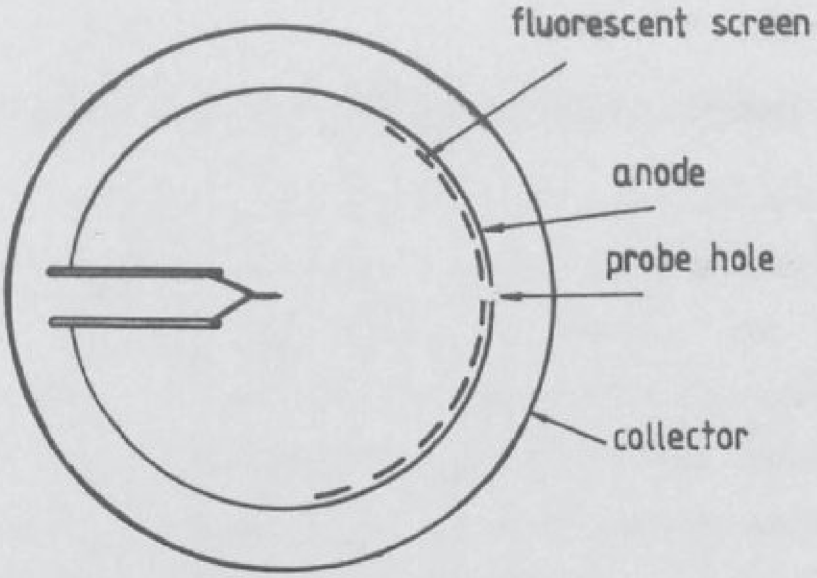

Fig. 3.3 The schematic illustration of a field emission diode.

Fig. 3.4 A projective image of field emitted electrons from clean metal emitter. (from Müller [53]).

---

symmetry of the pattern, which depends of course on the orientation of the tip (see [43], [51]). With a probe hole in the screen, which appears in figure 3.4 as a dark hole in the center of the (012) plane, electrons passing through this hole can be detected as a current by the collector (see figure 3.3). Therefore, the value of the emitted current density of the field-emitted electrons at any point of the image can, in principle, be determined by dividing the collected current by the size of the hole projected back onto the tip surface (see, for example, [54]).

3.2. Recently proposed models for prebreakdown electron emission

As experimental data has accumulated which apparently contradicts the metallic microprutrusion model, several alternative theoretical models have been proposed that attempt to explain the new experimental evidence. In particular, there is Hurley's filament model [55], Halbritter's dynamic field enhancement electron emission model [56] and Latham & co-workers' field-induced hot-electron emission model FIHEE [9,57,58]. Of these, the last model in its most recent sophistcated version [9], will form the basis of the discussion of the present experimental findings and therefore will be described in greatest detail.

3.2.1. The filament model

To explain the optical observations described in section 2.3, particularly the measurement of electroluminescence from emission sites, Hurley proposed his filament model [55]. This assumes that there are a number of semiconducting or insulating inclusions on the surface of electrodes, and that when the electrode is exposed to an electric field of 10-100 MV/m, local micro-regions of these inclusions experience an electroforming process similar to that suggested by Dearnaley et al [59]. The conductivity of the electroformed layer may be 10^8 times greater than their unformed state, and consequently the channel within the layer appears like a metallic filament embedded within the dielectric-like matrix of the surrouding inclusion (see figure 3.5.). The electroluminescence is then assumed to result either from the excitation of electrons to the conduction band by impact ionisation, or by some type of recombination process [60], or more likely, from the generation of hot carriers by acceleration

Production of electroluminescence, vacuum breakdown and electron emission from electroformed conducting filaments in oxide impurities. (*a*) Electroluminescence. (*b*) Vacuum breakdown. (*c*) Electron emission.

Fig. 3.5 Illustrations of phenomena associated with the filament model. (from Hurley [30]).

across weak high-resistance spots in the filaments [61]. With the latter mechanism, electrons may be accelerated to nearly the full potential difference existing across the semiconducting or insulating oxide layer, and may subsequently be scattered into the unformed surrounding oxide to produce the observed electroluminescence (figure 3.5a). The electron emission is assumed to occur from the tip of the formed conducting channels , since this regime will provide considerable local enhancement of the applied field at the surface of the impurity (figure 3.5c). A formed layer or channel can be switched between various conductivity states and, under certain conditions, this can lead to spontaneous heating with material being expelled from a given site to leave behind a crater as shown in figure 3.5b; such instabilities are also assumed to be the origin of microdischarge or breakdown events.

3.2.2. The dynamic field enhanced electron emission model

Recently, Halbritter [56] has proposed a dynamic enhanced electron emission model which assumes that there are low-density adsorbates like hydrocarbons on the surface of broad-area electrodes. It is further assumed that electrons will be trapped in such dielectric adsorbates at energy levels $E < \varphi$, and will be emitted stochastically out of the traps at electric fields $F \approx 10^6 - 10^7$ V/m [62]. These emitted electrons will then be heated through an energy of $e\Delta xF = \Delta E >> K_b T$ in the insulating adsorbate. To form stationally conducting clouds with $E \approx 1$eV in a field range $F_c \leqslant F < F_b$, where according to experimental findings from SiO_2, the possible values of F_c and F_b will be $\sim 10^8$ V/m and $\sim 10^9$ V/m respectively. These hot electrons subsequently cause impact ionization, yielding high conductivity states which can be switched on for $F > F_s$ without causing the destruction of the material. Thus, for $F \geqslant 10^6$ V/m, where permanent charges ensures that $\beta^* F = F^* > F$, electrons in the adsorbate are accelerated to $E \approx 1-10$ eV and electron attachment states are formed. The excited localized states then decay by the emission of electrons, photons and atoms, with the electron emission giving rise to positive charging, which enhances β^* to β^{**} in the region near to the surface of substrate electrode to cause electron tunelling from substrate into the adsorbate. However, only the fastest electrons penetrate through the surface barrier because of the positive charges in the adsorbate: the other electrons are slowed down and neutralize the positive charges. Thus the emission is pulsed, where the time constant t for the firing of the avalanche depends on the details of the switch-on process, the channel dimensions, and the electric field difference $\Delta F = F-F_s$, where a rough estimate is given by Halbritter to be nanosecond order for regions which are close to the metal (100 Å). Although this model apparently can account for some experimental observations, it is at present basically lacking in positive supporting evidence. Thus, recent experiments carried out by Niedermann et al [6] have shown that only in a very few instances is there a suspicion that hydrocarbon particles are responsible for emission processes. Furthermore, there appears to be no obvious experimental findings to indicate that there are a wide range of continuous trap states existing in the band gap of an insulator, i.e. as required by this model. Finally, its most important conclusion, viz. that there will be a pulsation of the enhanced emission, has not been experimentally observed.

3.2.3. The field-induced hot electron emission model

This model has been progressively developed by Latham and co-workers [9,57,58]. It is based upon a wide range of experimental measurements which includes, in particular, the energy distribution of electrons emitted from sites on the surface of broad-area electrodes, the S.E.M. evidence obtained from studies carried out with the micropoint anode probe technique [5] and the observation of emission images. The essential features of the most recent quantitative version of this model, which is fully described elsewhere by Bayliss & Latham [9], will now be summarised.

(i) The emission regime

The assumed structure of an emission site is illustrared in figure 3.6, from which it is seen to consist of some form of "foreign" dielectric-like surface inclusion, or an anomalously thick oxide aggregation having a dimension of ~0.1 - 1 μm in the direction of the applied field F; i.e. such that it can support a potential drop of 2-3 volts across it at typical macroscopic gap fields of 10-20 MV/m. This latter assumption is based upon direct evidence obtained from micropoint anode probe techniques [5,6], which have shown emitting particles typically to have this sort of dimension. In addition, the field emission imaging technique has shown that the electron emission associated with these features comes from one or more independent sub-sites, which suggests that there are generally one or more conduction channels within the dielectric which bridge the metal substrate and vacuum (see figure 3.6.).

(ii) The switch-on mechanism

As discussed by Halbritter [62], it is assumed that the surface inclusions are only partly crystalline and almost certainly impure, so that there will be a distribution of both trapping states and donor centres within the inclusions. A further requirement of the model is that under low field conditions, the metal-insulator interface forms a blocking contact (see figure 3.7.). It is assumed however that there will be one or more microscopic locations on this interface where the local electronic conditions present a favourable tunnelling contact, and it will be at these locations that electrons will first start tunnelling from the metal into the insulator under the influence of the external field. Such locations could be created, for example, by local concentration of impurity atoms in the insulator, which would provide the necessary donor centres to produce a marked band bending.

0.5 µm

A schematic representation of the emission régime showing the conducting channels in the insulating inclusion and the associated microscopic field enhancement.

Fig. 3.6 The emission regime of the early FIHEE model. (from Bayliss & Latham [9]).

Fig. 3.7 A sequence of band diagrams of the conduction channel illustrating the early switch-on mechanism. (from Bayliss & Latham [9]).

Under zero-field conditions, the energy band diagram of such a localized region will appear as shown in figure 3.7a; i.e. with a high internal field at the metal-insulator interface and a depletion region just within the insulator. When an external field is first applied, it can penetrate through the inclusion and reinforce the internal field at the MI contact, so that on increasing the external field to a threshold value, electrons can tunnel from the metal substrate into the conduction band of the insulator (see figure 3.7b). These electrons will eventually fill any empty traps within the insulator, with the result that its Fermi level will progressively move closer to the conduction band edge in response to the increased electron density in the insulator. A further increment of field will result in more electrons tunnelling from the metal, but because all the traps in the insulator are now full, these electrons will eventually accumulate close to the metal-vacuum interface; i.e. filling the surface states and creating a degenerate pool of cold electrons in the insulator conduction band. It follows that these electrons will screen the external field from the insulator, and so, as shown in figure 3.7c, the necessary interface condition for tunnelling will no longer be satisfied. However, further increments of field can lead to the situation shown in figure 3.7d, where an electron can tunnel into the conduction band of the insulator and be accelerated towards the insulator-vacuum region, and through scattering processes, will raise the effective temperature, T_e, of the electrons stored near the insulator interface. In fact, if T_e is high enough, it will be possible for electrons to be emitted "thermionically" over the reduced Schottky surface barrier.

For continuous emission, it is necessary for the system to experience a transition. Thus, as the electrons at the vacuum surface are preferentically emitted, the surface field will be greatly increased relative to the bulk field, with the result that the dynamic charge distribution will adjust itself to give the highest density a short distance into the insulator,i.e. as shown in figure 3.7e. The essential feature of this switch-on mechanism is that it does not require a permanent structural change in the channel region; rather, the channel path is essentially "memorized" by the system, and the surface charges remain so that an energy band configuration similar to that of figure 3.7d results immediately after the field is re-applied. It therefore follows that if the applied field is reduced to zero for a short time, and then re-applied, it is unlikely that a similar switch-on behaviour will be observed. It also follows directly from the model that it would be possible to reduce the applied field to well below its switch-on value before the emission current falls to zero.

The field distribution associated with an emitting conduction channel, i.e. as depicted in figure 3.7e, is shown in figure 3.8. From this, two field-enhancement factors may be defined as follow:β_1 refers to the ratio of the vacuum field immediately above the filament tip, F_{tip}, to the macroscopic electrode gap field, F_o, whilst β_2 is the ratios of the average field within the filament, F_{fil}, to the insulator field well away from the channel, F_{ins}. Thus,

$$\beta_1 = F_{tip}/F_o \qquad \text{and} \qquad \beta_2 = F_{fil}/F_{ins} ,$$

and since $F_{ins} = F_o/\epsilon$, one has

$$F_{tip}/F_{fil} = \epsilon(\beta_1/\beta_2).$$

This switch-on model is however not entirely consistent with the experimental observations. Firstly, under good vacuum condition, one finds that once a site switches on, it needs no further re-swith-on process, no matter how long the site is left in the vacuum. It is

Fig. 3.8 The schematic illustration of the field and potential distributions associated with an emitting channel (from Bayliss & Latham [9]).

therefore difficult to see how the proposed switching process can memorize the channel path for a very long time [63]. Secondly, even if this memorizing effect holds at room temperature, some of the electron traps and surface states would be expected to relax back to their pre-conduction empty state when a specimen is heated to 600° C [64]. These effects were not in fact observed during the thermal stimulated study described in chapter 5. Thirdly, if the memory effect holds, ion beam sputtering would be expected to neutralize the negative surface charges, and even those stored in the insulator-vacuum interface region, so that it is likely that a re-switch-on process would become necessary. However, ion beam sputtering experiments carried out either in this programme or by Bayliss [31] did not indicate this possibility.

(iii) The energy distribution of emitted electrons

A detailed energy band diagram of the "on" state of a channel is shown in figure 3.9. From this, it will be seen that the surface region of the insulator contains a dense accumulation of the stored electron gas, and could therefore be expected to have electronic properties that are similar to a metal. This situation, which corresponds to the high-field limit of thermionic emission, has been considered by Murphy and Good [65], although the analysis of these authors was unfortunately in terms of the normal energy distribution, P(W), whereas experimental spectra generally correspond to the total energy distribution, P(E). However the transmission coefficient, D(W), derived by Murphy and Good [65] remains valid, and this may be used in conjunction with the total energy supply function, N(W,E)dWdE, developed by Young [49] to give the required emitted-electron energy distribution,

$$P(E)dE = \int_{W=-\infty}^{W=E} D(W)N(W,E)dWdE \qquad (3.13).$$

Substituting from Murphy and Good [65],

$$D(W) = \frac{1}{1+\exp\ \{-\pi(F/a_1)^{-1/4}[1+(W/b)(F/a_1)^{-1/2}]\}} \qquad (3.14);$$

and from Young [49],

$$N(W,E)\ dE\ dW = \frac{4\pi m}{h^3}\frac{dE\ dW}{1+\exp[(E-E_F)/K_bT_e]} \qquad (3.15)$$

and integrating leads to

$$P(E)dE = \frac{4mb}{h^3}\left[\frac{F}{a_1}\right]^{3/4}\frac{\mathrm{In}\ \{1+\exp[\pi(F/a_1)^{-1/4}[1+(E/b)(F/a_1)^{-1/2}]\}}{1+\exp\ [(E-E_F/K_bT_e)]}dE \qquad (3.16).$$

A detailed band-diagram representation of the on state of a conducting channel. F.l., Fermi level; v.b., valence band; c.b., conducting band.

Fig. 3.9 The energy band-diagram of the on state of a conducting channel. (from Bayliss & Latham [9]).

In above equations, F corresponds to the microscopically enhanced surface field at the top of the emitting channel, E_f is the Fermi energy, T_e the temperature of the hot-electron population behind the surface barrier, and a_1 and b are constants given by

$$a_1 = \frac{m^2 e^2}{h^4 (4\pi\epsilon_o)^3} = 5.15 \times 10^{11} \mathrm{V/m} \qquad (3.17)$$

and

$$b = \frac{me^4}{h^2(4\pi\epsilon_o)^2} = 27.2 \text{ eV} \quad (3.18).$$

Also, the Fermi energy will be equal to $-\varphi$, the barrier height at the insulator-vacuum interface.

A further theoretical development of this model leads to the important spectral parameters

$$E_p = AK_bT_e - b\left[\frac{F}{a_1}\right]^{1/2} \quad (3.19)$$

and

$$f = \frac{K_bT_e[2.328\pi K_bT_e - 1.303b(F/a_1)^{3/4}]}{\pi K_bT_e - b(F/a_1)^{3/4}} \quad (3.20)$$

where E_p is the position of a spectrum peak relative to the substrate cathode Fermi level, while f is the full width at half maximum. The second equation indicates that f has the interesting property that it may either increase or descrease with increases F, depending on the relative rate of increase of T_e and F.

(iv) The emission current density

Making the same assumption as above, i.e. that the electronic properties of the surface region of the insulator are quasi-metallic, the emission current density will correspond to that given by Murphy and Good [65] for the high-field thermionic case, i.e.

$$J = \frac{4\pi me}{h^3} \; \frac{\pi/N}{\sin(\pi/N)} \; K_b{}^2T_e{}^2\exp\left[\frac{-(\varphi-b(F/a_1)^{1/2}}{K_bT_e}\right] \quad (3.21),$$

here N is defined as

$$N = \frac{K_bT_e}{b}\left[\frac{F}{a_1}\right]^{-3/4} \quad (3.22)$$

and is a factor determing the shape of the energy spectrum, which typically has values less than 1.6.

This current density will also be influenced by the electronic properties of both the metal-insulator contact junction and bulk material of the insulator. This will be manifested by a transition from contact-limited to bulk-limited conduction, as discussed by Simmons [66]. In the contact-limited region of a J-V characteristic, the current density J_t tunnelling through the metal-insulator contact junction will be given by an expression of the form [66]

$$J_t = \frac{5.56 \times 10^{-14}}{\epsilon^* \varphi} N_D \left(V_c + \varphi_m - \varphi_i\right) \exp\left\{-3.6 \times 10^{13} \left[\frac{\varphi^3 \epsilon^*}{N_D\left(V_c + \varphi_m - \varphi_i\right)}\right]^{1/2}\right\} \qquad (3.23)$$

where φ_m and φ_i are respectively the metal and insulator work functions, φ the contact barrier height, ϵ^* the high-frequency dielectric constant of the insulstor, N_D the donor density and V_c the potential appearing across the contact junction due to the applied field. This equation predicts a sharply rising dependence of the current on the applied voltage, and hence a rapidly falling contact resistance that is essentially independent of temperature. In the bulk-limited region, the current density for low-fields is given by [66]

$$J_o = e\mu \frac{V_b}{d} N_C \left[\frac{N_D}{N_T}\right]^{1/2} \exp\left[-\frac{E_D + E_T}{2K_b T_e}\right] \qquad (3.24),$$

where N_C is the effective density of states on the insulator, N_D the donor density, N_T the trap density, E_D and E_T the donor and trap energy levels respectively, μ the electron mobility and V_b the potential appearing across the bulk due to the applied field. This equation applies if $E_T > F_1 > E_D$, where F_1 is the Fermi level position, whilst all these energy levels are just beneath the insulator conduction band, and nearly all the electron traps are filled. However, for the high-field case, where the Poole-Frenkel effect operates (i.e. field-assisted thermal ionization of donors and traps), the bulk conductivity becomes field-dependent. Under these circumstances, the J-V relation may be expressed as

$$J = J_o \exp\left[\frac{e}{K_b T_e}\left(\frac{eV_b}{\pi \epsilon \epsilon_o d}\right)^{1/2}\right] \qquad (3.25),$$

or

$$J = J_o \exp\left[\frac{e}{2K_b T_e}\left(\frac{eV_b}{\pi \epsilon \epsilon_o d}\right)^{1/2}\right] \quad , \qquad (3.26)$$

depending upon the nature and position of the traps [66].

Now if the insulator contains a high donor density ($N_D > 10^{24} m^{-3}$) and a high trap density ($N_T > 10^{25} m^{-3}$), the depletion region will be very thin and its bulk conductivity will be low in spite of the high donor density. Under these conditions, a contact-limited to bulk-limited transition may be observed in the current-voltage characteristic [66]. The dominant term in the equation of the bulk-limited case will then arise from the Poole-Frenkel effect, and it is usual to illustrate this by plotting lnI versus $V^{1/2}$, which usually enables the contact- and bulk-limited regions to be clearly separated. It should be noted that the slope of the bulk-limited region then varies inversely proportional to $d^{1/2}$, where d is the insulator thickness.

As will be discussed below, this interpretation gives a generally satisfactory explanation of the experimental results. However, as can be seen from equations 3.25 or 26, the bulk region has a finite conductivity that is dependent of the field, suggesting that the emission current will not become saturated. However, experiments on a similar control emission regime, carried but by Mousa & Latham [67], have revealed that the emission current eventually reaches a

Fig. 3.10 The current-voltage characteristic of a composite emitter. (from Latham & Mousa [67]).

---

saturation stage (see figure 3.10). This observation suggests that there may be another mechanism other than the Poole-Frenkel effect operating within the bulk region; a possibility that will be discussed in the next section.

(v) The hot-electron temperature T_e.

Referring to figure 3.9, the insulator surface potential at a conduction channel is give by

$$\frac{d\beta_2}{D\epsilon}V_o + \varphi_m - \varphi_i - V^* \qquad (3.27)$$

where D is the electrode gap width, V_o the applied voltage across the gap, whilst V^* repersents the effect of the stored negative charge, which may be assumed to the constant for moderate changes in the applied field. These negative charges are assumed to be trapped (a) throughout the bulk of the insulator, (b) in vacuum surface states, and (c) probably at the bottom of the conduction band, where the vacuum barrier is too wide for electron tunnelling to occur. The difference in energy ΔV (in electron volts) between the conduction-band edge at the vacuum surface and the metal Fermi level is now given from the geometry of figure 3.9 as

$$\Delta V = \frac{d\beta_2}{D\epsilon} V_o + \chi - \varphi_1 - V^* \qquad (3.28)$$

where χ is the insulator electron affinity. Most electrons lose an energy S (in electronvolts) in traversing the insulator contact and bulk regions, where S is the measured displacement of the spectral peak from the metal Fermi level. Therefore, the energy available for generating hot electrons near the vacuum surface will be

$$\Delta E = \Delta V - S \qquad (3.29)$$

where ΔE is measured from the bottom of the conduction band at the vacuum interface. However, a large proportion of this energy will be lost as the electrons react with the insulator lattice in an attempt to thermalize down to the lattice temperature, T_o. Thus, assuming that the hot-electron temperature is approximately a linear function of ΔE, we have

$$(K_b/e)\ (T_e - T_o) = \alpha \Delta E \qquad (3.30)$$

where α is, at present, an unknown constant. Substitution of (3.28) and (3.29) into (3.30) then yields

$$K_b T_e/e = [\ (d\beta_2/D\epsilon)\ V_o - S + \chi - \varphi_1 - V^*] + K_b T_o/e \qquad (3.31).$$

This consideration is still based upon the approach adopted by Latham [113]; i.e. that the hot-electron temperature is assumed to be a linear function of ΔE. Although this may give an good fit to the experimental results, it is only a good approximation in the situation where this potential only drops within a distance of the electron mean free path. For the insulator-vacuum region (-50 nm) assumed by the model, the electrons have to travel over a distance of several times of their mean free path, so that they will eventually lose their energy through the lattice scattering process. The model has taken this into account by adding a "loss factor" α to equation 3.30, but it does not provide a clear physical picture showing how electrons become "heated" and how they lose their energy. For this reason, it has been pointed out [68] that, under the field condition assumed by the model, hot electrons are unlikely. In fact, there are reasons to believe that the generation of hot electrons, and their energy loss mechanism in the solid state materials, may eventually be shown to involve more complicated scattering process. In order to enrich the existing model, a following section will present some theoretical considerations of these processes, so that a qualitative explanation can be given.

(vi) The unified emission equations

Finally, the model leads to the following three expressions that provide a basis for interpreting experimental data.

Firstly, the spectral half width f will have following relation with V_o and S:

$$f/5.47 = \alpha[BV_o - S] + G \qquad (3.32).$$

Secondly, the emitting current will be in the form of

$$I = 1.62 \times 10^{14} a \frac{\pi/N}{\sin \pi N} (\alpha[BV_o - S] + G)^2 \exp\left[\frac{-\{\varphi - b[\beta_1 V_o/(a_1 D)^{1/2}\}}{\alpha[BV_o - S] + G}\right]$$

(3.33),

Thirdly, instead of an F.N. plot, the following equation will give

Fig. 3.11 The I-V characteristic of a typical sub-site. (from Bayliss & Latham [9]).

Fig. 3.12 The field-dependence characteristic of the spectral half-width of a typical sub-site. (from Bayliss & Latham [9]).

Fig. 3.13 The linear characteristic of a typical sub-site. (from Bayliss & Latham [9]).

---

rise to a straight line,

$$\mathrm{In}\left[\frac{I}{(\alpha[BV_o-S]+G)^2}\right]-\frac{b[\beta_1 V_o/(a_1 D)]^{1/2}}{\alpha[BV_o-S]+G}=\frac{-\varphi}{\alpha[BV_o-S]+G}+\mathrm{In}(5.89\times 10^{14}a) \qquad (3.34).$$

where

$$B = d\beta_2/(D\epsilon) \text{ and } G = \alpha(\chi-\varphi_1-V^*)+K_bT_o/e,$$

In these equations, a is the emission area and N may again be taken as 1.6.

The examples of the application of equations 3.32 and 3.34, and a plot of lnI versus $(S+\varphi_1-\chi)^{1/2}$ have been given in figures 3.11, 3.12 and 3.13, which show a good fit to the experimental data. However, in figure 3.12, the "kink" at V_o = 6.1 kV remains a common features.

3.3. Theoretical considerations associated with the field-induced hot electron emission model

From the last section, it is apparent that the existing FIHEE model needs clarifying so that a clear physical picture can be given as to how electrons are "heated" in insulator-vacuum interface regions, while they are at the same time loosing most of their energy to the lattice. Furthermore, a new theoretical approach must be developed to account for the experimental data of emission images accumulated in present research programme. In this section, therefore, a simple model will first be given which shows the relationship between the hot electron parameters, such as electron mean energy and drift velocity, and the electric field. Secondly, a consideration will be given to the lattice scattering mechanism, in order to show how the interaction of phonons with electrons influences these relationships. Finally, a coherent scattering theory will be presented which has been developed from the experimental observations on the emission images of electrons emitted from purpose-fabricated MIM structures.

3.3.1. The field dependence of hot-electron parameters

The term "hot electron" is associated with the increase of the mean energy of an electron above that given by 3/2 K_bT_o [69]. Associated with the concept of a hot electron, there is related experimental evidence that shows how such parameters as drift velocity, mean electron energy and diffusion coeffecient vary with field; the former two parameters being particularly interesting to the following discussion. In order to give a simple and complete picture of this dependence, Reggiani [69] has chosen the simple covalent semiconductor model. Although it can not be completely applied to our situation, it provides a clear physical picture that is useful for the later discussion.

This model consists of a single spherical or parabolic band with an effective mass $m = 0.35\ m_o$, and accounts respectively for the acoustic and nonpolar optical scattering coupling constant $E_1 = 4.6$ eV, and the optical deformation potential $E_{do} = 40.3$ eV. Figure 3.14 reproduces the results of a Monte Carlo calculation that Reggiani has presented, and includes definitions of the individual parameters. The results have been reported as a function of electric field for the two temperatures of 8 K and 300 K, where we shall first consider the low-temperature (8 K) case. In the linear response region (i.e. $F <$ 20 V/m in figure 3.14.1a), the acoustic scattering process is sufficient to thermalise electrons down to the lattice temperature T_o. In the intermediate region, which starts at about 100 V/m, and extends up to $\sim 10^3$ V/m, the acoustic scattering mechanism is the only active process as indicated by figure 3.14.1b. Owing to the quasi-elastic nature of this mechanism and since the scattering efficiency of acoustic modes increases with electron energy, the drift velocity is found to behave in a sublinear way, whilst the electron temperature increases slightly above its thermal equilibrium value. In the field region between 10^2 and 10^5 V/m, the optical scattering mechanism builds up until it predominates over acoustic scattering (see figure 3.14.1b). Owing to strong optical scattering, the electron returns to the bottom of the band after each emission process so that under this condition, the drift velocity tends to saturate. Accordingly, the mean electron energy attains an approximately constant value. In the region of field above 10^5 V/m, the optical scattering mechanism maintains its predominant role, but is no longer able to fully dissipate the energy gained by the electrons from the

Fig. 3.14 The field dependence of hot electron parameters. (from Reggiani [69]).

---

field. As a consequence, the drift velocity achieves a new saturation level higher than the previous one; correspondingly the mean electron energy is found to increase more and more steeply with the field till it exhibits a limiting quadratic dependence. In the high-temperature case (T_o = 300 K), figure 3.14.2 shows that, owing to the increased efficiency of the scattering mechanisms in dissipating the energy gained by the field to the lattice, the field region for which the linear response region holds is extended ($E < 10^5$ V/m in the figure). This behaviour results from the increased importance of acoustic-phonon scattering and optical absorption processes. According to the similar reasons, the saturation of the drift velocity and the increase of the mean electron energy are again found to occur at the highest field region ($E > 10^5$ V/m).

The quantum theory of solids will now be used in the following discussion to explore how electrons interact with the lattice.

3.3.2. Electron-phonon scattering mechanisms

This problem has been considered by a number of authors, such as Kittel [70], Conwell [71] and more recently Ridley [72]. Dedicated publications by Frohlich [73], Ridley [74] and Fischetti [75] are also available. Here, only a summary of the important results will be presented.

(i) The nonpolar electron-phonon interaction

Electrons can interact with both acoustic and optical phonons via nonpolar processes, in which the electron Bloch waves are perturbed by the displacement of the ions from their equilibrium position. This displacement results in a deformation potential causing a spatial variation of the energy band structure of the solids. The perturbed energy surface may be calculated in principle; for the acoustic phonon, it may be given by the following form [70]:

$$E(k) = E_o(k) + E_1\Delta \qquad (3.35)$$

where $E_o(k) = k^2/2m^*$ is the electron energy for the unperturbed, nondegenerate, spherical energy band, Δ is the dilation and $E_1 = dE(o)/d\Delta$ is a constant which may be determined in part by pressure measurements [70]. Using the dilation operator given by [70]:

$$\Delta(x) = i\sum_{k}(2\rho\omega_q)^{-1/2}q(a_q e^{i\mathbf{q}\cdot\mathbf{x}} - a_q e^{-i\mathbf{q}\cdot\mathbf{x}}) \tag{3.36}$$

where ρ is the density of the lattice, a_q is the acoustic- or optical-phonon operator, and ω_q is the phonon frequency, and the electron Bloch function

$$\psi(x) = \sum_{k} c_k e^{i\mathbf{k}\cdot\mathbf{x}} u_k(x) \tag{3.37}$$

where c_k is a constant, and $u_k(x)$ is the periodic part of the Bloch function, we ultimately obtain the deformation potential perturbation valid for the normal interaction process, i.e., when $\mathbf{k} - \mathbf{k}' + q = 0$, in the form of

$$H' = iE_1 \sum_{kq} (2\rho\omega_q)^{-1/2} \; |q| \; (a_q - a^{+}_{-q}) \; c^{+}_{k+q} c_k \tag{3.38}.$$

With this Hamiltonian, the total collision rate W of an electron in the state $|\mathbf{k}\rangle$ against a phonon system at absolute zero, is given by Kittel [70] as

$$W = \frac{E^2}{4\pi\rho u_1} \int_{-1}^{1} d(\cos\theta_q) \int_{0}^{qm} dq q^3 \delta(E_k - E_{k-q} - \omega_q) \tag{3.39}.$$

Now the argument of the delta function is

$$\frac{1}{2m^*}(2\mathbf{k}\cdot\mathbf{q} - q^2) - u_1 q = \frac{1}{2m^*}(2\mathbf{k}\cdot\mathbf{q} - q^2 - qq_c) \tag{3.40},$$

where $q_c = 2m^* u_1$. The minimum value of k for which the argument can be zero is

$$k_{min} = \frac{1}{2}(q + q_c) \tag{3.41},$$

which for q=0 reduces to

$$\begin{aligned} k_{min} &= \frac{1}{2} q_c \\ &= m^* u_1 \end{aligned} \tag{3.42}.$$

For this value of k, the electron group velocity $v_g = k_{min}/m^*$ is equal to u_1, the velocity of sound. Thus, the threshold for the emission of phonons by electrons in a crystal is that the electeon group velocity should exceed the acoustic velocity. The electron energy at this threshold is estimated to be equivalent to 1 K. For $k \gg q_c$, the qq_c term in (3.40) may be neglected. Then the integrals in (3.39) become

$$\int_{-1}^{1} du \int dqq^3(2m^*/q)\delta(2ku-q) = 8m^*\int_{o}^{1} duk^2u^2$$
$$= 8m^*k^2/3 \qquad (3.43),$$

and the emission rate is

$$W(\text{emission}) = \frac{2c^2m^*k^2}{3\pi\rho u_1} \qquad (3.44).$$

It is important to note that this is proportional to the electron energy E_k.

For nonpolar scattering with optical phonons, Harrison [76] has shown that the scattering increases with energy at a slower rate.

(ii) The polar electron-phonon interaction

In polar materials, the vibrations of oppositely charged ions give rise to long-range macroscopic electric fields in addition to deformation potentials, and the interaction of an electron with these fields produces additional components of scattering. In fact, the longitudinal optical mode scattering has been considered as the major scattering mechanism in polar materials [73,75,77].

The Hamiltonian describing this coulombic interaction has been given by Fronhlich et al in the form [73,70,78]:

$$H_p = \sum_{k,q} \frac{ieG}{q} c_{k+q}c_k(b_q-b_{-q}) \qquad (3.45),$$

where k and q are the electron and phonon wave vectors, c_k and b_q are the electron and phonon operators, and the coupling constant G is given by

$$G^2 = \frac{\omega_{lo}}{4}\left[\frac{1}{\epsilon_>} - \frac{1}{\epsilon_<}\right] \qquad (3.46),$$

with $\epsilon_>$ and $\epsilon_<$ being respectively the permittivity at frequences larger and smaller than the optical-phonon frequence ω_{lo}. Since the LO-phonon spectrum mostly gives rise to narrow bands, the dispersion of ω_{lo} is usually ignored.

The first order scattering rate at a finite temperature for the emission or absorption of one phonon can be obtained with the Hamiltonian by the Fermi rule, and by using the effective-mass approximation with parabolic and spherical bands: not surprisingly, the ultimate expression is complicated and will not therefore be presented here. However, as discussed by Fischetti et.al.[75], the physical implications, so far as our interest is concerned, is that the scattering probability decreases as the electron-energy increases, since collisions with short-wavelength phonons are less probable.

From the above discussion, it is apparent that no matter what type of material the electrons are travelling in, be it either polar or non-polar, an electron will eventually interact with a phonon in a scattering process, and so can either absorb or emit phonons depending upon their energy; i.e. energy may be either lost to or gained from the lattice. Furthermore, in non-polar materials, the scattering rate of electron interactions with acoustic phonons increases with electron energy, whilst the optical phonon scattering rate increases at a slower rate. On the other hand, in polar materials, electrons can take part in additional polar optical mode scattering process, although the probability decreases as the electron energy increases. Therefore, in both cases, as the electron energy increases, the interaction of electrons with acoustic phonons might be expected to become a dominant mechanism in the scattering process. Finally, it is possible that under high field conditions, the combined scattering processes are not sufficient to thermalize the electrons to their equilibrium situation, so that their average energy will be higher than the lattice. As discussed in the following section, this will involve a consideration of the rate of change of electron energy under the stead-state condition as caused by the combined effects of the scattering processes and the exteral source (e.g. applied field).

3.3.3. The rate of energy loss by scattering processes

In the interaction of electrons with lattice vibrations, an electron in a state with a wave vector **k** can make a transition to the state **k′** by absorbing or emitting one or more phonons. For lattice temperatures not higher than 300 K, the scattering processes involving more than one phonon may be neglected [71]. Thus, after a transition involving a phonon of wave vector **q**, the electron is in a state $\mathbf{k}' = \mathbf{k} \pm \mathbf{q}$, whereas the number of phonons in the lattice oscillator characterized by **q** is $N_{\mathbf{q}} \mp 1$; in both cases, the upper sign corresponds to phonon absorption and the lower to phonon emission.

Thus, once a transition is completed, an electron can gain energy by absorbing a phonon or lose energy by emitting a phonon. In the following calculation, we shall see that as far as hot electrons are concerned, an electron will lose energy in a transition. The rates of these energy changes have been considered by both Conwell [71] and Ridley [74], but in the following, we shall follow Conwell and give a general description of the problem.

(i) The rate of energy loss to the acoustic mode

The average rate at which an electron losses energy to the acoustic lattice modes may be calculated in different ways: one is to first calculate $dN_{\mathbf{q}}/dt$, the rate of increase of the number of phonons with wave vector $\mathbf{q}$, due to emission and absorption by all the electrons. From this, the average energy loss rate is obtained by multiplying the initial states, and then summing over all the $\mathbf{k}$'s. Similar reasoning may be employed to obtain the probability of absorption of a phonon of wave vector $\mathbf{q}$. Combining the two processes, we obtain for the rate of change of $N_{\mathbf{q}}$

$$\begin{aligned}\frac{dN_{\mathbf{q}}}{dt} = \frac{2\pi}{\hbar} \, [\, & |\langle \mathbf{k}, N_{\mathbf{q}}+1 |\, H' \,| \mathbf{k+q}, N_{\mathbf{q}} \rangle|^{2} \\ & \times \delta(E_{\mathbf{k},N_{\mathbf{q}}+1} - E_{\mathbf{k+q},N_{\mathbf{q}}}) f(\mathbf{k+q}) \\ & - |\langle \mathbf{k+q}, N_{\mathbf{q}}-1 |\, H' \,| \mathbf{k}, N_{\mathbf{q}} \rangle|^{2} \\ & \times \delta(E_{\mathbf{k+q},N_{\mathbf{q}}-1} - E_{\mathbf{k},N_{\mathbf{q}}}) f(\mathbf{k}) \,] \end{aligned} \qquad (3.47).$$

As discussed by Conwell [71], it is usually a good approximation to take the distribution function $f(\mathbf{k})$ as the sum of a spherically symmetric term $f_o(E)$ and an additional small term f_1 that gives an asymmetry in the field direction. In calculating the rate of energy loss by scattering, we shall neglect the contribution of this small asymmetry component and replace $f(\mathbf{k})$ and $f(\mathbf{k} + \mathbf{q})$ by their spherically symmetric parts. Also, we shall only consider spherical constant energy surfaces. This mathematic procedure will lead to an expression for $dN_{\mathbf{q}}/dt$ in terms of the energy of a phonon with a vector $\mathbf{q}$ by intergrating over all $\mathbf{q}$'s, and dividing by the number of electrons.

In the last section, we obtained the scattering rate that gives the probability that a phonon with a wave vector $\mathbf{q}$ is emitted per unit time by an electron making a transition from $\mathbf{k} + \mathbf{q}$ to $\mathbf{k}$. This of course presumes that the electron is actually in a $\mathbf{k} + \mathbf{q}$ state at the begininig of the transition interval. To find the total number of phonons with $\mathbf{q}$ emitted in a time t, we must multiply the above expression by the probability $f(\mathbf{k} + \mathbf{q})$ of the electron being in the initial state, which gives rise to

$$\frac{dN_q}{dt} = \frac{u_l}{2l_{ae}}\,\frac{n}{N_c(T_e)}\,\frac{T_e}{T}\left\{(N_q+1)\exp\left(\frac{-\hbar u_l q}{K_b T_e}\right)-N_q\right\}\exp\left[\frac{-\hbar^2 q^2}{8mK_b T_e}\right] \qquad (3.48)$$

where u_l is the longitudinal velocity of sound, l_{ae} the mean free path for acoustic scattering under equipartition, n the electron concentration, N_c the effective density of states and T_e the temperature of the hot electron gas.

Equation 3.48 may be further simplified. Since, for the phonons with which the hot electrons interact, $\hbar u_l q \ll K_b T_e$, so that we may replace $\exp(-\hbar u_l q/K_b T_e)$ by $(1- \hbar u_l q/K_b Te)$: thus, the expression in the bracket becomes $\{1-(N_q+1)\hbar u_l q/K_b T_e\}$.

The average rate of electron energy loss to the accoustic mode is,

$$\left[\frac{dE}{dt}\right]_a = -\frac{1}{nV_l}\sum_q \hbar u_l q\left[\frac{dN_q}{dt}\right]_e$$

$$= \frac{-\hbar u_l}{2\pi^2 n}\int_{q=0}^{q_o} dq\,q^3\left[\frac{dN_q}{dt}\right]_e \qquad (3.49)$$

For intergration over q, the upper limit may be taken as ∞ , since $(dN_q/dt)_e$ given by [3.48] falls off rapidly for large q. The integration over q may then be carried out very simply for N_q obeying equipartition, i.e.

$$N_q + \frac{1}{2} = \frac{K_b T}{h\omega_q} \qquad (3.50),$$

where when $h\omega_q \ll K_b T$, corresponds to the situation appropriate for hot electrons. The result for this case is

$$\left[\frac{dE}{dt}\right]_{ae} = -\frac{8}{\pi^{1/2}} \frac{(2K_b T/m)^{1/2}}{l_{ae}} m u_1^2 \left[\frac{T_e}{T}\right]^{3/2} \left[1 - \frac{T}{T_e}\right]$$

$$= -R\left[\frac{T_e}{T}\right]^{3/2} \left[1 - \frac{T}{T_e}\right] \qquad (3.51).$$

For hot electron, $T_e > T$ holds, so that $(1-T/T_e) > 0$. In this case, the minus sign on the right hand side of the above equation indicates that the electron losses its energy during the interaction.

(ii) The optical modes

For optical mode scattering, it is a good approximation to neglect the dispersion of ω_o. Therefore, the rate of change of electron energy due to these scattering processes is given by ω_o times the difference between $1/\tau$ for phonon absorption and $1/\tau$ for phonon emission. Conwell [71] has given the average rate of energy loss for non-polar scattering in the form of

$$\left[\frac{dE}{dt}\right]_{op} = -\frac{1}{\pi^{1/2}} \frac{(2K_b T/m)^{1/2}}{l_{ae}} \frac{E_{1op}}{E_1^2} \frac{(\hbar\omega_o)^2}{K_b T} \left[\frac{T_e}{T}\right]^{1/2} M(x_o, x_e) \qquad (3.52)$$

where

$$M(x_o, x_e) = \frac{e^{(x_o - x_e)} - 1}{e^{x} - 1} \frac{x_e}{2} e^{x_e/2} K_1 \frac{x_e}{2} \qquad (3.53)$$

$$x_e = \hbar\omega_o / K_b T_e \qquad (3.54),$$

and K_1 is a Bessel function of the second kind with imaginary argument, E_{1op} an optical deformation potential constant, E_1 a acoustic deformation potential constant. For polar optical scattering,

$$\left[\frac{dE}{dt}\right]_{po} = \frac{2eE_o \hbar\omega_1}{(2mE)^{1/2}} \left[N_q \sinh^{-1}\left[\frac{E}{\hbar\omega_1}\right]^{1/2} - (N_q + 1)\sinh^{-1}\left[\frac{E - \hbar\omega_1}{\hbar\omega_1}\right]^{1/2}\right] \qquad (3.55)$$

where E_o is a measure of the strength of coupling to the polar modes.

On the basis of this, Conwell [71] has also pointed out that, if only on the evidence that breakdown does not occur, other mechanisms take over when polar optical scattering becomes less effective.

In fact, for the case of lattice temperatures T < 300 K, there are only a few optical phonons within the lattice, so that the absorption of phonons can be neglected. Therefore, we have

$$\frac{dE}{dt} = -\frac{\hbar\omega}{\tau} \qquad (3.56),$$

This conclusion will be found to be useful when we discuss the saturation of the emission current.

(iii) The hot electron temperature T_e and the variation of electron mobility with field

In order to investigate how T_e and μ vary with F, it is convenient to express μ in terms of T_e. For the simple model, we may use a relation, that is valid for a Maxwell-Boltzman distribution [79],

$$\mu = \frac{e}{m}\frac{\langle E\tau\rangle}{m\langle E\rangle}$$

$$= \frac{4\pi}{3\pi^{1/2}m}\int_o^\infty x^{3/2}\tau\, e^{-x}dx \qquad (3.57)$$

where $x = E/K_bT_e$.

Shockley [79] was the first to calculate the dependence of J on F for hot electrons in a semiconductor. There are no restrictions on applying his findings to other cases provided that the acoustic mode is the dominant scattering process in the field range of interest. Thus, using the relaxation time [71], i.e.,

$$\tau_{ae} = \left[\frac{m}{2E}\right]^{1/2} l_{ae}$$

$$= \left[\frac{m}{2K_bT_e}\right]^{1/2}\left[\frac{l_{ae}}{x^{1/2}}\right] \qquad (3.58).$$

Substitution of (3.58) into (3.57) leads to

$$\mu(T_e) = \frac{4el_{ae}}{3(2\pi mK_bT_e)^{1/2}} \qquad (3.59).$$

Similar reasoning leads to the following expression for the low-field mobility:

$$\mu_o(T) = \frac{2el}{3m^*}\sqrt{\frac{2m^*}{\pi K_bT}} \qquad (3.60),$$

so that by comparing (3.59) and (3.60), we obtain

$$\mu = \mu_o\sqrt{\frac{T}{T_e}} \qquad (3.61).$$

Now under steady-state conditions

$$\frac{dE}{dt} = \left[\frac{dE}{dt}\right]_{ae} + \left[\frac{dE}{dt}\right]_f$$

$$= 0 \qquad (3.62),$$

where $(dE/dt)_{ae}$ is given in equation 3.51, whilst $(dE/dt)_f$ is the rate of change of the electron energy due to the acceleration by the external field F, i.e.

$$\left[\frac{dE}{dt}\right]_f = e\mathbf{F}\cdot\mathbf{v}_d$$

$$= e\mathbf{F}\cdot\mu\mathbf{F}$$

$$= e\mu F^2 \qquad (3.63)$$

where we still define $\mathbf{v}_d$ as

$$v_d = \mu F \qquad (3.64).$$

Thus,

$$\frac{8m^* u_1}{l_{ae} T}\sqrt{\frac{2K_b T_e}{\pi m^*}}(T-T_e) + e\mu F^2 = 0 \qquad (3.65)$$

or

$$\frac{8m^* u_1}{l_{ae} T}\sqrt{\frac{2K_b T_e}{\pi m^*}}(T-T_e) + e\mu_o \sqrt{\frac{T}{T_e}}\, F^2 = 0 \qquad (3.66)$$

Finally, we obtain

$$T_e = \frac{1}{2}\left\{1+\left[1+\frac{3\pi}{8}\left(\frac{\mu_o F}{u_1}\right)^2\right]^{1/2}\right\} T \qquad (3.67)$$

and

$$\mu = \mu_o\sqrt{2}\left\{1+\left[1+\frac{3\pi}{8}\left(\frac{\mu_o F}{u_1}\right)^2\right]^{1/2}\right\}^{-1/2} \qquad (3.68).$$

For fields of $F \gg u_1/\mu_o$

$$T_e = \sqrt{\frac{3\pi}{32}}\left[\frac{\mu_o F}{u_1}\right] T$$

$$= \sqrt{\frac{3\pi T^2 \mu_o^2}{32\ u_1}}\ F$$

$$= XF \qquad (3.69)$$

where

$$X = \sqrt{\frac{3\pi T^2 \mu_o^2}{32\ u_1}} \qquad (3.70)$$

i.e. T_e is proportional to the electric field F.

Assuming that for the optical scattering,

$$\left[\frac{dE}{dt}\right]_P = \frac{\hbar\omega}{\tau} \qquad (3.71),$$

we have

$$-\frac{\hbar\omega}{\tau} + eFv_d = 0 \qquad (3.72)$$

so that

$$v_d = \frac{\hbar\omega}{eF\tau} \qquad (3.73).$$

On the other hand,

$$m^*v_d = eF\tau_o \qquad (3.74)$$

so that

$$v_d = \sqrt{\frac{\hbar\omega}{m^*}} \qquad (3.75),$$

which shows that v_d has become independent of F, and that the current density will become saturated, as can be seen below:

$$J = nev_d = ne\sqrt{\frac{\hbar\omega}{m^*}} \qquad (3.76)$$

3.3.4. Coherent scattering of hot electrons in the top metal layer of MIM structures

Field-induced electron emission into vacuum from purpose-fabricated metal-insulator-metal structures has been observed by a number of authors, such as Mead [80,81], Cohen [82,83], Kanter [84], Collins et al [85], Nelson [86], Simmons et al [8,88], Gould et al [89,90] , Yu [91] and more recently DiMaria et al [92]. In many cases, the emission has been found to be associated with pinholes in the top metal layer [87,88,89,91]. By photograhphing the emission on an imaging phosphor screen, non-uniform emission images have been obtained and reported by a number of authors, including Simmons et al [87,88], Gould [89,90]. In particular, Simmons et al [8] observed that the electrons ejected from the top metal electrode were imaged as bright arcs of the same radii superimposed on a faint background; furthermore, all of the arcs appeared to subtend an angle of < 180°, as shown in figure 3.15. To explain these results, Simmoms et al [8] proposed an electron diffraction model in which hot electrons, generated in the insulating medium, impinge normally on the upper metal electrode and undergo a coherent scattering process before being

Fig. 3.15 The emission images obtained from purpose-fabricated MIM devices. (from Simmons et al [8]).

Fig. 3.16 A sequence of emission images as obtained from the MIM structure whose top metal electrode contained a small square hole, illustrating the field-dependence of the image. (from Simmons et al [88]).

injected into the vacuum. Further evidence supporting this hypothesis was subsequently obtained by Simmons & Verderber [88] by observing that the emission pattern associated with a small square hole intentionally made in a thick Au top electrode was symmetrical, and that the image appeared as a solid segment, whose outer edge had the form of a well-defined arc (see figure 3.16). Subsequently, other experiments, such as those carried out by Gould & Collings [89] and Gould & Hogarth [90], showed that it is possible for hot-electrons to undergo a coherent scattering process and be emitted through a "perfect" metal layer to give a "ring-like" image structure, rather than an "arc-like" structure, i.e. as shown in figure 3.17. Their results were considered to be consistent with the Simmons´s theory. In the course of the present research programme, we have observed similar emission patterns from both a significant number of naturally occuring sites and also artificially simulated sites, and as will be discussed in chapters 5 and 6, they have been found to be broadly consistent with the diffraction theory. To provide a framework for this discussion, the coherent scattering model will now be described.

(i) Coherent scattering processes in the top metal layer

This model was first proposed by Simmons et al [8] to explain the arc-like nature of the emission images obtained from artificial MIM structures Thus, for his experimental system, electrons are assumed to be injected from the Al substrate electrode into the conduction band of the insulator by a tunnel-hopping process via discrete levels provided by the injected ions. They are then accelerated towards the top Au electrode, a fraction of them arriving there with little loss of energy, i.e., with an energy equal to $V_b+\eta$, where V_b is the bias voltage across the sandwich and η is the Fermi energy of the top metal

Fig. 3.17 Photographs of emission patterns of coherently scattered electrons emitted through the surface of the top metal layer of MIM structures. (from Gould et al [90]).

---

electrode. Furthermore, since the transverse energy of the electron is of the order $K_b T$, it follows that the electrons are incident essentially normally on the top metal electrode.

On the basis of the foregoing discussion, and because the Au electrode is essentially polycrystalline, we have all the ingredients for coherent scattering to occur. Hence, electrons will be diffracted by an angle 2θ where θ is given by the Bragg law $\sin\theta = \lambda/2d_{(hkl)}$, where $\lambda = 12.27/(V_b + \eta)^{1/2}$ is the electron wavelength. For Au, the separation of the (111) planes, is $d_{111} = 2.35$ Å; thus, for $V_b = 10V$, $\theta = 40.5^{\circ}$ and $2\theta = 81^{\circ}$, which means that the electrons are diffracted almost into the plane of the electrode, and thus will not normally be able to escape from the electrode. However, if the diffraction occurs very near to the edge of a pinhole [see figure 3.18.], electrons in that portion of the cone of diffraction close to the edge of the pinhole will have sufficient energy to surmount the surface potential barrier or the work function of the Au electrode.

(ii) The energy condition for the emission of diffracted electrons from the edge of the top metal electrode

According to the coherent scattering process described above, the velocity v of an electron in that cone can be resolved into two components $v_{\parallel}$ and $v_{\perp}$, i.e. respectively parallel to and normal to the plane of the film. Vectors drawn from O to the circumference of the semicircle shown in the velocity diagram of figure 3.19, represent all possible values of the velocity vectors in the plane of the film, $v_{\parallel}$, that the diffracted electrons can have that arrive at the edge of the pinhole. However, it is only those electrons arriving at the surface satisfying the condition [8]

$$v_{\parallel} \cos\Theta > [(\varphi+\eta)2/m]^{1/2} \qquad (3.77)$$

that can emerge from the surface, where φ is the work function of the electrode; that is, only those electrons whose velocity vectors lie within an angle Θ_o of the normal to the surface can escape from the

Fig. 3.18 The physical diagram of the edge structure of a pinhole in the top metal electrode of MIM structure, with the cone of diffraction of the electrons superimposed. (from Simmons et al [8]).

Fig. 3.19 The velocity diagram of the parallel components of the electron velocities. (from Simmons et al [8]).

---

surface; the rest will be internally reflected.

(iii) The energy condition for the emission of electrons through the top metal electrode

It is apparent that the angle θ decreases as the energy of electrons increases; i.e. electrons trajectories gradually move towards the forward direction. Therefore, if electrons can become "hot" enough in the insulating medium, and the top metal layer is thin enough (less than the mean free path of the hot electron in the metal), electrons will be able to escape into vacuum through the top metal electrode. Similar to the reasoning of the last section, we have [89]

$$(\eta+V_b)-(\varphi+\eta)^{1/2}(\eta+V_b)^{1/2}-\frac{h^2}{4em}\frac{n^2}{d^2}>0 \tag{3.78}$$

or

$$(\eta+V_b)-(\varphi+\eta)^{1/2}(\eta+V_b)^{1/2}-\frac{75}{d^2}>0 \quad (n=1) \tag{3.79}$$

(iv) The field-dependence of the geometrical parameters and the shape of the emission image

The characteristic features of the emission images resulting from this coherent scattering process can be summarized as following: (i) an image typically consists of a number of arc-like segments; (ii) both the outer edge of an individual segment, and their overall size increase with the cathode bias voltage; (iii) the outer radius of a segment increases with the cathode bias voltage but decreases with the bias voltage of the phosphor screen. Simmons et al [8,88] also gave an account for these observations in terms of the diffraction theory.

Thus the arc-like segmental images, i.e. those of figure 3.15, are considered to indicate that electrons are emitted from the edge of the top metal layer; in particular, from a triple junction location associated with a pinhole. Although the diffracted electrons will form a cone, those in the half opposite the edge will be "internally" reflected; conversely, it is only those electrons injected towards the edge that have the possibility of being emitted, so that the arc-like segment appears to be subtend an angle of < 180°.

Finally, the radius of a segment can be related to the bias voltages of the phosphor screen and cathode substrate. Thus, the radius of an arc can be derived from following equation

$$r = v_{\perp} t \tag{3.80}$$

and the final result,as given by Simmons et al [8], is presented below,

$$r = \frac{24.54s}{d\sqrt{V_a}} \left[1 - \frac{36}{d^2(\eta + V_b)} \right]^{1/2}$$

here s is the distance between the emitter and screen (in cm), with the other parameters having been defined previously. The V_a appears inversely to r indicating that r will decrease as V_a increases, whilst the increase of V_b will cause the decrease of the second term in the brackets so that the value of the brackets will become bigger, resulting in an increase of the radius.

CHAPTER FOUR

EXPERIMENTAL SYSTEMS

4.1. Introduction: field emission spectrometers

There are, in principle, two main types of spectrometer that could be used to investigate the energy distribution of field-emitted electrons: the retarding potential and the electrostatic deflection analyzers. A popular design for the retarding potential analyzer is that due to Van-Oostrom [44], as illustrated schematically in figure 4.1. In its conventional application, a sharp micropoint emitter with radius of ~100 nm allows high fields of $> 10^{9}$ Vm^{-1} to be created at its tip under moderate accelerating potentials (0.5-5 kV). Those emitted electrons that pass through the anode hole are retarded by the lens L to an energy of a few eV and focussed on to a collector electrode C. A slowly increasing ramp voltage V_c is applied to the collector C so that high energy electrons are collected initially at low values of V_c, with all electrons being eventually colleted if V_c is great enough; a typical plot of collector current I_c against V_c obtained with this type of instrument is shown in figure 4.2. This is known as an integral plot which needs differentiating in order to obtain the energy distribution P(E) of the emitted electron current (see figure 4.2.). In contrast, an electrostatic deflection analyzer, gives an energy distribution directly. Thus, referring to figure 4.3, the heart of a deflection analyzer is an energy dispersive element consisting of two concentric hemispheres with a potential difference ΔV across them. This arrangement allows electrons focussed at input aperture B with a kinetic energy E to pass between the hemispheres in great circles and be refocussed at an exit aperture C as discussed by Purcell [93]. Electrons with energies outside the pass range $(E-\Delta E)$ to $(E + \Delta E)$ of the analyzer collide with the hemispheres and are either trapped there or emerge diffusely at C. If now the voltage V_s is

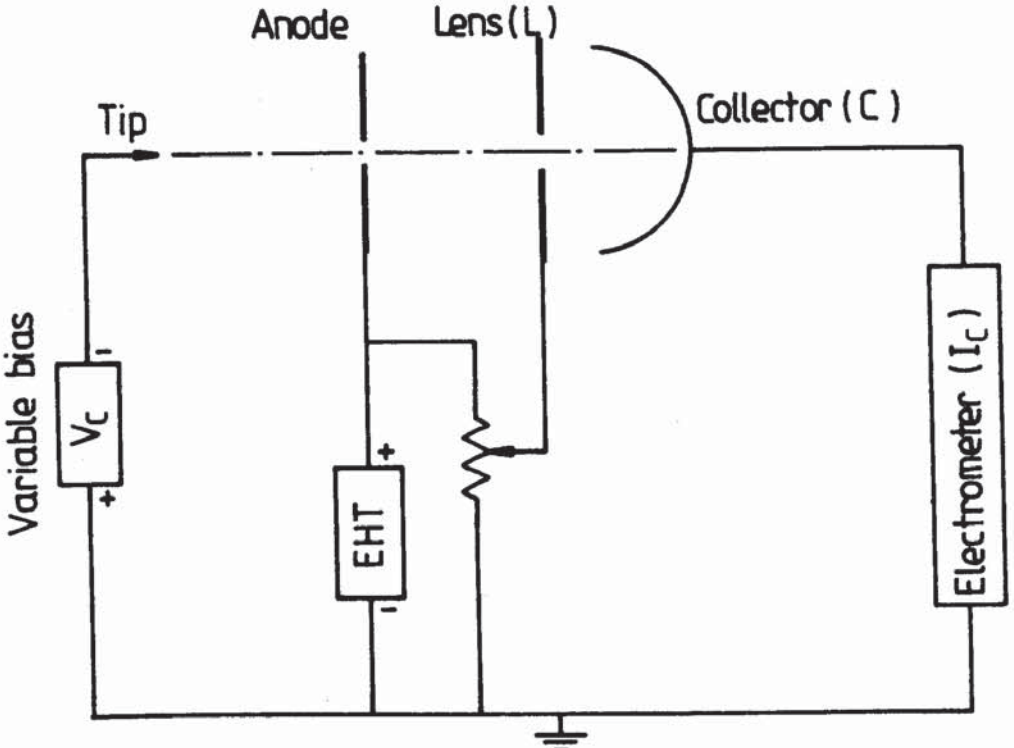

Fig. 4.1 A schematic illustration of the essential features of a retarding potential analyzer.

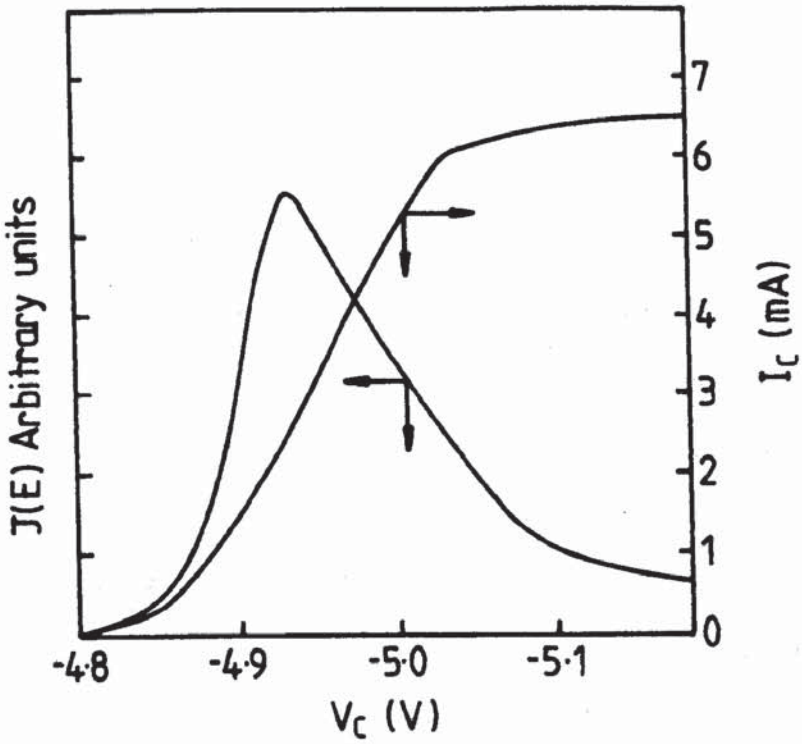

Fig. 4.2 A plot of integral current I_c, and corresponding differential graph J(E), as pbtained from a retarding potential analyzer, both as functions of retarding voltage V_c.

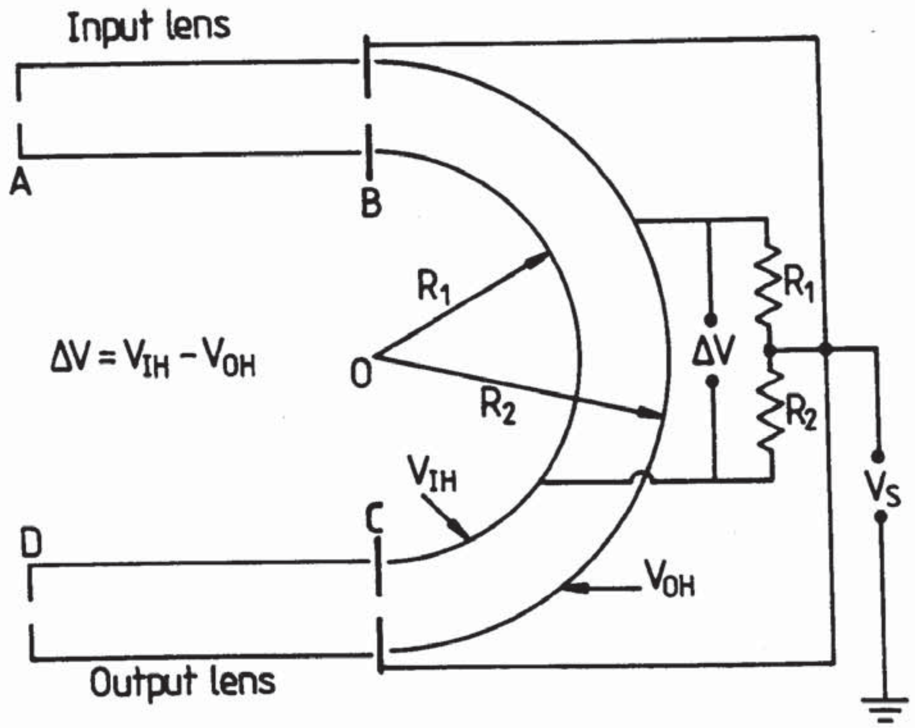

Fig. 4.3 A schematic diagram illustrating the principle of the hemispherical deflection analyzer.

---

varied linearly with time (i.e. ramped), it follows that the analyzing "energy window " will be swept through the whole energy range. Thus a plot of the electron current emerging from C against the ramp voltage will generate the electron energy distribution. To a first approximation, the deviation E of an analyzing energy of the analyzer is linearly dependent on the analyzing energy E (see section 4.2.1.), so that a small kinetic energy at the entrance aperture B is required to obtain higher resolution. An input lens system is therefore necessary, firstly, to retard highly accelerated field-emitted electrons having energies of several keV´s into the analyzing energy range of a few eV and, secondly, to focus an image of aperture A onto B (see figure 4.3). An output lens then re-accelerates the electrons emerging at C and focusses them onto the aperture D, thereby preventing any scattered electrons at C from passing D in great numbers. An electron multiplier collects all electrons accelerating away from D and produces an analyzer output signal.

In fact each of these two types of spectrometer has their own merits. The retarding potential analyzer is quite simple in its design, and hence readily machined and constructed. In applications where high resolution is not required, it is still widely used (see, for example, references 94 and 95). The deflection analyzer on the other hand has two important advantages over the retarding potential analyzer. Firstly, it is readily possible to use electron multiplier techniques for greatly increasing the sensitivity of the collected electron current detection system. Secondly, the output from such analyzers gives an field electron energy distribution (F.E.E.D.) directly, with a nearly constant signal-to-noise ratio over a complete energy spectrum. This approach was first used by Kuyatt and Plummer [96] for the measurement of F.E.E.D´s, who designed an instrument based on a 135° deflection analysing element formed from concentric spheres of 25 mm mean radius. Subsequently, Braun et al [97] constructed a more advanced analyzer of this type to provide the experimental evidence necessary to complement theoretical studies of field emission from semiconducting materials. Later, Latham and co-workers [31,98] have further developed this instrument for the study of field emission from broad-area electrodes, and now it has become a highly-specialized and versatile facility. This later version of the facility formed the basis of the apparatus used in the present research programme and is described in the following section.

4.2. Design and operational features of the spectrometer facility

In this section, we shall give an account of the basic spectrometer facility and other instruments which enhance the versatility of the spectrometer; these include the electron emission imaging system and the automatic spiral-scan system for searching a specimen for emission sites. The new spatially resolved energy selective analysis technique developed specifically for this work will be described in detail in section 4.3.

4.2.1. Design features of the hemispherical analysing element

The practical design equations for the hemispherical analyzer were given by Kuyatt and Plummer [96] and may be summarized as follows.

a) An electron will move in the mid sphere between the two hemispheres if $mv^2 = eF_oR_o$, where e is the electronic charge, m the electronic mass, v the electron velocity and F_o is the electric field at radius R_o. From the electrostatic potentials at the mid point of, and immediately outside the hemispheres and the voltage ΔV across them, the potentials V_1 on the inner hemisphere (radius R_1) and V_2 on the outer hemisphere (radius R_2) may be calculated in terms of the analysing energy E. Thus

$$\Delta V = \frac{E}{e}\left[\frac{R_2}{R_1} - \frac{R_1}{R_2}\right] \qquad (4.1),$$

$$V_1 = \frac{E}{e}\left[\frac{R_2}{R_1} - 1\right] \qquad (4.2),$$

$$V_2 = \frac{E}{e}\left[\frac{R_1}{R_2} - 1\right] \qquad (4.3),$$

b) The resolution is given by:

$$\frac{\Delta E}{E} = \frac{z}{2\,R_o} + \frac{\alpha^2}{2} \qquad (4.4)$$

where Z is the width of the input and output slits, while α is the angular spread of the beam.

To minimise the broadening of the transmission function, the input lens is so designed that

$$\alpha^2 = \frac{Z}{4\ R_o} \qquad (4.5)$$

and therefore

$$\frac{\Delta E}{E} = \frac{5}{8}\,\frac{Z}{R_o} \qquad (4.6).$$

c) The minimum deviation of the beam, Z_m, from the central path is

given by:

$$\frac{Z_m}{R_o} = \frac{\Delta E}{E} + \left[\alpha^2 + \left(\frac{Z}{R_o} + \frac{\Delta E}{E}\right)^2\right]^{1/2} \qquad (4.7).$$

These equations show that for the best resolution, the smallest pass width ΔE for a given energy E is required, and that E, Z and should be as small as possible with R_o as large as possible. However, very low energy electrons are difficult to control because of stray magnetic fields and potential patch effects on the hemisphere surfaces [93], while decreasing the aperture size will reduce the total electron transmission through the analyzer thus requiring more sensitive detecting equipment. On the basis of these considerations, the Aston analyzer was designed to have the following parameters:

$E = 2eV$, $Z = 1mm$, $Z_m = 5mm$,
$R_o = 50mm$, $R_1 = 40mm$, $R_2 = 60mm$,
$\Delta V = 1.67V$, $V_1 = + 1.0V$, $V_2 = -0.67V$,
Resolution: ~25 meV

During the practical construction of the analyzer, a mu-metal shield was fitted onto the whole analyzer to screen it against magnetic fields, and a subsequent investigation indicated that the electron spectrum was not altered by further shielding against the earth magnetic field using Helmholtz coils.

4.2.2. The input and output lenses

The input lens system to the spectrometer consisted of a three-element electrostatic lens designed by Heddle et al [99], followed by a fixed-ratio lens. This system had to fulfil the following criteria:

(1) To decelerate electrons from an energy of several keV to 2 eV at the entrance aperture B.

(2) To focus the beam of electrons into the entrance aperture B with a small angular divergence.

(3) To be capable of operating over an input energy range of 1 to 4 keV, and an analysing energy range of 1 to 18 eV.

At the exit of the spectrometer, the output lens re-accelerates the electrons to 200 eV. To collimate the electron beam, in both input and output lenses, one of their elements contains a set of X-Y deflector plates. A schematic diagram of the electron optical system in the spectrometer is given in figure 4.4.

4.2.3. The electrical and electronic drive systems

The electrical connections to the spectrometer are schematically illustrated in figure 4.5. In particular, the lens voltages are supplied from a single fully-adjustable 2MΩ resistor chain, so that the lens voltage-ratios, and hence their focussing properties, remain constant as the anode voltage V_a is varied through a range 1 to 5 kV. The voltage V across the hemispheres is also adjustable to accommodate analysing energies varying from 2 eV to 18 eV.

The energy scan is achived by using a versatile ramp generator which gives a switched amplitude of 1,2,5 or 10 V, with a continuously adjustable starting voltage. This system enables the hemisphere mid

Fig. 4.4 The electron optic arrangement of the unmodified spectrometer. (from Braun et al [97]).

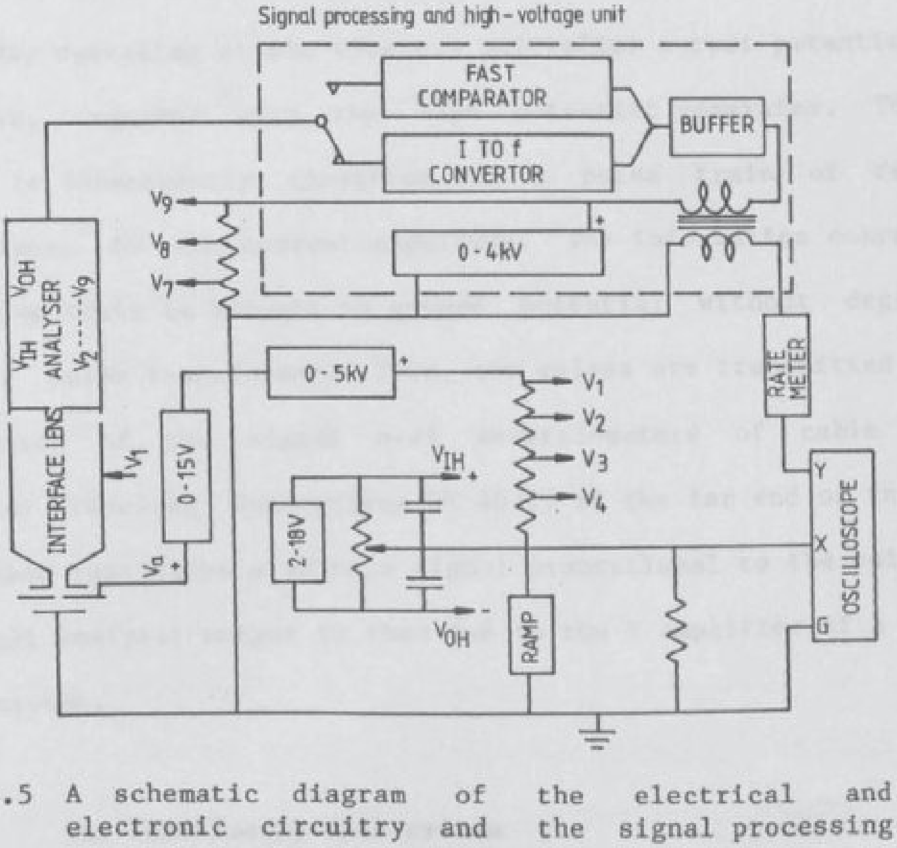

Fig. 4.5 A schematic diagram of the electrical and electronic circuitry and the signal processing arrangement for the analyzer.

potential, V_4, to be ramped over these ranges, starting anywhere between 0 and 15 V, with a scan time variable between 10 ms and 100 s. The arrangement, shown in figure 4.5, allows the transmission energy to be scanned by ramping V_4 whilst keeping V_a and V_1 constant. Thus the resolution of the analyzer, and the emission process, are not affected, also there is a neligible effect on the lens focussing properties.

4.2.4. The detection system

This system consists of a Channeltron electron multiplier, a combined signal-processing/high-voltage unit and a ratemeter. The electron multiplier (Müllard B 318 AL/01) has a gain of $\sim 5 \times 10^{7}$, with an open end suitable for current measurement. Electrons leaving the Channeltron are collected by an electrode biased 200 V positively with respect to the end of the Channeltron. This electron current then is fed to a directly-coupling signal processing unit (Brandenburg model 494) operating at the electron multiplier output potential of 1 to 4 kV, together with the high potential generator. The input current is subsequently converted to a pulse train of frequency proportional to the current magnitude. The information contained in this pulse train is brought to ground potential without degradation using a pulse transformer. Thus, the pulses are transmitted without degradation of the signal over several-meters of cable to the ratemeter (Nuclear Enterprises NE 4672) at the far end of the cable, which then reproduces a voltage signal proportional to the pulse rate. The final analyzer output is then fed to the Y amplifier of a storage oscilloscope.

4.2.5. The interfacing lens system

When used for measurements of electron emission from broad-area electrodes, the spectrometer needs an additional lens systems (the interfacing lens) to fulfil the following requirements:

(1) The first lens element should form the anode of a HV test gap and provide an electrical field of up to 30 MV/m at an earthed cathode to stimulate the electron emission process.

(2) To converge emitted electrons to a focus at the aperture of the analyzer (see above).

Allen and Latham [98] constructed such lens system (figure 4.6a) by using an additional anode A_1, which was separated from a "test" cathode, which formed by a standard gap of 0.5 mm, and is followed by a second electrode L_1 to obtain a lens with convergent properties. Later, Bayliss and Latham [31] found that an emission image could be obtained on a phosphor screen formed on the front face of the input aperture electrode; the image being viewed through a slot on the cylindrical electrode of the interfacing lens. In addition, it was also considered necessary to add a further weak lens by separating the cylindrical electrode into two pieces, i.e. the second electrode L_1 and third electrode L_2 that was electrically connected with the input aperture electrode A_2. The important consequence of Bayliss's modification is that by positioning a sub-spot [31,32], which is responsible for a single-peak spectrum, at the input aperture probe hole, it was possible to make spatially-resolved spectral measurements of the entire image. However, the arrangement was not entirely satisfactory, since it suffered from the following two disadvangtages. a) Often part of an image of a single site was shielded by the wall of the electrodes L_1 or L_2. b) Sub-spots, or segments, of an image could not always be resolved so that the spatially-resolved spectral measurement could only be made with a portion of emission sites. In addition, the weak lens formed in the gap between L_1 and L_2 was found

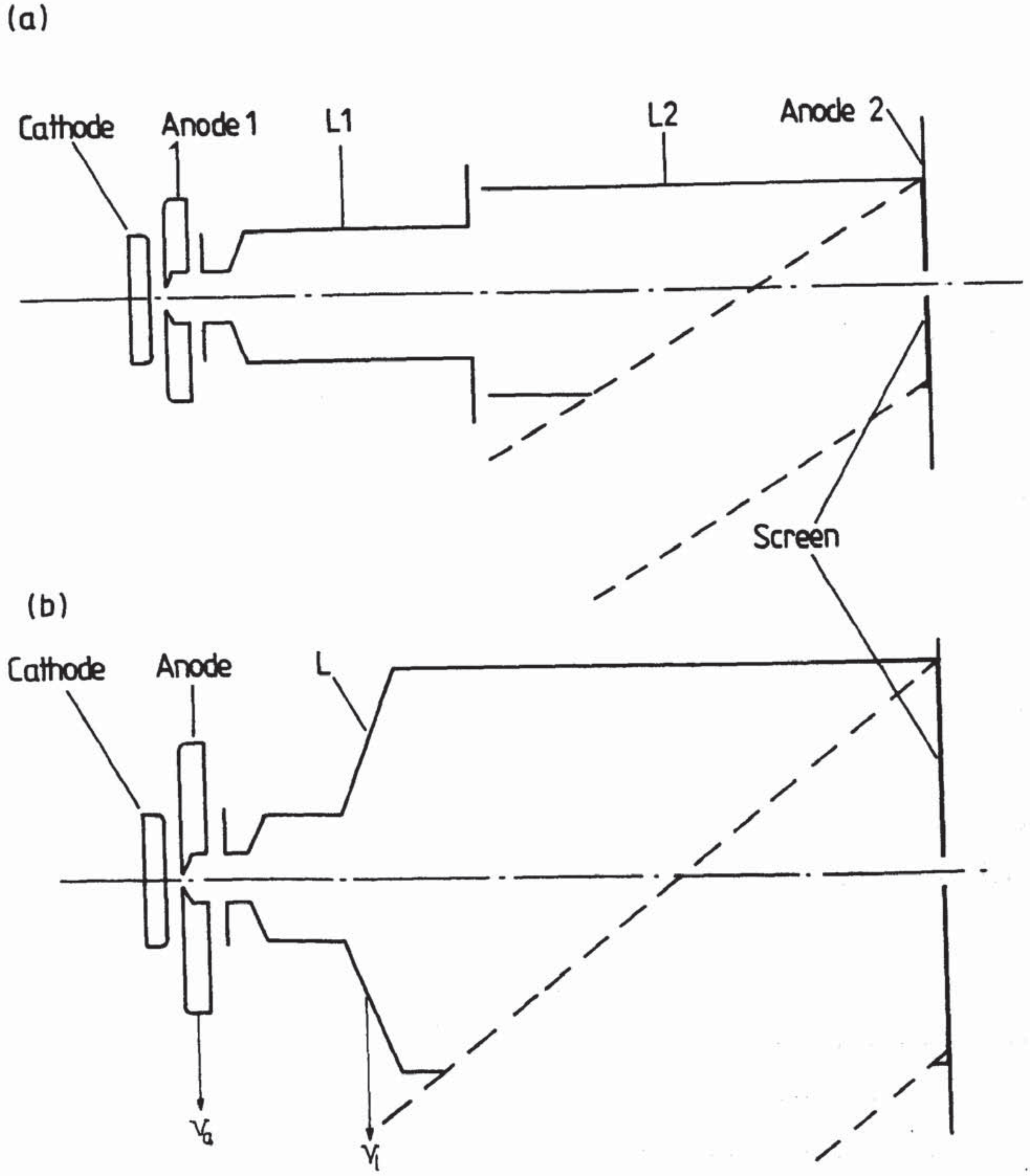

Fig. 4.6 A schematic illustration of the interface lenses.

to be of little use. This was not surprising, since with 15 mm diameter cylindrical electrodes, the small ratio of voltages did not have any real influence on an electron beam.

Therefore, to improve this system, experiments were made on lenses with different geometry, where the final chosen version is shown in figure 4.6b. The essential modifications introduced by this design are:

(1) the "weak" lens was eliminated.

(2) the length of the cylindrical electrode L_1 was shortened from 3.5 cm to 2 cm.

(3) the inner diameter of the cylindrical electrode L_2, and accordingly the diameter of the screen, was increased from 15 mm to 25 mm.

In order to understand the electron optic properties of the new lens system, the potential, and hence field distributions of this chosen configuration was plotted using a standard 2-dimensional conducting paper technique, and is shown in figure 4.7. In practice, the axial section of the lens was magnified by 500 in the plane of paper, and a potential difference of 500 V was taken as the basic increment between equipotentials. As can be seen, the lens is actually composed of two individual component lenses: a divergent lens d followed by a convergent lens c.

The magnification of the lens system, which is dependent on the voltage ratio of V_a to V_1, was estimated by comparing the displacement of an object (i.e. a site on the test cathode) with that of its corresponding image on the phosphor screen. Thus, results obtained by this technique are shown in figure 4.8. Although these were limited by the brightness of the image, and a restricted range of V_a (due to the breakdown voltage of the electrode assembly), it is nevertheless reasonable to extrapolate the measured points as shown by the dashed line in figure 4.8.

However, this does not represent the total magnifications of the image, since we have not yet considered the special features of an emissive object. Thus, referring to figure 4.9, electrons emitted

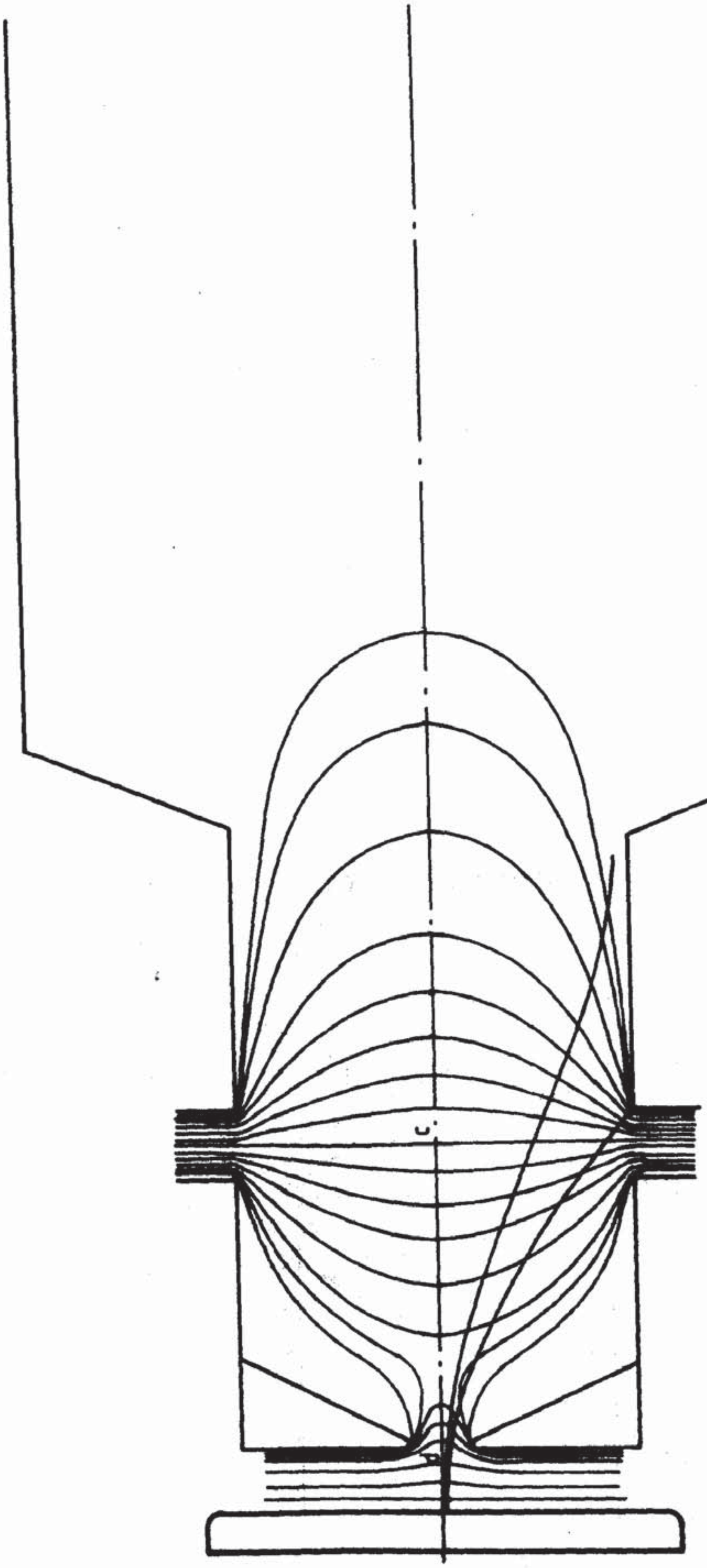

Fig. 4.7 The potential distribution of the interface lens.

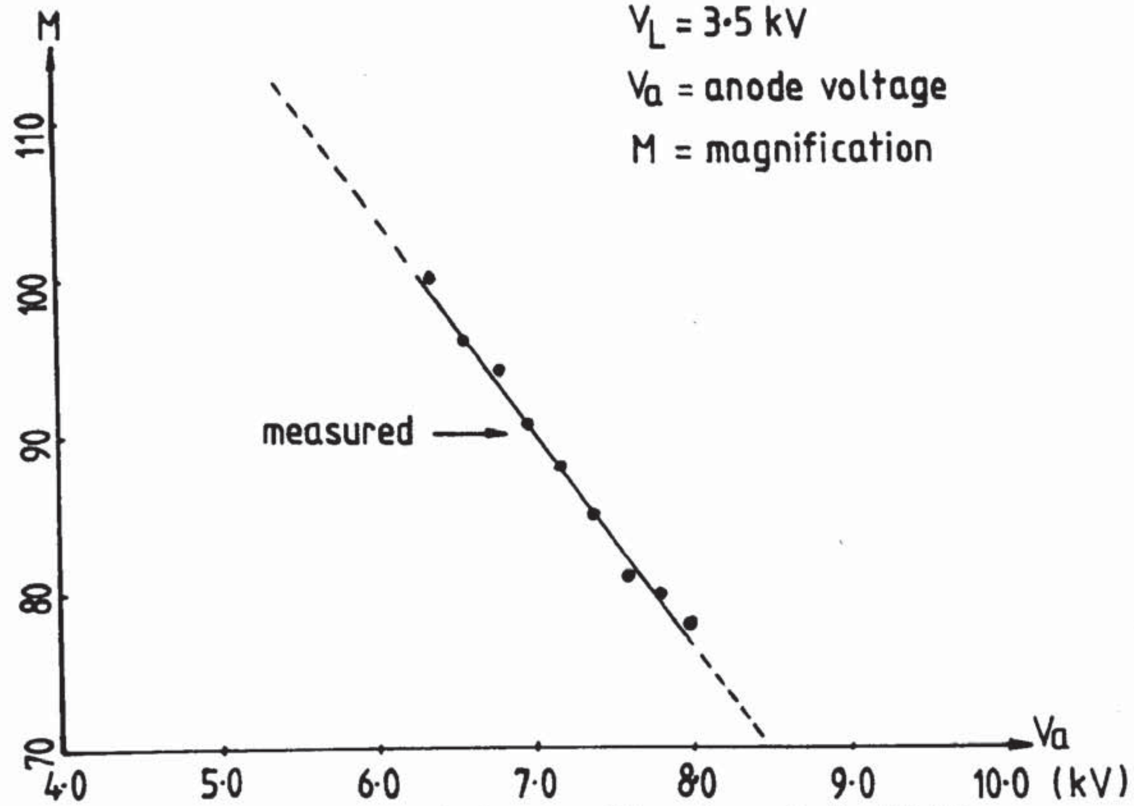

Fig. 4.8 The variation of the magnification of the field imaging system.

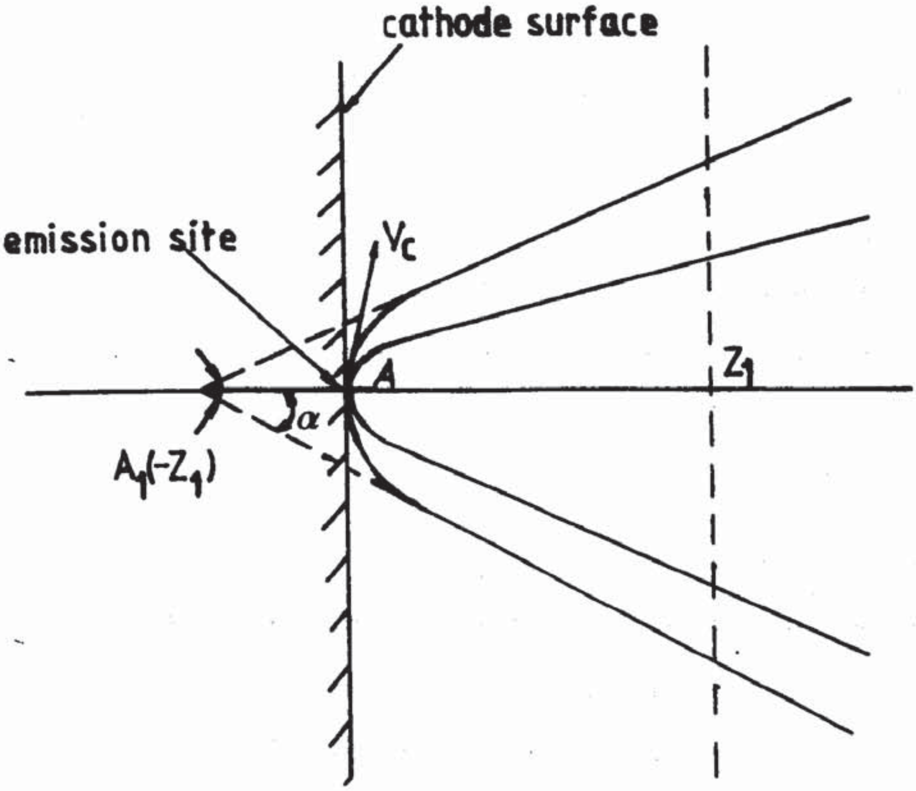

Fig. 4.9 A schematic representation of the features of an emission objective.

from a point-like source (site) on the surface of a cathode will form a divergent pencil beam since they are not only likely to leave the surface with a range of initial transverse velocities, but they will also be subject to a local diverging field. The experimental approach described above can therefore only measure how many times the final beam divergence is magnified, since a displacement of the cathode does not change the local emission regime. To obtain a more detailed perspective of the "local" image magnification effect, it is necessary to consider the known features of an emissive object. Firstly, since the initial electron velocities will be very low (corresponding to energies of the order of a few tenths of an electron volt) and the macro-field is assumed normal to the surface (which is equivalent to being parallel to the axis), very intense and almost uniform, the initial trajectory will be parabolic in shape, and the velocity changes direction very rapidly along the curve until it becomes nearly parallel to the axis in a plane $z=z_1$, as shown in figure 4.9. In this plane, rays which have in fact originated from a point on the cathode such as A (see figure 4.9.) appear to be coming in a straight line from a small disc around A_1, situated at $z=-z_1$, and of radius $r=(2D_c)/F_c$; here D_c is the voltage equivalent to the most probable initial electron velocity, and F_c is the local micro-field on the cathode [100]. Thus, assuming that $F_c=10$ MV/m and $D_c=0.1$ V, the radius of this disc will be $\sim 0.02\mu m$. Furthermore, since D_c could be expected to increase with E_c in our case, the radius r can be assumed to be remain approximatly constant. The angular aperture of the beam corresponding to each point on the cathode is given by $2\alpha = 2\sqrt{\frac{D_c}{F_c z_1}}$, where $z_1=d/3$, in which d is the inter-electrode, or gap spacing [100]. The angle α is calculated to be less than 1^o so that the radius of the beam in the plane where the divergent lens becomes effective is approximately 0.02 μm. Secondly, as can be seen in chapters 3 and 6, local micro-field intensification would occur at an emitting area and the modified field lines would reinforce the divergence of the electron beam. From this analysis it can be seen that an exact determination of the total magnification would have involved a very much more complicated electron optical experiment which was considered to be beyond the scope of this project. However, its approximate value is available, from an indirect measurement made during the calibration of the system in the course of this programme. Here, the image of a tungsten tip having of a diameter of 10 μm was observed to be ~20 mm diameter thus giving magnification of ~2000.

The resolution of this system is given by the following relation [100]:

$$\delta = k_r \frac{\zeta_c}{F_o} \qquad (4.8).$$

in which ζ_c is the most probable energy of the emitted electrons (measured in volts), and F_o is the electric field at the cathode (only considering the macro-field); k_r is a constant having a most likely value of 1.2. Therefore, assuming $\zeta_c = 0.1$ V, the resolution of the system is calculated to be $\delta = 1.2 \times 10^{-8}$ m= 120 Å for the lowest applield macro-field of $F_o = 10$ MV/m.

4.2.6. The resolution of the analyzer

The technique of directly measuring the resolution of a field emission analyzer from an electron energy distribution was first described by Young and Kuyatt [101]. They assumed that the energy analyzer has a Gaussian transmission function given by

$$G(E) = \frac{0.949348}{\Delta E_{1/2}} \exp\left[- \frac{2.772588E^2}{(\Delta E_{1/2})^2} \right] \qquad (4.9)$$

where $\Delta E_{1/2}$ is the analyzer width and G(E) is normalized. The effect of analyzer smearing is calculated by folding the assumed Gaussian transmission function $G(E'-E)$ into the field emission energy distribution P(E)dE, thus

$$J(E) = \int P(E')\, G(E'-E) dE' \qquad (4.10)$$

so that J(E) is the measured electron energy distribution. Since the leading edge of the above distribution suffers the greatest distortion, due to the influence of the analyzer transmission function, the difference in energy between the 10% and 90% points on the leading edge of the energy distribution has been chosen as the pertinent parameter. Figure 4.10 reproduces their results, where the analyzer width is represented as a function of the measured energy difference between the 10% and 90% points in the leading edge of the energy distribution. This approach assumes, of course, that the energy distribution is obtained from an ideally clean tungsten emitter. In fact, Braun et.al. [97] have shown this edge to be very dependent on surface contamination and were only able to obtain a high energy slope width of 0.11 eV against a theoretical value of 0.10 eV after thorough cleaning of the emitter by field desorption; using figure 4.10, this gives an analyzer width of 50 meV. However, by comparing this with those of Young and Müller [102], they concluded the analyzer width is < 30 meV. Athwal [58] also checked this result after an instrumental modification to make spectral measurements from broad-area cathodes, and claimed that the modification did not influence the resolution of the analyzer.

fig. 4.10 The plot of analyzer FWHM against the high energy edge of its measured energy distribution. (from Young & Kuyatt [101]).

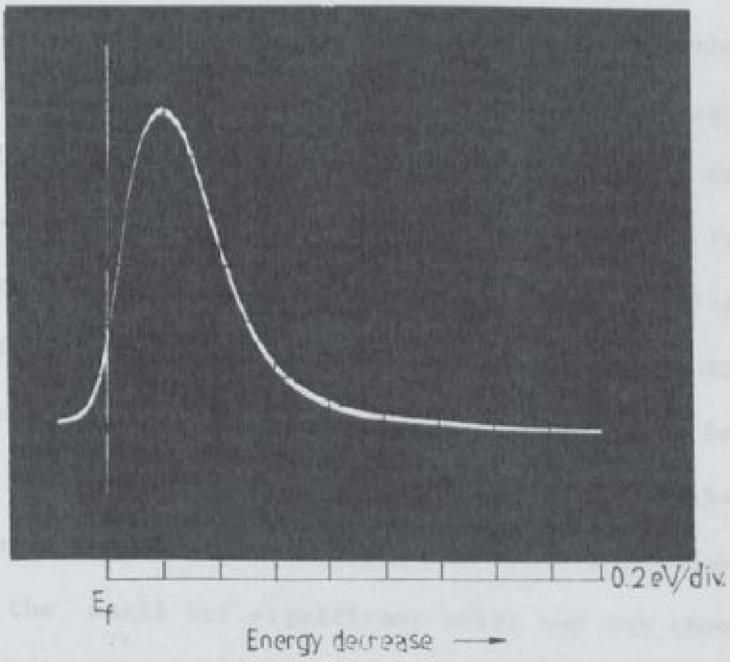

Fig. 4.11 An electron spectrum from a reference tungsten emitter.

4.2.7. The calibration of the analyzer

If the Fermi level of a metal is taken as zero potential, any electron at rest in vacuum just outside the metal will have a potential Ψ equal to the work function of the metal. Since a metallic cathode and the hemisphere of the analyzer are connected together, their Fermi levels should be at the same energy position. Therefore, under normal circumstances, i.e. with the cathode earthed, the hemispheres with a work function Ψ and a mid potential V_4 , the kinetic energy of an electron emitted from the Fermi level of the cathode will be

$$E = eV_4 - \Psi.$$

Young [49] predicted theoretically that for the typical operating conditions of a tungsten emitter where $F = 4.5 \times 10^9$ V/m and $\Psi = 4.4$ eV , the Fermi level occurs at a point 73% up the high-energy slope of an energy distribution recorded at room temperature (300K). Based on this theoretically derived result, Braun et.al. [97] measured Ψ to be 4.23 ± 0.03 eV, and this was subsequently checked by Athwal [58] after modifying the instrument. At the beginning of this research programme, a further check was made on this parameter since there was a suspicion that the work function of the analyzer had altered. From the result shown in figure 4.11, a point 73% up the high-energy slope was found to be shifted by ~ 0.08 eV below the previously determined Fermi level; furthermore, repeated cleaning failed to give a better result. However by examing the distribution it can be seen that its FWHM is ~0.38 eV, thus indicating that the tip was still contaminated [97,58]. Therefore, the small but significant shift was not thought to result from a change in the analyzer work function Ψ , but rather as a consequence of adsorbates on the emitting surface.

4.2.8. The electromechanically-controlled specimen scan system

The complete system is illustrated schematically in figure 4.12. In this, the mechanical drive for the x-y movement of the specimen stage is provided via two 220 V dc motors and a 50:1 worm reduction gear box. This motion is transmitted to a cathode in the vacuum chamber via a bellow-linked rigid rod [31], and is controlled by an electronic system (see figure 4.12) which has been described in detail by Bayliss [32]. In essence, it consists of a motor-driven unit and a spiral scan generator, in which the operation of a motor is determined by whether or not a potential difference between a preset value of potential of a control potentiometer and that of linear potentiometers driven directly by the specimen stage, which is proportional respectively to the x and y co-ordinates of a specimen position. Thus, when two voltage sequences, $V_{x(t)}$ and $V_{y(t)}$, derived from the scan voltage generator, are fed respectively to the x- and y-drive circuit, the specimen is caused to be scanned in a spiral pattern in the x-y plane.

To obtain a map of emission sites on the surface of a specimen, an anode probe current is used to control the z-modulation of a synchronously scanned storage oscilloscope. This current can be collected by either the lens electrode or the electron multiplier, which respectively give low or high resolution maps of a site distribution. In the low resolution mode, the resolution is limited by the anode probe hole whose diameter is 0.5 mm, whilst in the high resolution mode, the resolution is limited to ~100 μm, which corresponds to the minimum spot-size of the recording oscilloscope.

4.2.9. Photo-stimulation and electroluminescence studies

The experimental arrangement used for these optical studies is

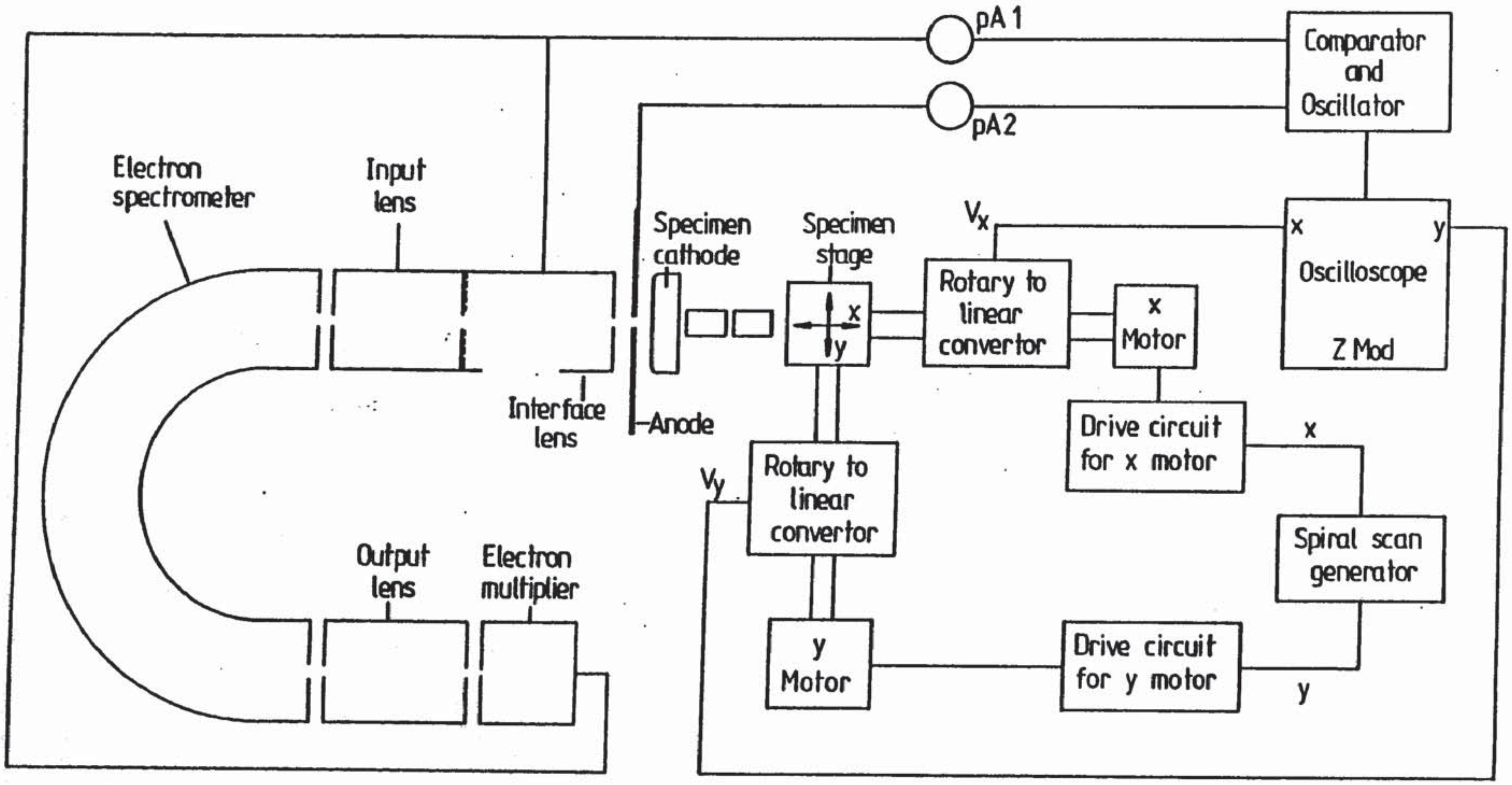

Fig. 4.12 A schematic illustration of the specimen scan system.

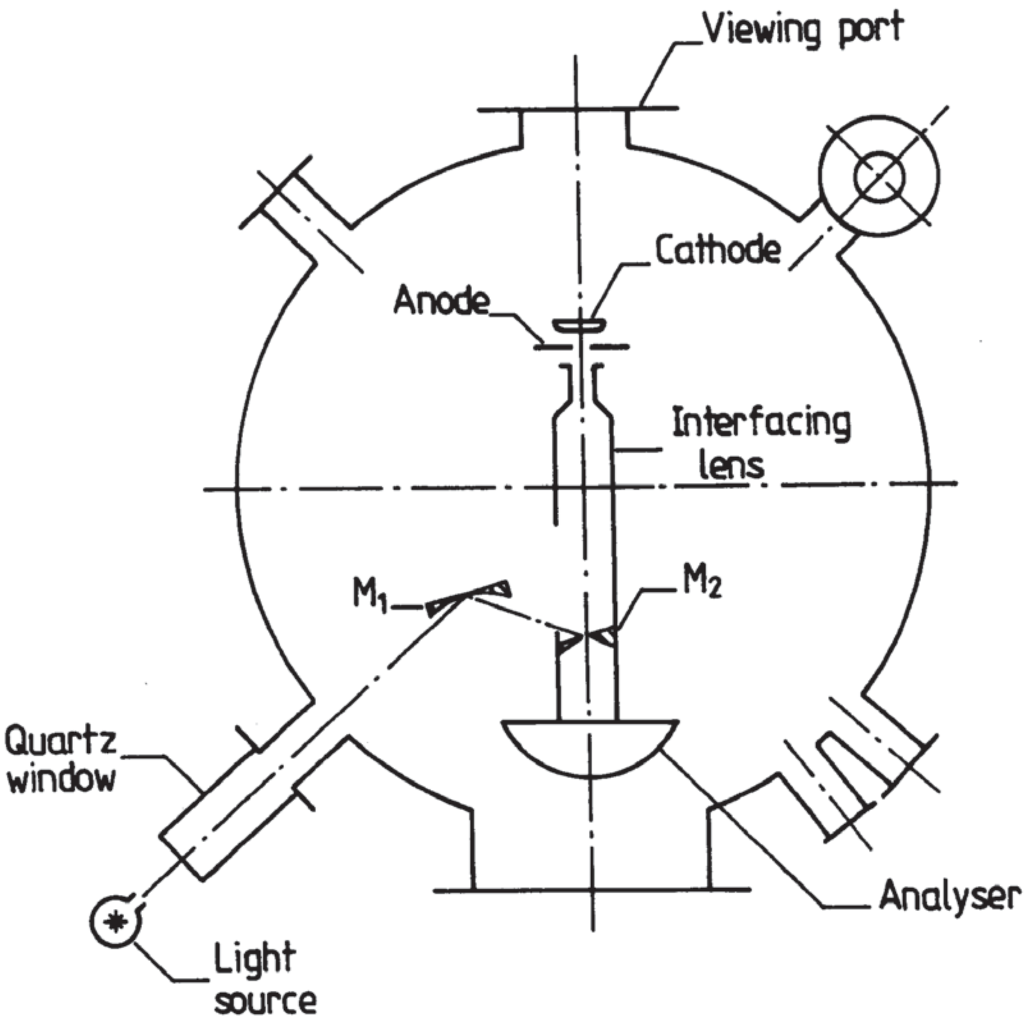

Fig. 4.13 The arrangement for the optical measurement.

shown schematically in figure 4.13 ; this includes both an optical lens system for delivering light from an external source to an emission site on the cathode, and a mirror system for observing optical activity on the cathode, which is a development of the system used by Bayliss [32]. The aim of this study was to observe the effect of photon stimulation on both the emission and particularly on the energy distribution. Thus, a commercial mercury-discharge lamp was used as a source of UV-photons, and was located just outside the chamber, behind a quartz window (which is transparent to the ultroviolet light). The radiation leaves the discharge tube through a 0.8 cm wide and 1.5 cm long slit. The distances between two deflection mirrors and their curvatures were carefully chosen so that the system gave a 1/30 demagnified image of the slit at the anode probe hole. Since this image was larger than the anode probe hole, the practical focusing procedures were eased. With this consideration, mirror M_1 with radius of 9.5 cm, 27 cm from the source, and 6 cm from M_2 reflected the light from the source to give an image at M_2, whilst M_2, of radius of 1.4 cm focused the light to a site 81 mm from its centre. From electron optical considerations, the back face of M_2 was machined concave so that the thickness of the electrode in the region around the aperture was maintained at about 1 mm in order to maximise the transmission of the electron beam. Conversely, if the light source is replaced by a photo detector, it follows that any optical processes associated with an active emission site can be observed with essentially the same optical system, but used in reverse.

4.3. The electron energy-selective display technique

It became obvious from the first series of experiments of this programme, (see section 5.2 and 5.3) that the electron images of emission sites may be broadly divided into two classes. As previouly defined, the first is characterised by a group of apparently independent sub-spots, whilst the second generally consists of several geometrically-shaped segments: in both cases, the electrons from each of these subspots or segments form a single peak energy spectrum. By establishing broad similarities between the images of this second class of site and those observed from purpose-fabricated MIM electron sources [8] , which have been described in section 3.3.4, it was concluded that the electrons which form a "geometrical" image escape into the vacuum by a field-induced hot-electron coherent scattering mechanism at a naturally occuring MIM microstructure. In order to investigate the mechanism in more detail, it was decided to improve the spectrometer facility to include an electron energy-selective display technique for the study.

4.3.1. The principle of the electron energy-selective display technique

The electron energy-selective display techinque is illustrated schematically in figure 4.14. As described previously, electrons passing through the anode hole are focussed to form an image on the phosphor screen deposited on the front face of the electrode that forms the input aperture of the spectrometer. By using an X-Y electrostatic deflection system located within the interfacing lens module, the electron image can be systematically scanned in a raster pattern against the probe hole. The spectrometer then acts as a "filter" which only transmits those electrons passing through the probe hole which have an energy within its energy "window". These electrons are detected by a single channel electron multiplier whose signal is fed into a storage oscilloscope and used to "bright up" its screen. Thus, by synchronously scanning the storage oscilloscope with the deflection system in the interfacing lens, the transmitted electrons within a selected energy range will be recorded as a bright image on the screen of the scope, and hence generate a visual image of their spatial distribution on the screen of the oscilloscope.

4.3.2. The electrostatic deflection system

In order not to perturb the electron optical performence of the existing spectrometer facility, it was highly desirable to minimise changes to the lens system when designing a suitable scanning system. It was therefore firstly necessary to decide whether to use an

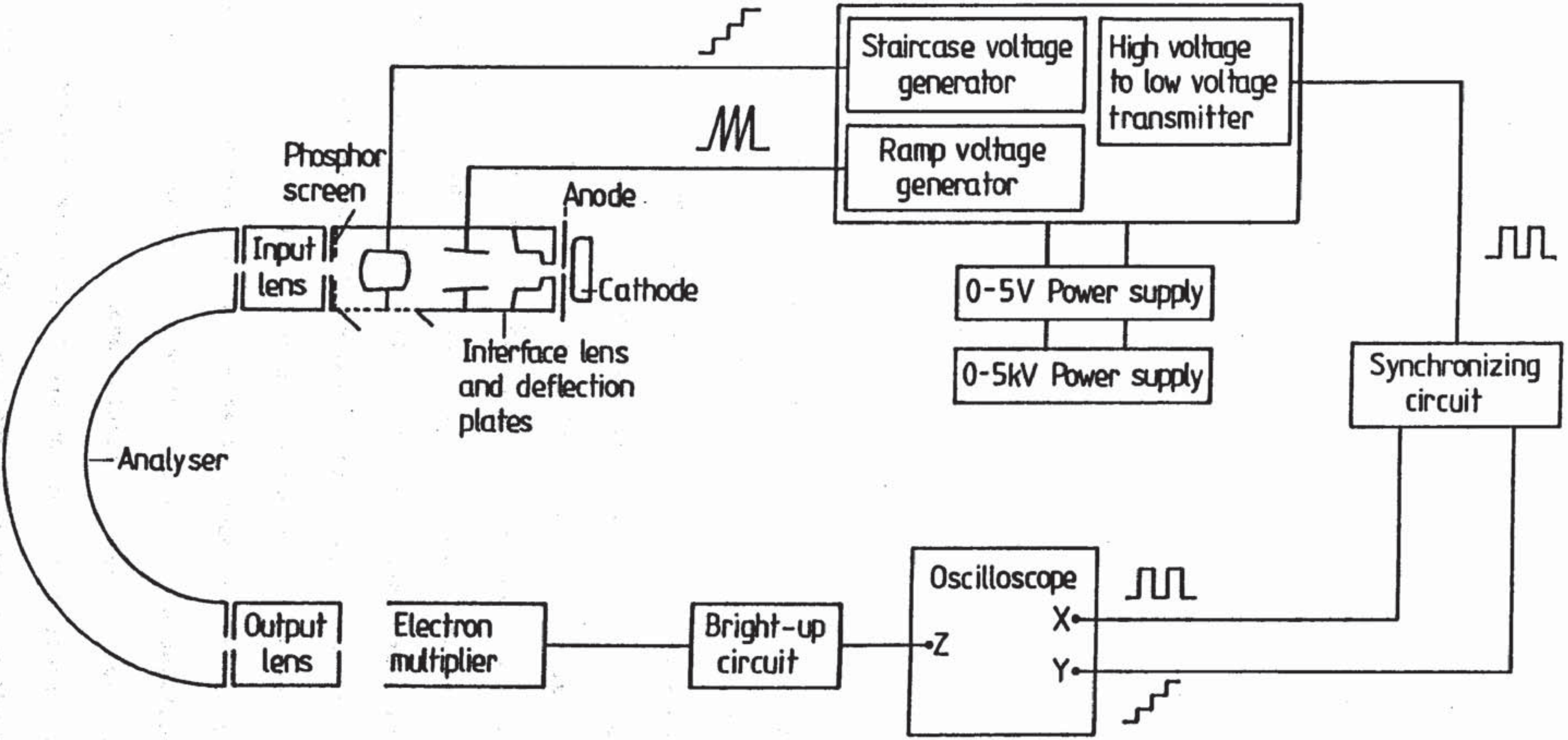

Fig. 4.14 A schematic illustration of the electron-energy selective display facility.

electrostatic or magnetic deflection system. In fact, the latter alternative was rapidly eliminated since any strong magetic field near to the analyzer would almost certainly influence its normal operation. Having thus settled on an electrostatic deflection system, it was then necessary to decide whether the plate assembly should be mounted within the input lens or interfacing lens.

After studying the design features and the operational principles of these two lenses, it was found that the latter was more suitable to accommodate the deflection system. This is illustrated by figure 4.7 which shows that there is a field-free region between the second anode and the screen where a deflection system can be inserted without significanly influencing the properties of the lens system. In addition, since the interfacing lens is of a projection type, as illustrated by figure 4.15, which reproduces the result of a computer simulation of electron trajectories in this lens, most electrons travel to the screen in the direction that diverges by a small angle from the axis of the lens. Thus, only axial electrons can satisfy the optical requirement of the input lens since, for its best focussing, the input electron beam should be parallel to its axis. Therefore, the additional advantage of using a deflection system within the interfacing lens is that it can electronically deflect an electron beam to the aperture hole with a near zero angle against the axis, as shown by figure 4.16. Furthermore, figure 4.15 is very useful for estimating the possible maximum diameter of a beam, since for the purpose of the design it only needs information about the divergent properties of the lens. However, it should be mentioned that since in figure 4.15 only those electrons emitted without tangential velocities were considered, it may not be a very close simulation of the trajectories of the electrons emitted from the regime we are concerned about: this has been discussed in section 4.2.5.

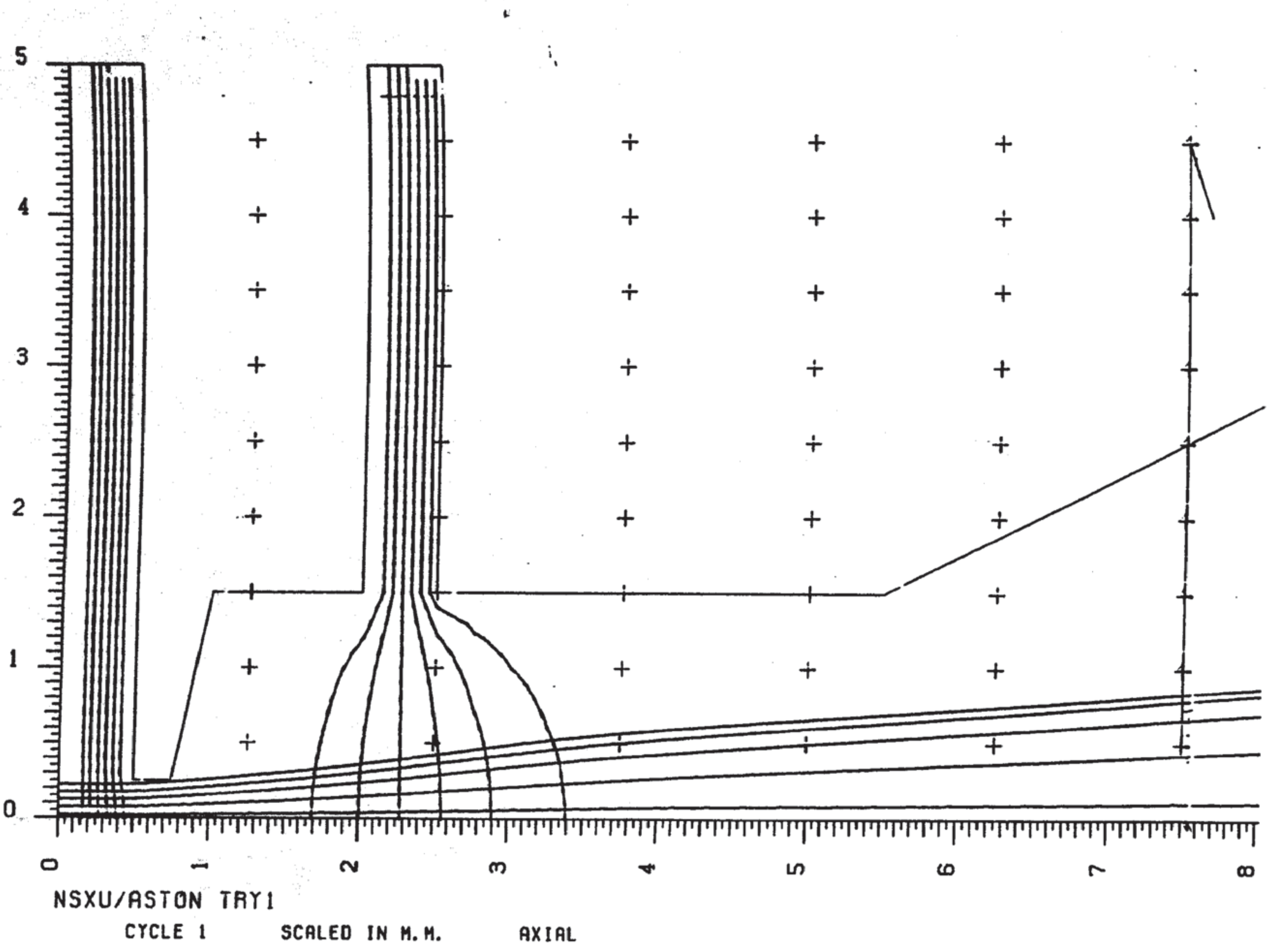

Fig. 4.15 The electron trajectories within the interface lens.

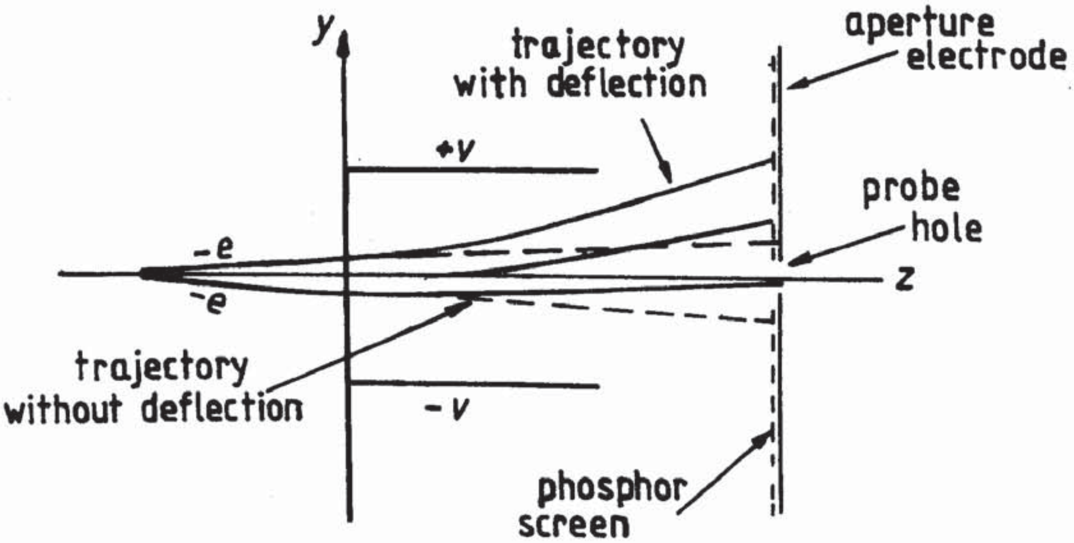

Fig. 4.16 A schematic illustration of the behaviour of deflected electron beams.

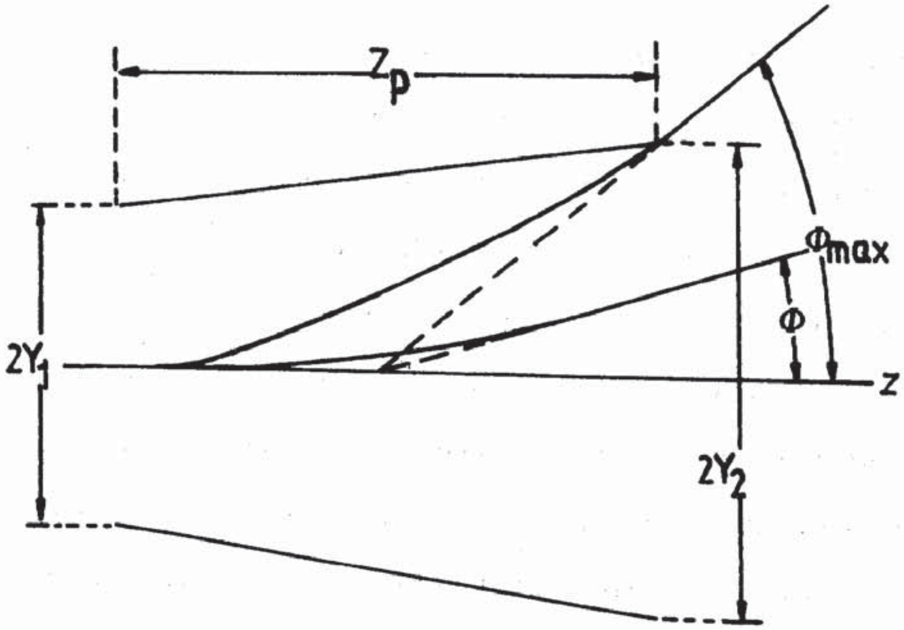

Fig. 4.17 A schematic illustration of the dimensional parameters of the deflection system.

Later tests on the deflection system have shown that this consideration is correct, since it performs satisfactorily. We take the outermost possible electron as the example in the following calculation. Thus, firstly the angle of the direction of the electron is determimed by

$$\Phi_{max} = tg^{-1}\left[\frac{6}{80}\right] = 4.3\ (^{o}) \tag{4.11}$$

where 6 mm is the displacement of the electron on the screen, whilst 80 mm is the distance between the second electrode and the screen.

Having thus established the basic properties of the interfacing lens, it is now possible to start designing a suitable deflection system. According to Knoll [103], the power G of a defection system can be defined as

$$G = \frac{Z_{eff}}{2Y_{eff}} \tag{4.12}$$

where Z_{eff} and $2Y_{eff}$ are the "effective" length and "effective" separation, respectively, of an ideal parallel-plate deflecting system producing a strictly homogeneous field of limited length. Obviously, the deflecting power increases with decreasing plate separation, or increasing the length of plates. If, however, for a required deflection, the separation is reduced too much, the electron beam will be trimed by one of the plates. On the other hand, if the deflecting field is too strong, the associated fringing field may damage the focal properties of the lens, so that the resulting electron image may be distorted. In our case, the total distance available for the deflection system is 78 mm, i.e. between the second anode and the screen. Thus, it is impossible to have a long plate-length. In addition, it is difficult to reduce the separation of plates too much, because the diameter of the electron beam in the present projection type of lens is rather large; for example, it will be seen from figure 4.15 to be 12 mm in the plane of the screen.

Having considered these two factors, it was firstly decided that to avoid the effects of the fringing field, it was necessary to set the distance between the second anode electrode and the first pair of deflection plates to be 10 mm, and that the axial distance between the two pairs of deflection plates to be 3 mm, and consequently the distances between the second anode and the exit or entrance of the deflecting plates can be determined. Secondly, the separations of the pairs of plates were estimated according to (4.11). These results are summaried in table 4.1.

Table 4.1. unit: mm

distance	28	38	41	68
diameter	2.1	2.9	3.1	5.1

NB.

1) "distance" is measured from the second electrode.
2) "diameter" means the displacement from the axis of the outmost electron.

In order to scan the whole electron image over the aperture hole in the input lense, an axial electron should be scanned about the axis, over a distance at least equal to ± the radius of the imaging cone in the plane of the screen. Thus, the separations of the deflecting plates were set to be equal to the twice the diameter of Table 4.1. Thus, all the parameters of the deflection system could be defined, and are listed in Table 4.2, where the meaning of the parameters is illustrated by figure 4.17.

Table 4.2. unit: mm

y_{1x}	y_{2x}	z_{px}	y_{1y}	y_{2y}	z_{py}
2	6	10	6	10	27

Then, assuming initially that the deflecting plates have a parallel geometry, the maximum applied voltages necessary for producing the desired deflection can be estimated as follow [103]. Since

$$G = tg\,\Phi_{max}\left(\frac{V_{el}}{(V_p)_{max}}\right) \qquad (4.13),$$

and,

$$(V_p)_{max} = tg(\,\Phi_{max})\left(\frac{V_{el}}{G}\right) \qquad (4.14)$$

where Φ_{max} is the maximum angle through which the beam can be deflected without fouling the plates (which can be calculated from the parameters given in Table 4.1), $2(V_p)_{max}$ is the maximum possible deflecting voltage difference between the plates, and V_{el} is the initial electron energy. Thus, taking the average value of the separation of x-plate as the effective separation, i.e.,

$$Y_{eff} = \frac{Y_{1x} + Y_{2x}}{2} \qquad (4.15)$$

$$= 4(mm)$$

we then have, according to (4.12),

$$G_x = \frac{10}{8} \qquad (4.16).$$

since

$$tg(\Phi_{max}) = \frac{6}{45} \qquad (4.17),$$

with $V_{el} = 3$ kV. Finally, by substituting these values into (4.14), the maximum possible deflecting voltage difference for x-plates is calculated to be equal to 640 V. A similar calculation leads to the maximum voltage difference for y-plate to be 850 V. Therefore, in a practical design, adjustable voltages that have a maximum limitation of 900 V for both sets of plates would satisfy the above requirements. To reduce these voltages, the plates were curved in a parobolic profile. As a result, the separations of the plates on their exit sides are slightly larger than the calculated values in Table 4.2.

4.3.3. The electronic control drive-system

In order to electrostatically deflect the electron beam in a raster pattern, it was necessary to design and build an appropriate electronic drive system. This will now be described in detail below.

4.3.3.a. The signal generator

To generate a raster scan pattern, it is necessary to provide the x-deflection plates with a ramp signal, and the y-deflection plates with a staircase waveform voltage; it follows that there must be a strict time relationship between these two signals. The unijunction transistor circuit designed for generating these signals is shown in figure 4.18. It is similar to a common unijunction transistor circuit, but instead of using a resistor in the emitter line, the transistor T_1 is used to provide current. A Zenor diode clamps the

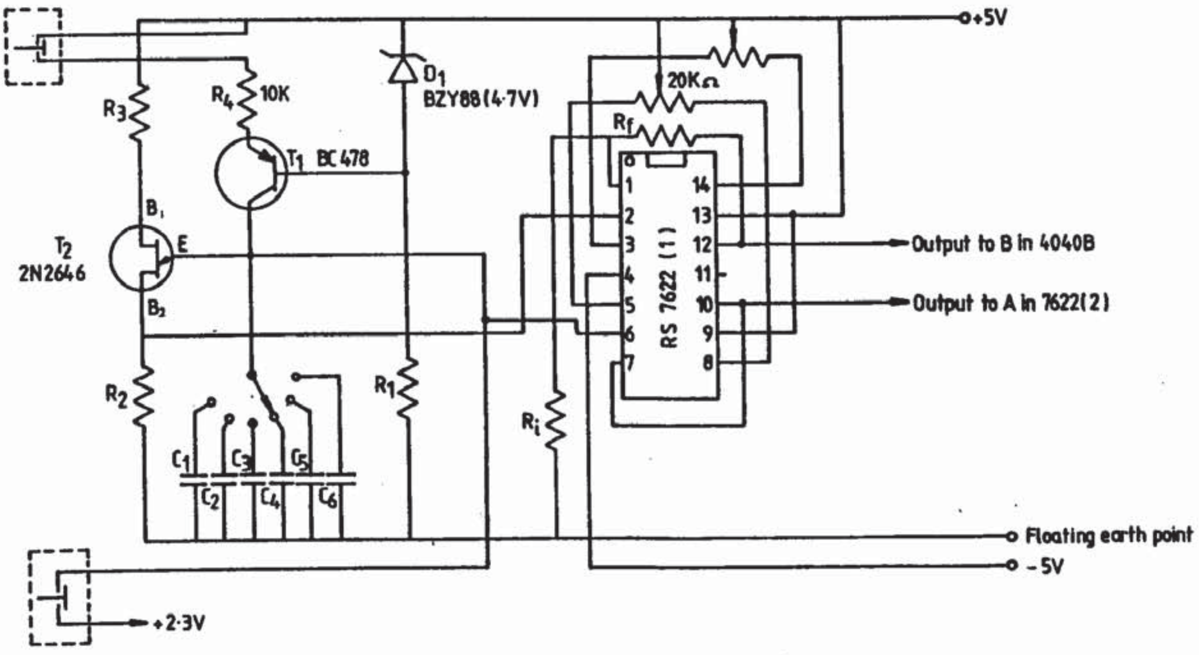

Fig. 4.18 The circuit diagram of the signal generator.

voltage across the base and the emitter to ensure that the output current of the transistor remains constant at a value of 0.5 mA. The frequency of the output signals from the circuit is determined by the values of both this current and the capacitors; i.e.

$$\nu = \frac{I}{CV} \qquad (4.18).$$

By arranging for there to be a selection of six capacitors, it follows from equation (4.18) that there is a choice of six different operating frequencies; viz. 0.33 Hz, 0.66 Hz, 2 Hz, 3.3 Hz, 6.6 Hz and 20 Hz. The lowest two frequencies were used most often in this experimental programme; however, it is anticipated that the others will be used in future developments when a computer will be interfaced for storing the data. As shown in figure 4.20, the unijunction transistor provides three different output signals: (a) a ramp from E, (b) a positive pulse from B_1, (c) a negative pulse from B_2. The two required signals, viz. a positive pulse and a ramp, are fed into a double op-amp 7622 which buffers the next stages. One of op-amp´s was designed as a "follower with gain" so that a positive pulse can be amplified to 5 V.

4.3.3.b. The staircase waveform generator

As indicated above, the vertical scanning facility requires a staircase waveform voltage. This is generated by the DA (digital-to-analogue) converter function generator circuit shown in figure 4.19. The counter 4040B counts the number of positive 5V pulses taken from output B of the "follower with gain" shown in figure 4.18, and gives a binary output. The DA converter (DAC0800) is a multiply type that should be incorporated with an op-amp (i.e. 7611 in figure 4.18) to give a voltage output. According to the binary output of the counter, the DA converter outputs different values of current. However, the output voltage V from the op-amp will take the following general form:

$$V = \sum_{m}^{N} X_m \left(\frac{1}{2} \right) IR \qquad (4.19)$$

where X_m takes the values 0 or 1, as determined by the binary output of the counter, whilst I is minimum output current. Since the full scale output current I_{fs} can be determined by

$$I_{fs} = \frac{V_{ref} \times 255}{R_{ref} \times 256} \text{ (mA)} \qquad (4.20),$$

where $R_{ref} = 5\ k\Omega$, $V_{ref} = 5$ V, then I can be determined from $I_{fs}/256$, i.e. 1/256 mA. It follows that the voltage difference between two sequential "steps" is 15 mV.

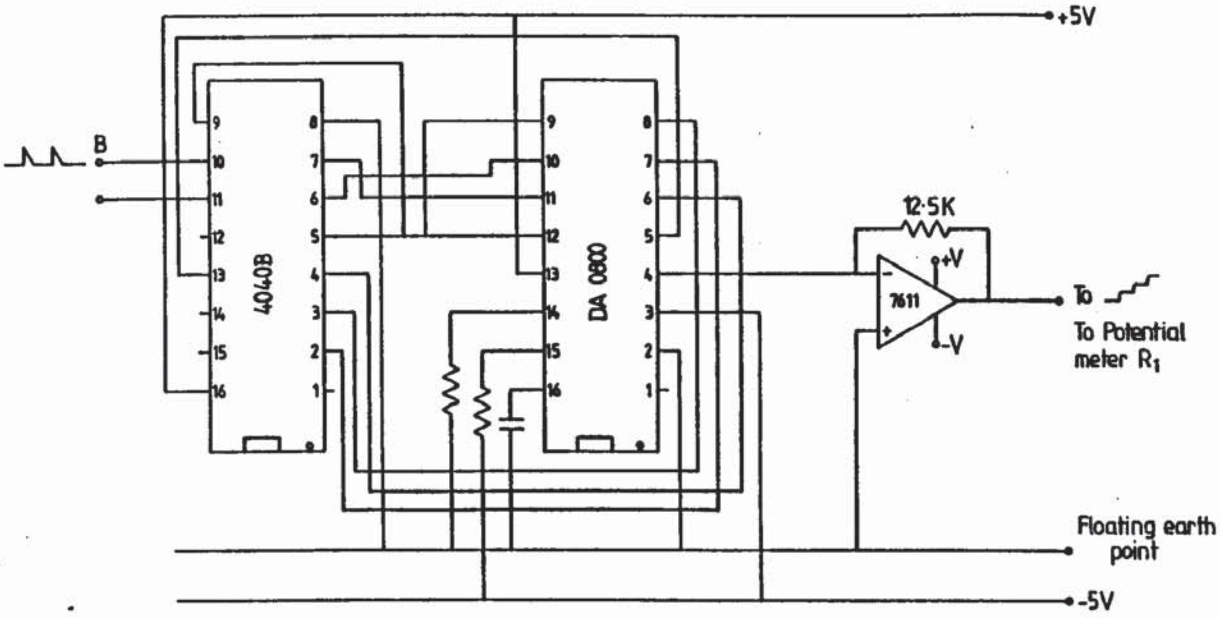

Fig. 4.19 The circuit diagram of the staircase waveform generator.

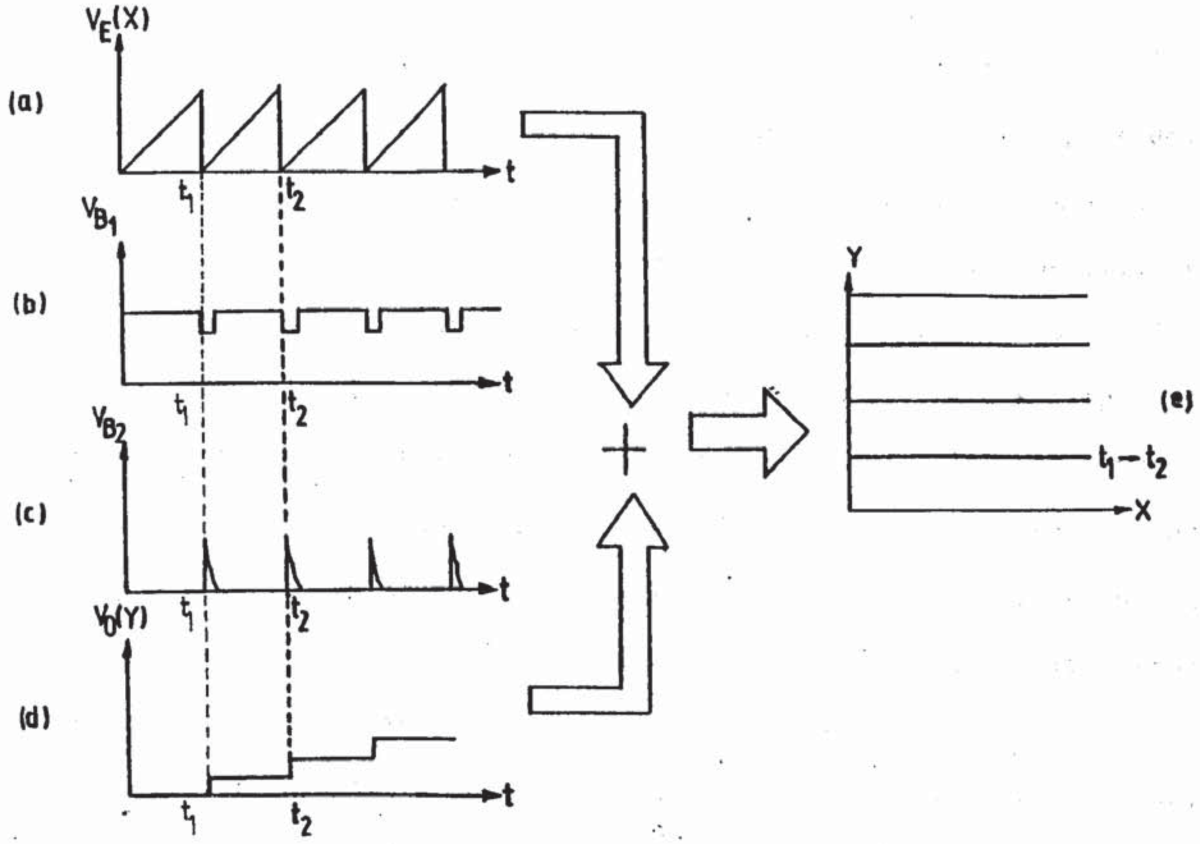

Fig. 4.20 The schematic illustration of forming of the raster scan pattern.

4.3.3.c. Forming the raster scan pattern

Having generated both the ramp and staircase waveform voltages, the ramp signal is fed to the x-deflection plates, and the staircase signal to the Y-deflection plates. Then, as shown in figure 4.20, when the ramp signal drops from its maximum to minimum value, a positive pulse is simultaneously generated, so that the output of the DA function generator "moves" up one step, i.e. since the counter 4040B responds to the rising edge of the positive pulse. This output is maintained while the ramp signal rises from its minimum to maximum value until next collapse of the ramp signal again leads to a position pulse; and the process repeats itself. As a result, the electron beam is scanned in a raster pattern as illustrated schematically in figure 4.20a, d and e.

4.3.3.d. The control circuit

This is shown in figure 4.21, and has the function of either starting or stopping the scan sequence or varying the scan amplitude. To start or stop the scan, the emitter of the uni-junction transistor, and its output to the next stage, are simultaneously cut off, or connected by the electronic analogue switch 4016B that is controlled by the J-K flip flop 4027B. When the output Q of the J-K flip flop suddenly goes high, the scan will start; conversely, it stops. Therefore, to start the scan, the 4027B must be manually enabled by giving a positive pulse to its clock input (CP). This involves using an opto isolator, since this enabling signal must be transmitted from the low potential stage to the high potential stage. This opto-isolator adopts a configuration of a LED and a phototransistor, and thus can isolate a high voltage of at least 4 kV. In the circuit

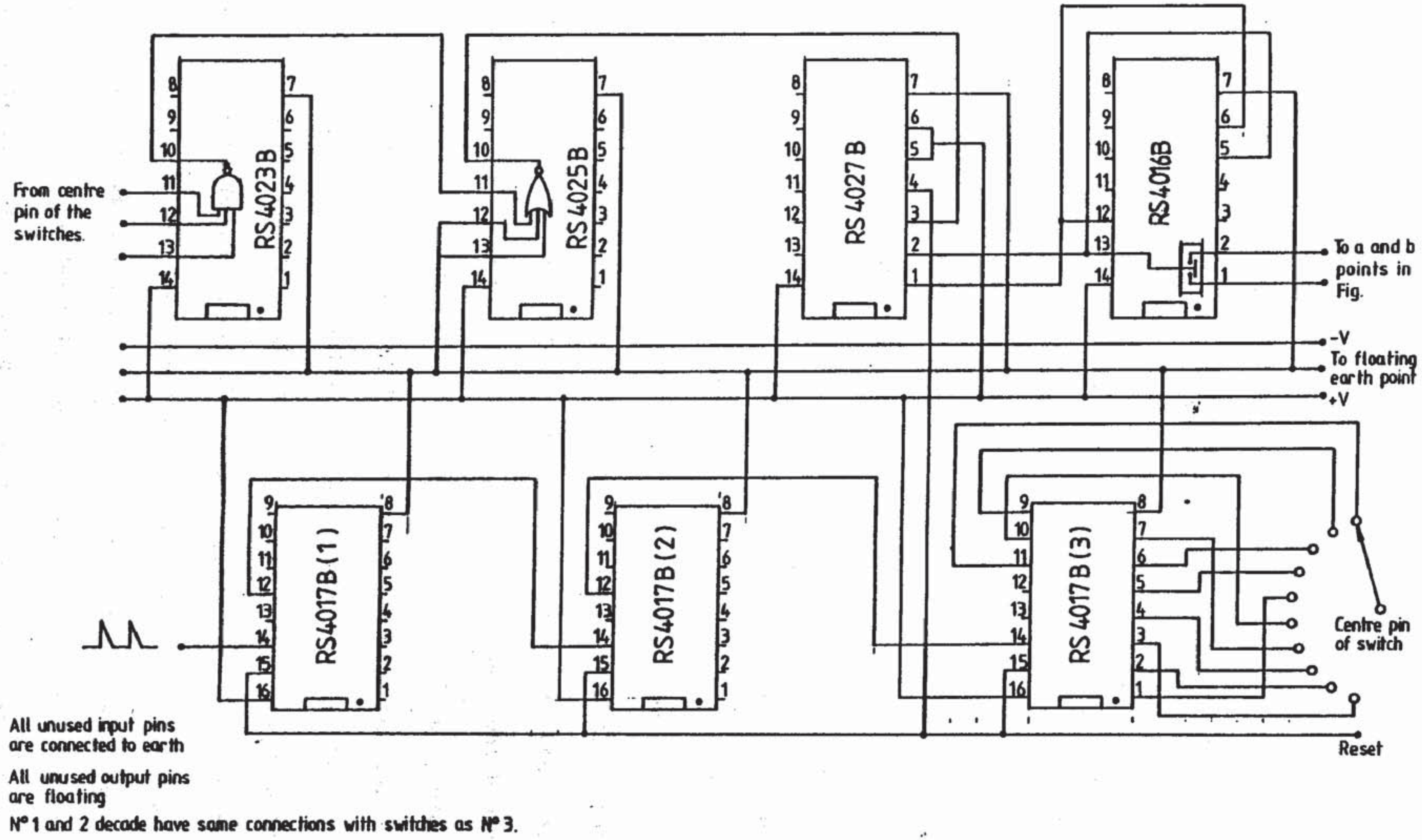

All unused input pins are connected to earth

All unused output pins are floating

N°1 and 2 decade have same connections with switches as N°3.

Fig. 4.21 The circuit diagram of the control unit.

shown in figure 4.22a, the LED operates in the low voltage side, while the phototransistor in the high voltage side. Once the switch 1 is closed, the LED illuminates and then transmits 20% of current to the phototransistor. Subsequently, the phototransistor receives this signal and generates a current so that a voltage of 5 V is developed across the resistor R. Therefore, whenever the switch S_1 is pressed, a positive pulse is sent to the reset pin of the 4027B to toggle the Q output, and consequently the electronic anologue switches are opened or closed. For the stop function, there are two modes, i.e. automatic and manual stop. To stop manually, it is only necessary to press the switch 1 and thus bring the output $\bar{Q}$ of the 4027B to a high voltage level. To stop automatically, a reset signal of the 4027B comes from a NOR gate of the 4025B and a NAND gate of the 4023B which are controlled by three decades (4017B). Three decades accumulate the number of positive pulses and represents them in hundreds, tens and one units in decimal system respectively. Since the maximum number of scan lines in one frame is two hundred and fifty six, it follows that three decades are necessary. The output pins of the decades are connected with decimal number preset-switches which have reading numbers corresponding to the representation of the decades. The central pins of the switches are connected with the three inputs of the NAND gates of the 4023BW. If the number of scans is preset by the switches, the output of the NAND gate will become low when the numbers in all three decades reach the preset number, and will bring one of the input of NOR gates to low voltage level. Since the other inputs are already "grounded", the output of the NOR gate will go high and thus enable the J-K flip-flop to toggle the $\bar{Q}$ output to high, and so automatically stop scanning. It follows that this function also allows changing the scanning number in the vertical direction, and

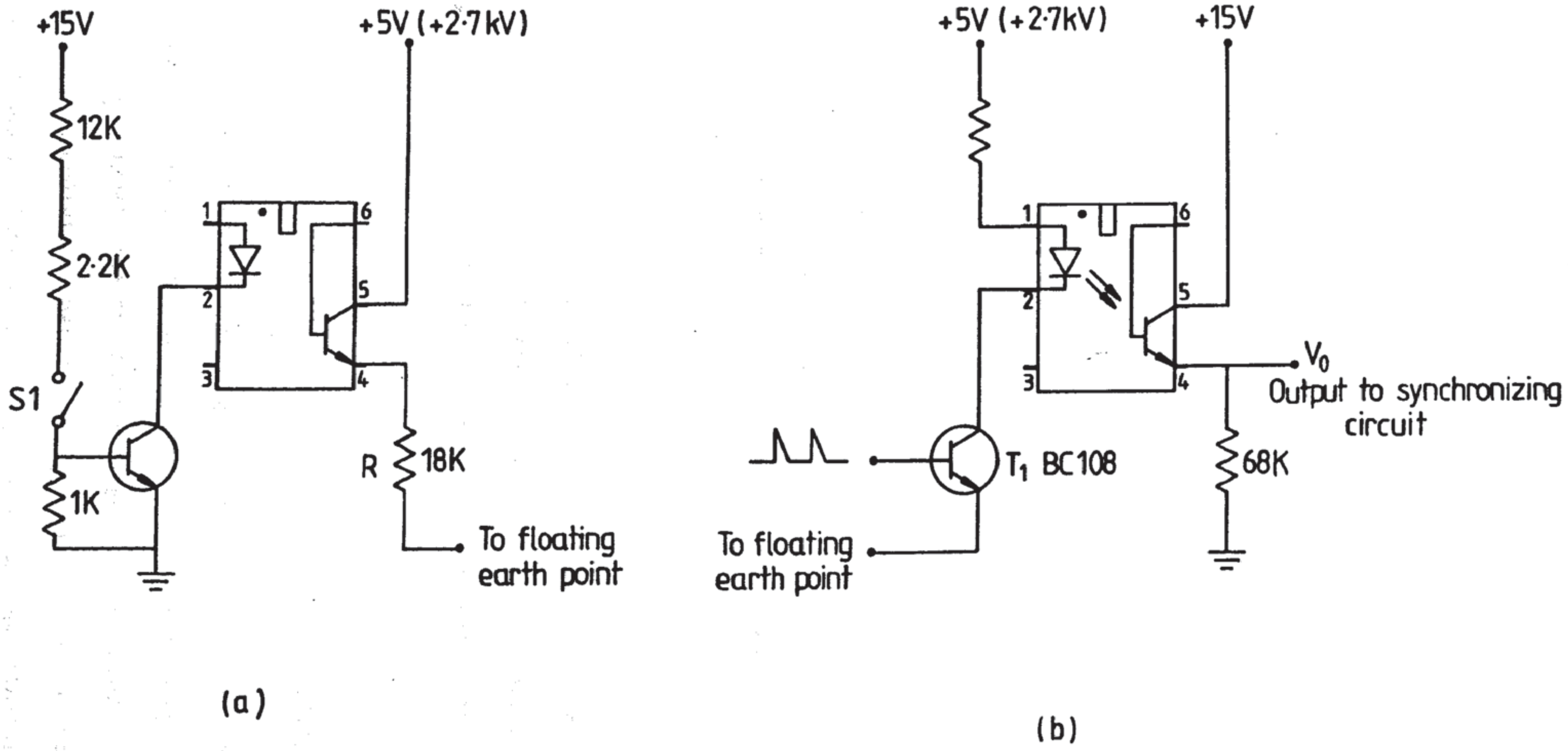

Fig. 4.22 The circuit diagram of the interface units between the high potential and low potential circuits.

thus changing the vertical scanning range.

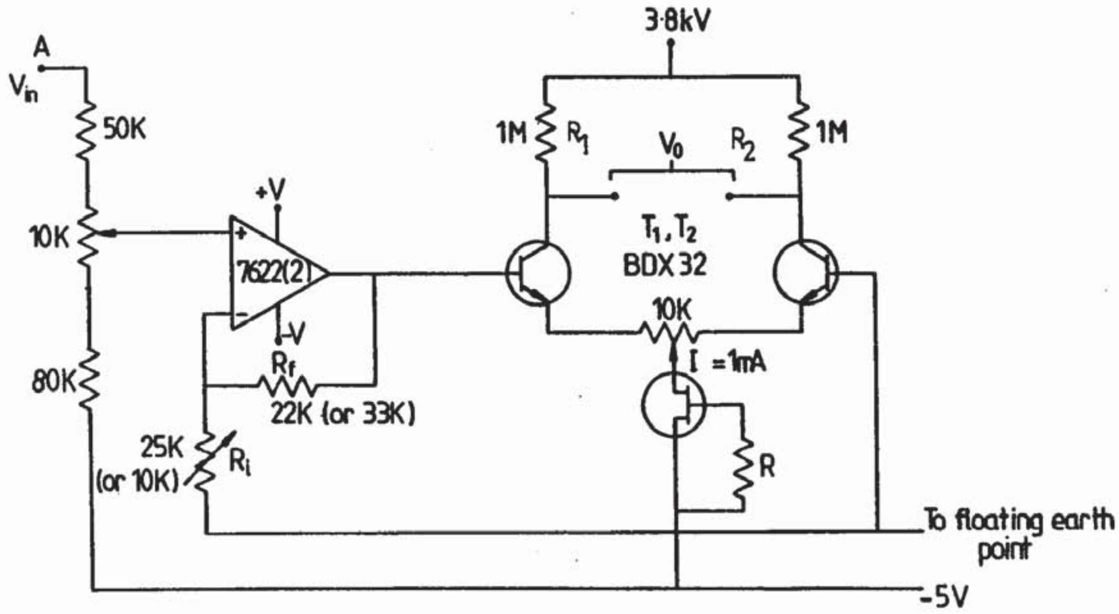

Fig. 4.23 The circuit diagram of the output stage.

4.3.3.e. The output stage

This is shown in figure 4.23, and is replicated for the two pairs of the deflection plates. It consists of a voltage-follower and a long-tail pair. The voltage-follower is constructed from an op-amp (7622) with a gain of

$$A = \frac{R_i + R_f}{R_i} \qquad (4.21),$$

which can be varied from 1.5 to 4 by adjusting the potentialmeter R_i; this stage therefore not only buffers the next stage but also amplifies the signal from the former stage. An in-coming signal goes through a voltage-divider before being fed to the input of the voltage-follower. This arrangement provides the flexibility for adjusting the scan centre. This is necessary for either positioning the analysed image at the centre of the oscilloscope screen or positioning any desired region of the image over the aperture hole of the spectrometer in order to record an electron energy spectrum. The long-tail pair was constructed from transistor T_1 and T_2, resistor R_1 and R_2, and a constant current source (RS3142), where T_1 and T_2 can handle a maximum voltage of 1.7 kV across their collector and emitter. The current source was designed to provide a constant current of 1 mA for one long-tail pair and ensure the linearity of its output. All the load resistors are 2W carbon film resistors in order to avoid any possibility of breakdown, even when the designed maximum voltage of 800 V is applied across them.

4.3.3.f. The power supplies

The drive circuitry described above requires both a low voltage and high voltage power supply, as shown in figure 4.24. The former supplies all the circuits described above. It has two outputs: i.e., a voltage of +5 V via a regulator RS317L which has an input from a battery of any voltage ranging from 5 V to 40 V and a voltage of -5 V via a regulator RS79L which has an input also from a battery of any voltage ranging from 7 V to 35 V. These regulators can provide maximum current of 100 mA. The output voltage of RS79L is fixed at -5 V, while the voltage-adjustable regulator RS317L was set to output +5 V. This circuit also included two pairs of red and green LED's. The red LED indicates whether the power supply is "on" or "off": the green flashing LED is used in the load of the transistors T_3 and T_4, where for a positive output voltage the LED will flash when the output current exceeds 25 mA, thus indicating that a short-circuit has been detected. The same is true for the negative voltage output, except that the output current limitation is 10 mA. The common end of the

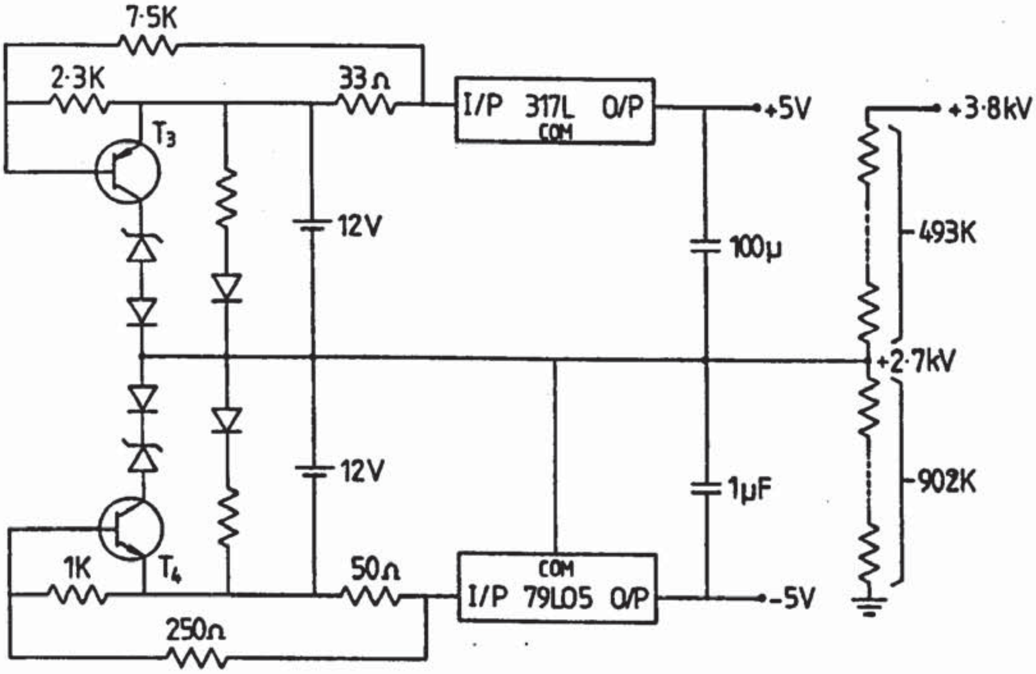

Fig. 4.24 The circuit diagram of the power supplies.

circuit is connected to the 2.7 kV point of the high voltage divider described below, so that all the circuits powered by the low-voltage power supply float above a voltage of 2.7 kV.

The high potential is provided by a high-voltage power supply unit (Brandenberg model 517), which has a maximum output voltage of 5 kV and a maximum output current of 5 mA at this voltage. Normally, a voltage of 3.8 kV is required to supply the collector of the transistors T_1 and T_2, while the voltage of the floating point, i.e. 2.7 kV is obtained by sub-dividing the 3.8 kV by a chain of resistors. To avoid exceeding the limitation of consumption power of the resistors it is inadvisable to use a high voltage of more than 3.8 kV.

4.3.3.g. The synchronously scanned storage oscilloscope

This is a very important requirement for the purpose of storing an undistored image on the oscilloscope screen and, provided that the functions of the oscillosope are fully used, it is a relatively straightforward procedure. Thus, it is achieved by providing the oscilloscope with a staircase waveform voltage signal to its y-input and a narrow pulse to its external trigger input. Then, setting-up the x-scan of a scope in its chopping mode, and adjusting the time needed to scan over the screen to be a little longer than that between two triggering pulses, the electron beam responds to a triggering pulse by starting its scan from the right hand extreme and continuing until the next pulse comes to restart it. On the other hand, a staircase voltage signal is applied to the y-input of the oscilloscope, it will respond to the triggering pulse by moving up one stair, i.e. as described in section 4.3.3.b. The combination of this staircase voltage and the scan voltage of the scope will together drive the electron beam to "write" a trace on the screen in a raster pattern in the same way as that illustrated in figure 4.20.

Therefore, to ensure that this electron beam scans schronously with that within the interfacing lens, a narrow positive pulse, taken from the output B_2 of the unijuntion transistor, is transmitted from the high-voltage unit to an input of op-amp 741 by the opto-isolator circuit shown in figure 4.22b. Its principle is same as that of figure 4.22a, except that now the LED is on the high-voltage end, whilst the transistor is on the low-voltage end. The op-amp 741 was again designed to be a follower with gain, but here it amplifies the input signal to 14 V which is high enough for later usage. This output is used directly both as an external trigger signal to the oscilloscope and fed into the input of 4040B in a ciruit arranged in a similar way as to that shown in the circuit of figure 4.19; i.e. except that the values of the resistors were changed to accord with the +15 V power supply.

4.3.3.h. The z-modulation of the storage oscilloscope

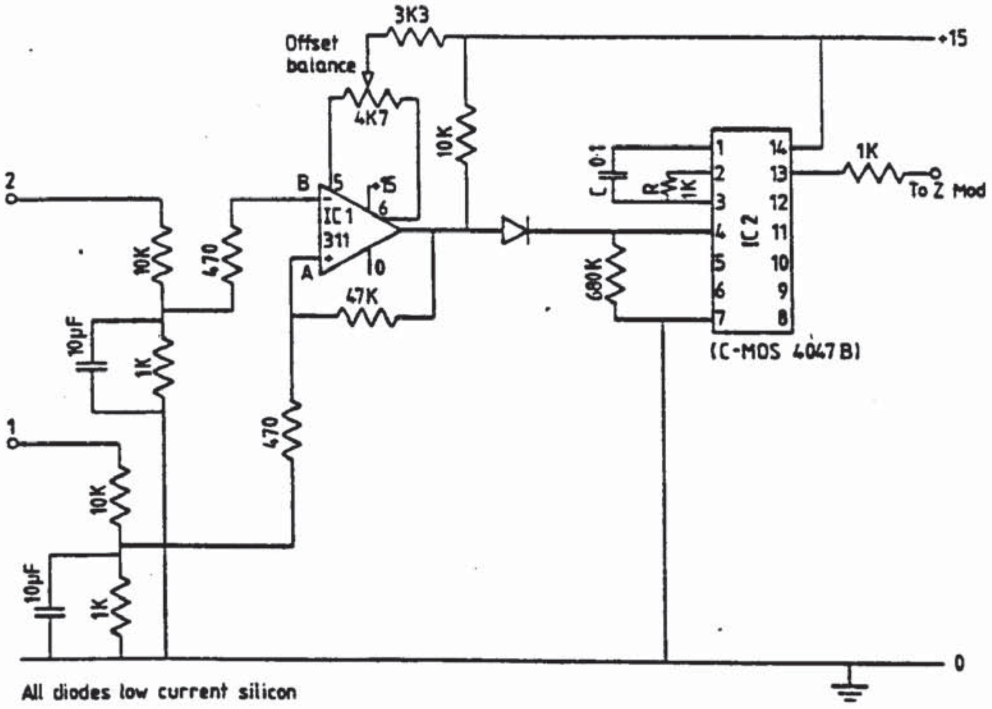

Fig. 4.25 The circuit diagram of the oscilloscope "bright up" and threshold detector.

In order to record a picture of an energy-selective electron image on the screen of the storage oscilloscope, the current from the electron multiplier is fed into the bright-up circuit shown in figure 4.25, originally designed by Bayliss [32]. It was so designed that under zero current conditions, the electron beam of the oscilloscope is biassed off. However, once the current reaches a threshold value, that is determined by the total emission current collected by the anode, it stimulates the generation of a series of voltage pulses of frequency of 1 MH_z, which are fed into the z-mode input connection of the oscilloscope, and give rise to a larger electron beam current and hence a "bright-up" of the 0.1 mm diameter spot on the display screen.

4.3.4. The operational procedure

(i) Recording an emission current pattern on the storage oscilloscope

The standard practical procedure was adopted for recording the typical data presented in the following chapter.

a. An emission site is located by the electrode scan system (see section 4.2.8).

b. The voltage of the interfacing lens is adjusted to give a sharp image on the phosphor screen.

c. The spectrometer facility is set up, and adjusted to give the best transmission, i.e. by maximising the reading on the rate meter at a given gain of the electron multiplier.

d. The visual image is centred over the aperture probe hole.

e. The ramp generator is set to operate at its maximum scan speed, i.e. corresponding to the scan duration of 10 ms, with scan voltage ranges of 2 V or 5 V.

f. The synchronously scanned oscilloscope is set up, and its brightness turned down so that the electron beam does not bright-up the screen when no electron current comes from the spectrometer.

g. A suitable number of scan lines are chosen and the deflecting voltage is adjusted to accommodate the size of an image.

h. The scan is initiated by pressing the "switch-on" buttom, i.e. by sending a pulse from the ground potential unit to the signal generator in the high potential unit.

(ii) Recording a picture of an energy-selected electron distribution

This is achieved by a very similar procedure to that described above, except that the analyser is tuned to a selected energy or a range of energies, as measured with respect to the cathode Fermi level. It will be recalled that in the present instrument, energy can be equated with scan voltage. Since the existing ramp generator can provide functions for both tuning the start-voltages, ranging from 3 V to 9 V, and changing the scan-voltage among 1 V, 2 V, 5 V and 10 V, the system can operate in two modes; i.e. either using a narrow energy window mode (determined by the resolution of the analyser, i.e. 25 meV), when a scan voltage is fixed to certain value, or a variable wide energy window, when the analyser is scanned in a certain range of voltage. This latter mode is possible only when the frequency of the energy scan is much higher than that of the deflecting voltage signal; for example, the two frequencies of 100 Hz for the energy scan and 0.33 Hz for the electron beam scan were often used in the present experimental programme. It should be noted that, since the FWHM of the emitted electron energy distribution is normally less than 0.5 eV, a future improvment to the system would be to add the capability of using an energy window of less than 0.5 eV.

CHAPTER FIVE

EXPERIMENTAL FINDINGS

5.1. General experimental procedures

The standard specimen used in this experimental programme was in the form of a thick disc having a diameter of 14 mm, a thickness of 5 mm and a 1 mm radiassed edge to minimise edge effects resulting from geometrical field enhancement [104]. The specimen preparation procedure was initiated by metallurgically grinding its active surface until there were no cracks or scratches visible to the naked eye. It was then subjected to a two-stage diamond polishing process, in which the smooth surface, the radiussed edge and its cylindrical side were successively polished to a 6 μm and 1 μm finish. Subsequently, it was immersed in methanol and ultrasonically cleaned for ~15 minutes, and then washed with distilled water. Particular care was taken to prevent it from being contaminated during the course of the above sequence, and a final rinse was given to the surface in order to remove any particles (e.g. dust) that may have become attached to the surface while handling the specimen. It is also important to note that the anode surface was cleaned in a similar way from time to time during the course of this programme.

The vacuum chamber could be routinely pumped down to a pressure of ~10^{-9} mbar after changing a specimen. However, to obtain the best pressure of ~ 5×10^{-10} mbar, it had to be baked at ~220° C overnight, and subsequently trapped with liquid nitrogen.

The in-situ parallel alignment of the anode and cathode surface could be quickly and accurately achieved by a simple procedure fully described elsewhere [32]. This was based on the assumption that the cathode surface was parallel to the back surface of the cylindrical specimen holder. This latter reference surface and that of the molybdenum anode were highly polished and had a comparable reflectance to a silver mirror. Having set a gap to ~1 mm by the Z-micrometer, a careful adjustment to the X and Y direction of the specimen holder could lead to completion of an undistorted image, in between two "mirrors", of a eye and thus the alignment was obtained.

The external electrical circuitry used for recording emission is shown in figure 5.1. Thus, the anode is connected to a 15 kV power supply (Brandenburg, Model No.2707), which includes a picoammeter monitoring facility to measure the anode current, while another picoammeter is used to monitor the cathode current. To obtain emission, the anode voltage was raised slowly in steps of 200 V, leaving a 5 minute interval between sequential steps. This procedure was adopted to ensure that in this interval, any delayed switch-on effects or microparticle activities could be detected at the lowest anode voltage and "flash-over" events could thus be avoided. Thus it was routinely possible to observe the unstable "switch on" of a site and subsequently record a stable and reversible I-V characteristic.

Having thus established a stable prebreakdown electron emission current, a searching procedure is initiated [32] to precisely locate the coordinates of the emitting sites. This involves scanning the cathode in a spiral pattern in front of the anode probe hole, such that when a site passes in front of the hole, electrons are detected by the spectrometer and the signal is used to bright-up a synchronously scanned storage oscilloscope to give a map of the site distribution on the surface of the cathode; i.e. such as shown in figure 5.2. Any chosen site can then be relocated on-axis, i.e. opposite the anode hole, and the interface lens focussed to form a visible image of the emission on the phosphor screen (see figure 4.6), which can be externally photographed through a window in the vacuum chamber and a slot in the lens electrode. Microadjustment of the cathode position and the lens voltage then allows any desired part of the emission pattern to be positioned over the probe hole for electron

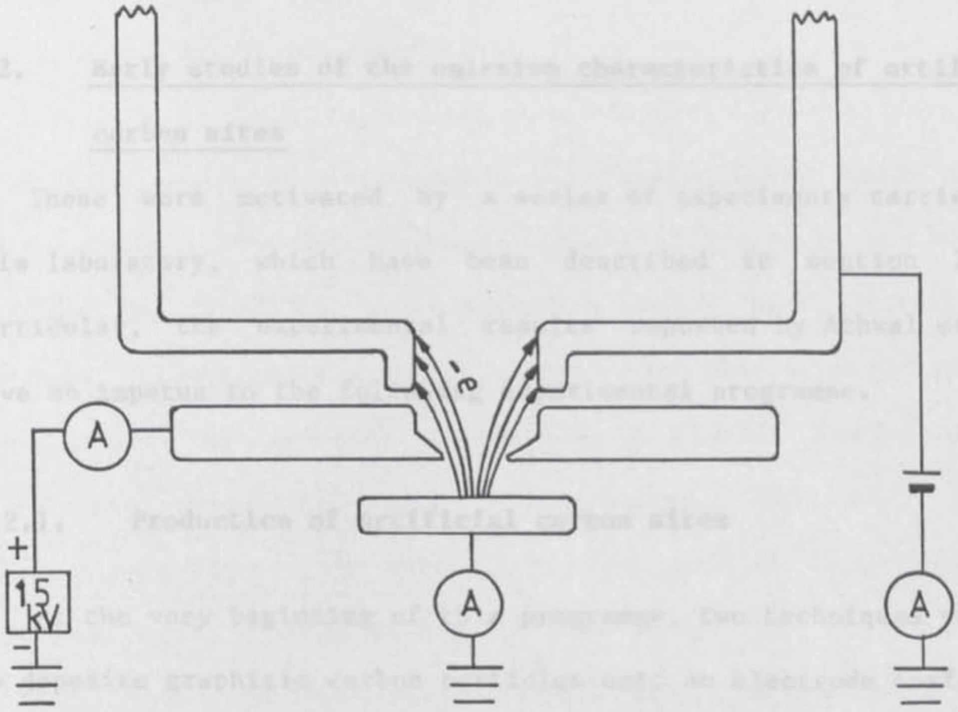

Fig. 5.1 The electrical connections used to obtain emission.

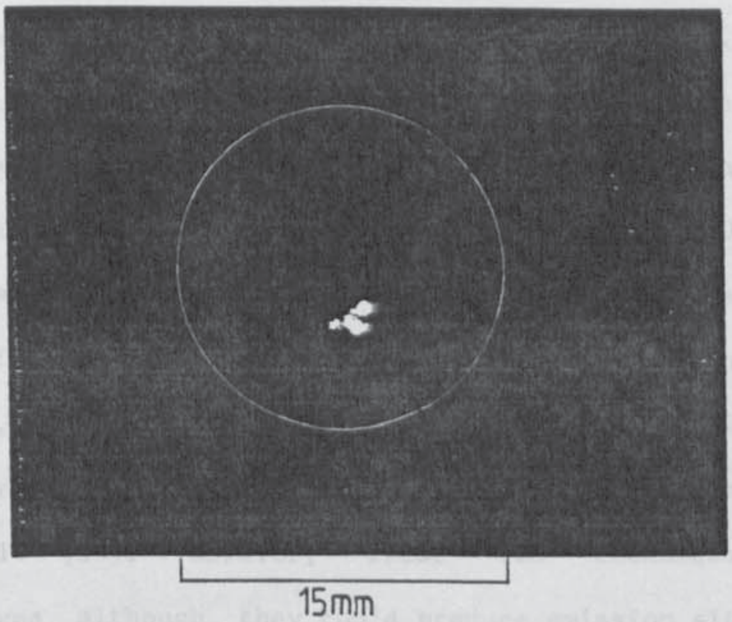

Fig. 5.2 A high-resolution map of an emission-site distribution.

energy analysis.

5.2. Early studies of the emission characteristics of artificial carbon sites

These were motivated by a series of experiments carried out in this laboratory, which have been described in section 2.4. In particular, the experimental results reported by Athwal et al [33] gave an impetus to the following experimental programme.

5.2.1. Production of artificial carbon sites

At the very beginning of this programme, two techniques were used to deposite graphitic carbon particles onto an electrode surface; i.e. those reported by Athwal et al [33]. In the first, a micromanipulator was employed to gently lower a finely sharpened pencil lead onto a known position on the surface of a planar electrode. A gentle "touch" of the pencil tip with the surface of the electrode would then produce a faintly visible carbon spot of typical diameter of ~ 0.2 mm. In the second, which used colloidal graphite (Aquadag) that was diluted with methanol as the source of carbon, a syringe with a fine needle was able to inject a drop of Aquadag with a diameter of ~0.5 mm onto the electrode surface. The drop, after drying, typically left a visible deposit of even smaller dimensions. Under a scanning electron microscope, such deposits were found to have a random distribution of carbon particles of different sizes and orientations, as shown in figure 2.14 [33]. However, these two techniques both had disadvantages although they could produce emission sites. The first suffered from a lack of mechanical control of the "touch", and frequently results in scratching to the electrode surface. The second was believed to produce somewhat more contaminated sites due to both the purity of Aquadag itself and the handling processes. Consequently, the sites produced by using these two techniques were unsuitable for detailed analysis.

Accordingly, these techniques were replaced for later experiments on artificial carbon sites by a new and simple one, which differed from the above techniques, in that a single carbon particle could be routinely deposited to any desired position on the surface of an electrode. Firstly pure graphitic carbon particles were spreaded on a glass plate so that a number of particles of similar dimension could be selected from them under a microscope. Then, these selected particles were transported onto any desired position on the electrode surface by using a tungsten tip that was wetted with methanol so that a particle would adhere to it. It is also important that both the tip and the plate were ultrasonically cleaned for ~15 minutes. The practical experience gained from the experiments with carbon sites produced by using this method indicates that it can produce a high percentage of analysable emission sites, and might minimise any possible contamination under the present laboratory conditions. This is supported by the fact that on every occasion that the technique has been used, at least one of these sites switched on.

5.2.2 "Switch on" effect of artificial carbon sites

Having thus succeeded in depositing a "pure" and single particle on an electrode surface, the experimental procedures described in previous section were followed; i.e. the gap field was carefully increased in increments until a stage when some sites were "switched on". Figure 5.3 illustrates a typical single-site "switch on" characteristic. From this it is seen that when a site is first exposed to an applied electrical field, its current is not detectable

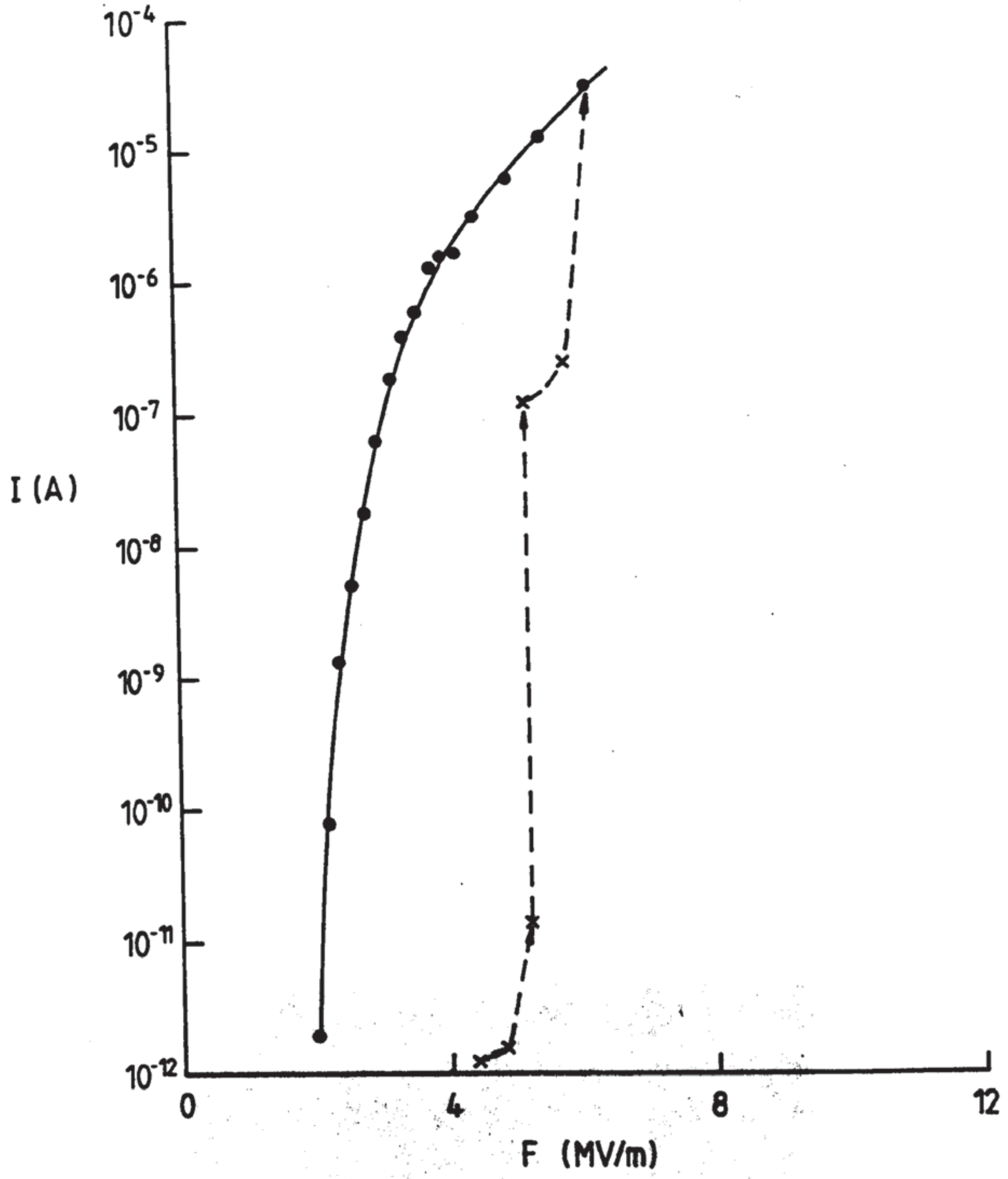

Fig. 5.3 The "switch-on" characteristic of a typical site, accompanied by its reversable I-V characeristic.

---

above a level of 10^{-12} A. However, when some threshold field is reached, the current exhibits a very unstable but gradually rising stage, which is followed by a spontaneous switch-on to a current of 10^{-5}A at which point the current tends to increase rapidly so that the field has to be quickly turned down if a flash-over is to be avoided. Even so, the current remains at a level of 10^{-6} A, at a voltage of 2 or 3 kV less than the previous value. In many cases, an I-V characteristic can then change to a reversible curve, which represents a stable state, as is also shown in figure 5.3. Occasionally, however, a site needs to be re-switched on in order to obtain a stable I-V characteristic, particularly when the pressure of the vacuum chamber is above 5×10^{-9} mbar. Furthermore, it must be emphasised that the number of sites that are switched on at any one time is unlikely to depend only on their dimensions, i.e. the associated field enhancement. Thus, as an example, figure 5.4 shows a map of "simultaneously " switched-on artificial carbon sites on an electrode surface. It was also found that the switch-on of some artificial carbon sites having higher β-values could be switched on after several cycles of measurements on the other sites.

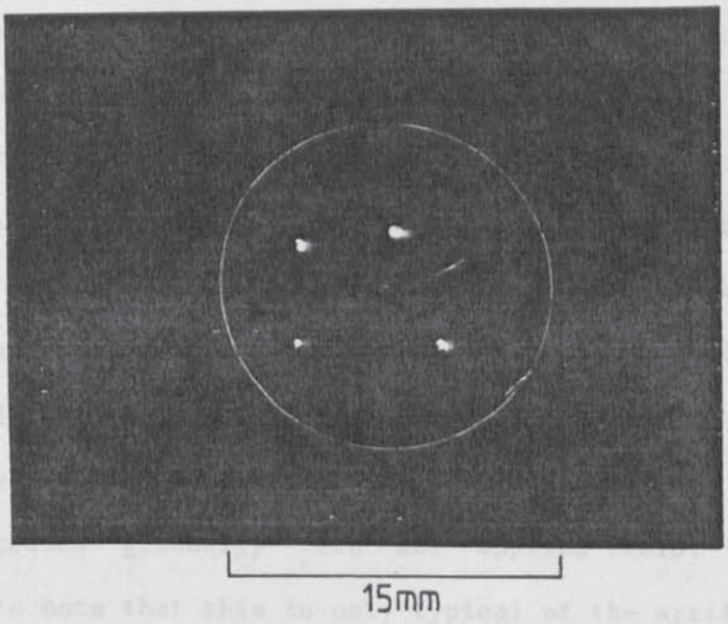

Fig. 5.4 A map of the distribution of four "simutaneously" switched-on sites.

5.2.3 Electron energy spectra and emission images of artificial carbon sites

This section presents a series of selected electron energy spectra and emission images of the artificial carbon sites formed on a range of electrodes of different materials, and from this data it will be possible to illustrate their common characteristics. Thus, referring to figure 5.5, both spectra and emission images are presented in parallel so that the inherent properties revealed by these two types of important measurement can be readily perceived. Also, in order to illustrate how the spectrum varies with field, a coherent sequence of spectra recorded from a segment is presented in figure 5.6. Thus, firstly, all spectra are single peak: double-peak or multi-peak spectra, such as reported by Athwal et al [33] were found to result from the overlap of two or more unstable segments; i.e., the phenomenon is similar to that explained elsewhere [31]. In fact, overlap was caused by an operational limitation of the interfacing lens which was subsequently eliminated (see section 4.2.5.). Thus, it can be concluded that these double or multi-peak spectra are not an intrinsic characteristic of artificial carbon sites. Secondly, all the spectra of emitted electrons detected by our facility with its present sensitivity are shifted by at least 0.2 eV below the Fermi level of the cathode electrode. This spectral shift S is field-dependent, as with the natural sites [9,24,25], and is illustrated in figure 5.7 which was constructed from the complete spectral sequence of figure 5.6. From this it can be seen how the shift increases gradually with the applied field. However, it is important to note that this is only typical of the artificial sites on an ambiently oxidised electrode surface. The type of rapid increase of spectral shift with field, such as shown in figure 5.5.2, often occured with sites on intentionaly oxidized electrode surfaces,

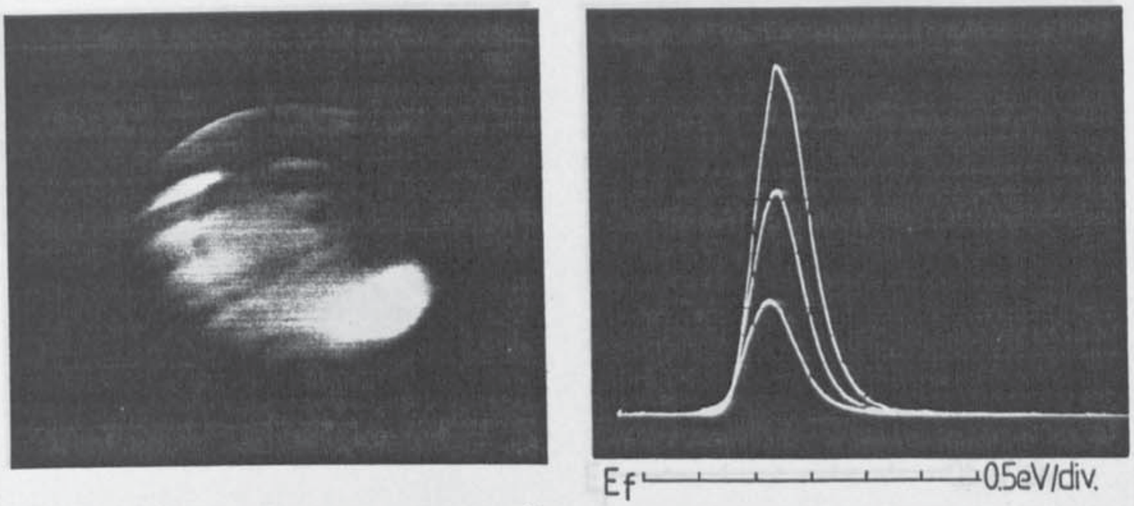

Cu

(a)
Emission image

(b)
Coherent set of spectra for:
F in range of 6.6 to 7 MV/m.
(gap spacing = 0.5 mm).

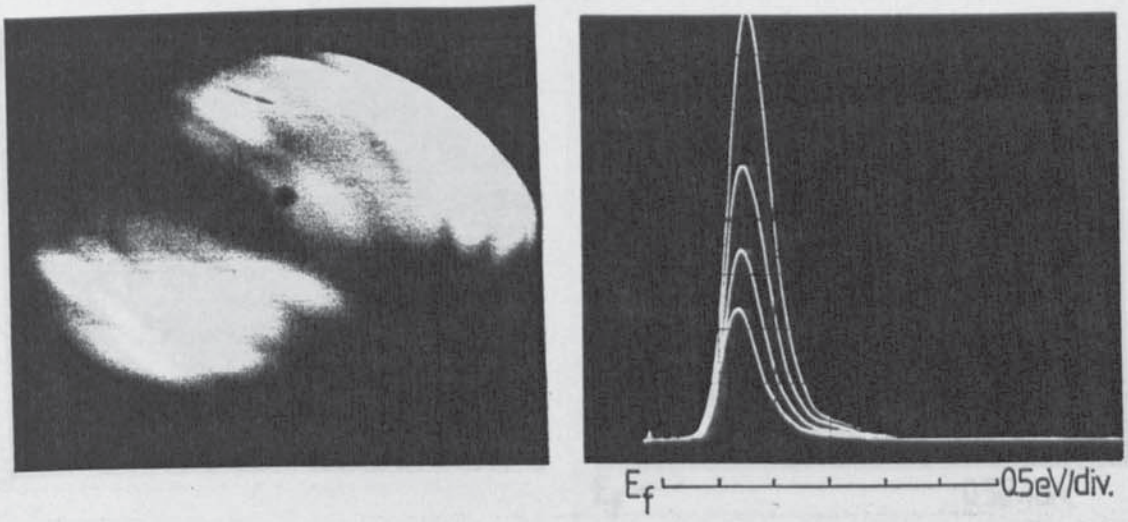

Mo

(a)
Emission image

(b)
Coherent set of spectra for:
F in range of 7.8 to 8.4 MV/m.
(gap spacing = 0.5 mm).

(NB. The area under the spectral curve and, hence, the peak height increases with field (in 0.2 MV/m increment). Y axis, current per unit energy, arbitrary units. Energy decreasing left to right. E_f = Fermi level position.)

Fig. 5.5.1 The spectra and emission image of the graphitic carbon site artificially deppsited on the surfaces of electrodes of different materials.

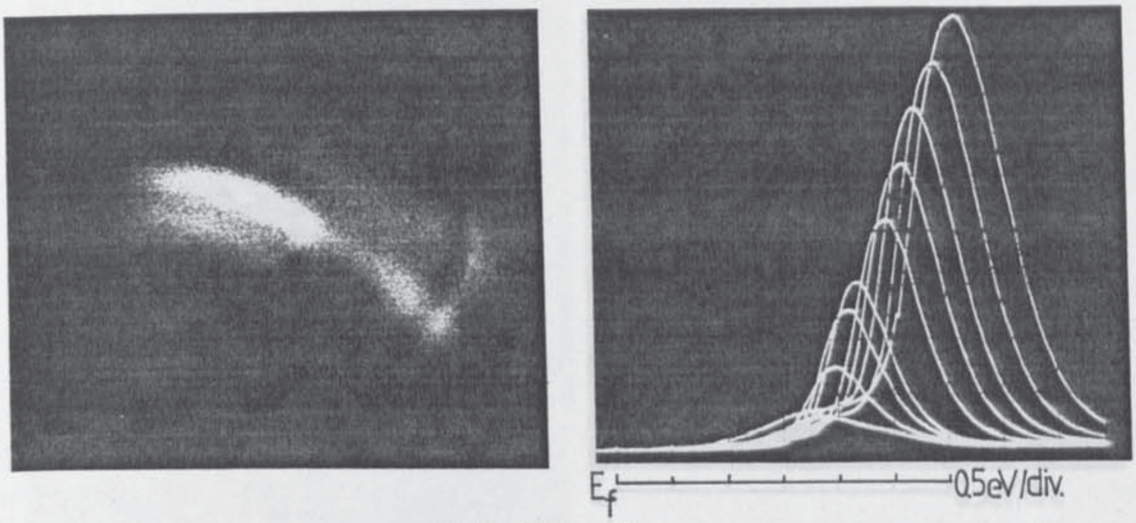

Al (oxidised)

(a)
Emission image

(b)
Coherent set of spectra for:
F in range of 7.2 to 8.8 MV/m.
(gap spacing = 0.5 mm).

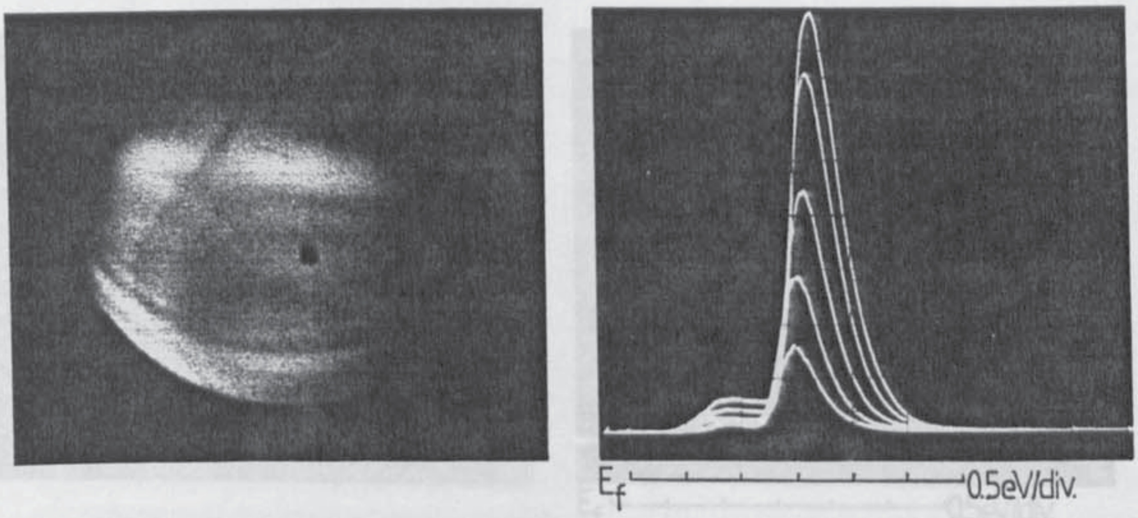

Cu (oxidised)

(a)
Emission image

(b)
Coherent set of spectra for:
F in range of 7 to 7.8 MV/m.
(gap spacing = 0.5 mm).

(NB. The area under the spectral curve and, hence, the peak height increases with field (in 0.2 MV/m increment). Y axis, current per unit energy, arbitrary units. Energy decreasing left to right. E_f = Fermi level position.)

Fig. 5.5.2 The spectra and emission image of the graphitic carbon site artificially deposited on the surfaces of electrodes of different materials.

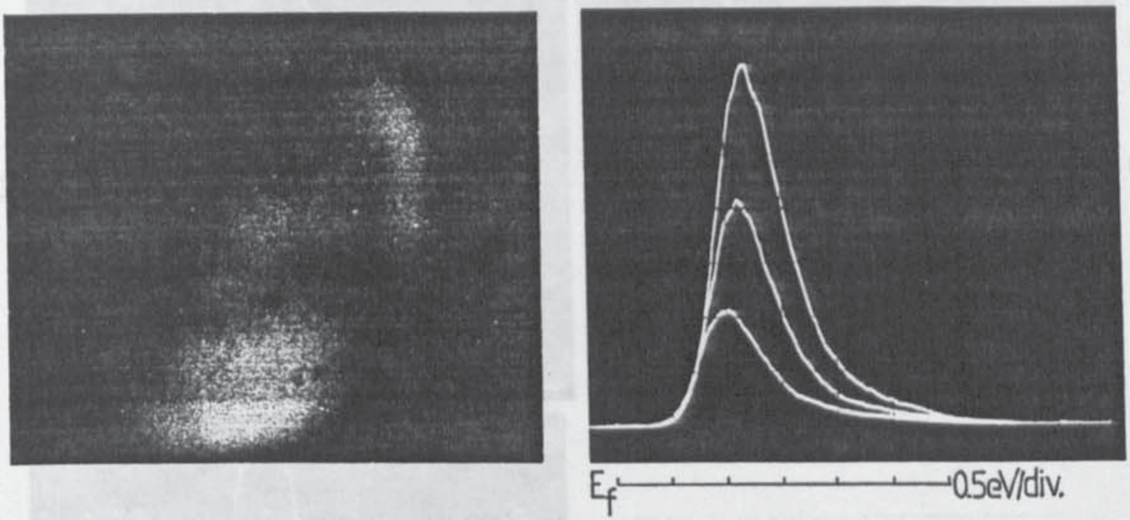

St. St.

(a)
Emission image

(b)
Coherent set of spectra for:
F in range of 6 to 6.4 MV/m.
(gap spacing = 0.5 mm).

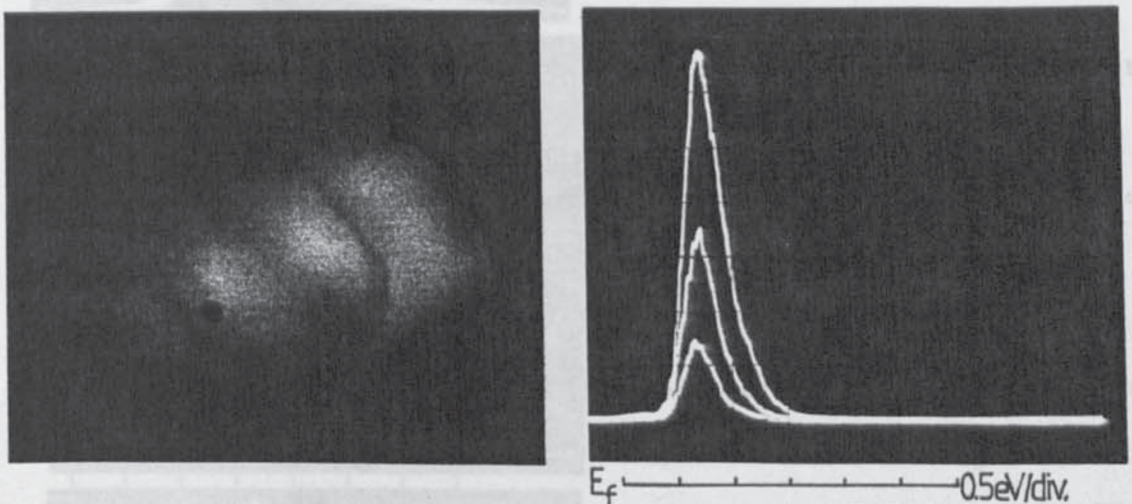

Cu

(a)
Emission image

(b)
Coherent set of spectra for:
F in range of 8.0 to 8.4 MV/m.
(gap spacing = 0.5 mm).

(NB. The area under the spectral curve and, hence, the peak height increases with field (in 0.2 MV/m increment). Y axis, current per unit energy, arbitrary units. Energy decreasing left to right. E_f = Fermi level position.)

Fig. 5.5.3 The spectra and emission image of the graphitic carbon site artificially deposited on the surfaces of electrodes of different materials.

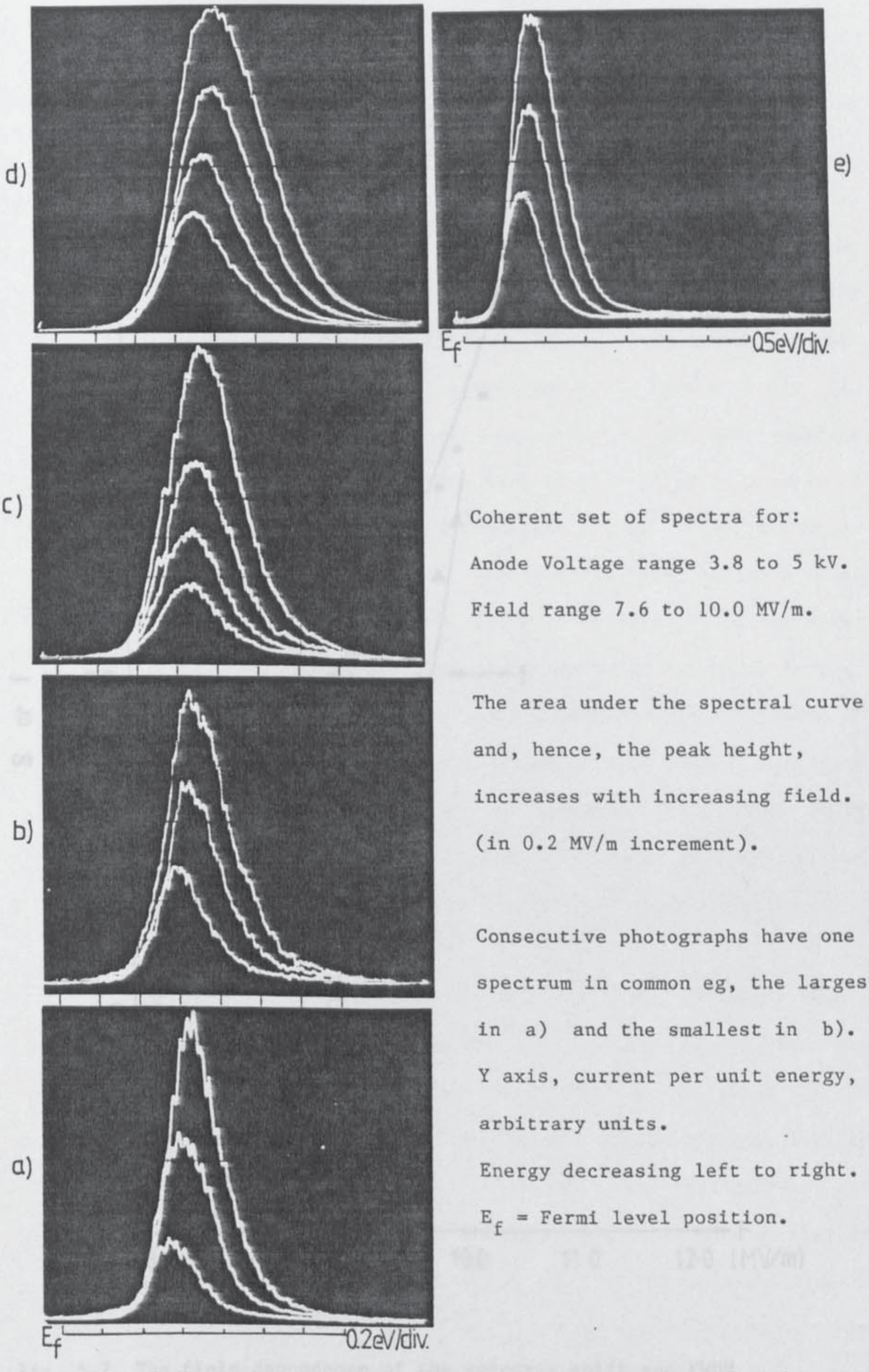

Coherent set of spectra for:

Anode Voltage range 3.8 to 5 kV.

Field range 7.6 to 10.0 MV/m.

The area under the spectral curve and, hence, the peak height, increases with increasing field. (in 0.2 MV/m increment).

Consecutive photographs have one spectrum in common eg, the largest in a) and the smallest in b).

Y axis, current per unit energy, arbitrary units.

Energy decreasing left to right.

E_f = Fermi level position.

Fig. 5.6 A sequence of spectra recorded from an artificial graphitic carbon site (site 1).

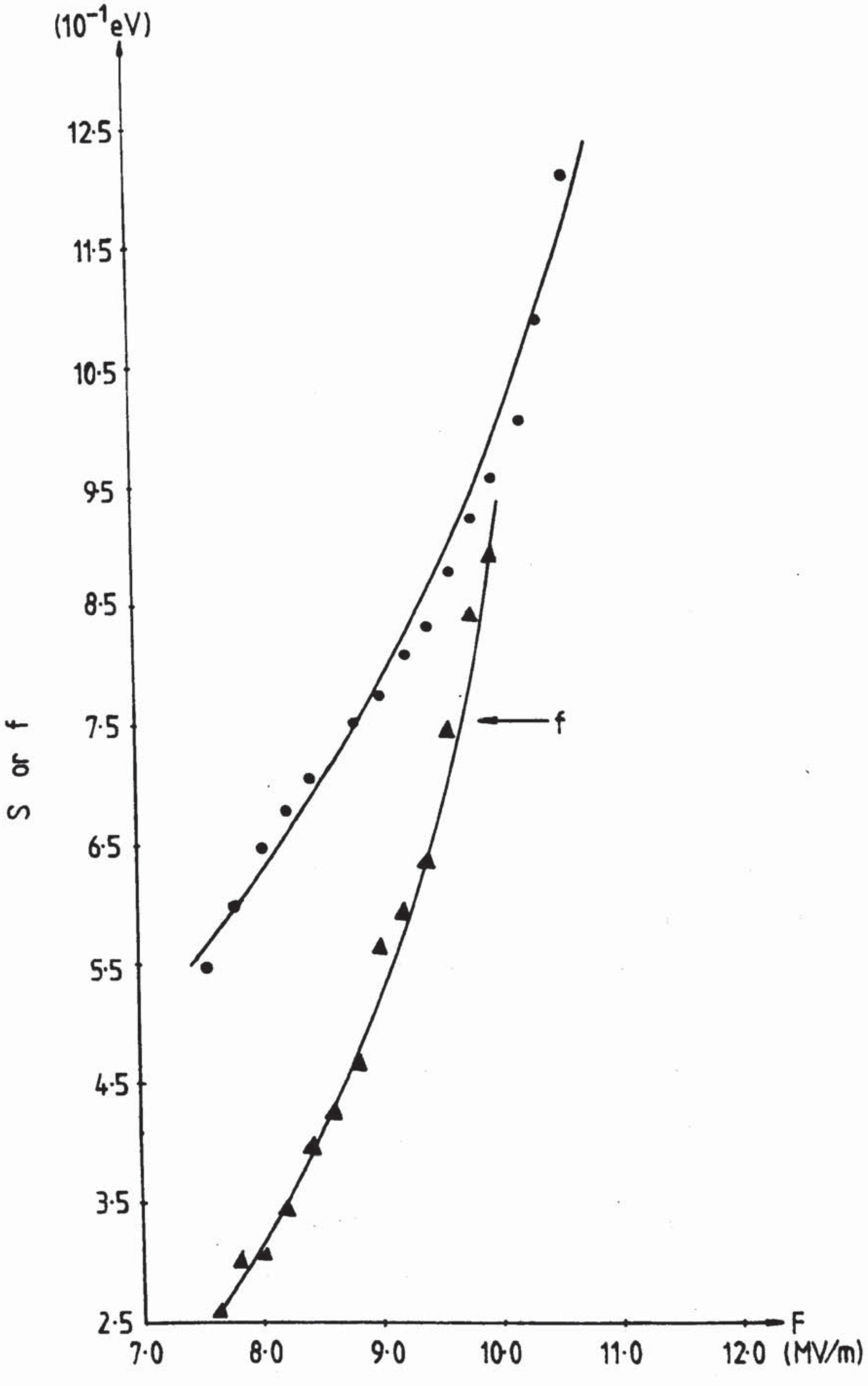

Fig. 5.7 The field dependence of the spectral shift and FWHM of the artificial carbon site.(site 1).

but only rarely with sites on ambiently oxidized surfaces. Thirdly, the half-width (FWHM) of the spectra is generally more than 0.3 eV and also field-dependent, as also illustrated in figure 5.7.

The electron emission images, however, generally differ from those recorded by Bayliss [32], although two of the eight images he presented in his thesis are somewhat similar. As defined previously [105], such images are classified as Type 2 (accordingly the site associated with type 2 image will be referred to as Type 2 site). In contrast with type 1 images, these images consist of arc-like segments rather than diffuse sub-spots, and were considered to be capable of providing some very important information about the mechanism operating at this kind of site. Consequently, they became a major subject for investigation in the later programme of this work. Although it is premature to say more about the origin of these images, a qualitative comparison can be made with those observed by Simmoms et al from purpose-fabricated MIM hot electron devices [8,88], described in section 3.3.4, from which it can be concluded that they share obvious geometrical resemblances; i.e. every image includes several segments which look very much like new-moons and subtend angles of $< 180^{o}$.

As illustrated in figure 5.5, there are many instances when a image consists of several segments that appear to be randomly orientated. However, one occasionally obtains an image of an artificial carbon site that consists of only a single segment, i.e. as shown in figure 5.8. Such sites are very convenient for analysis, and from the sequence of images shown in figure 5.8, it is evident that as the field is gradually raised, the outer edges of the segment remains relatively well-defined as its overall size increases. The corresponding series of electron spectra associated with these five

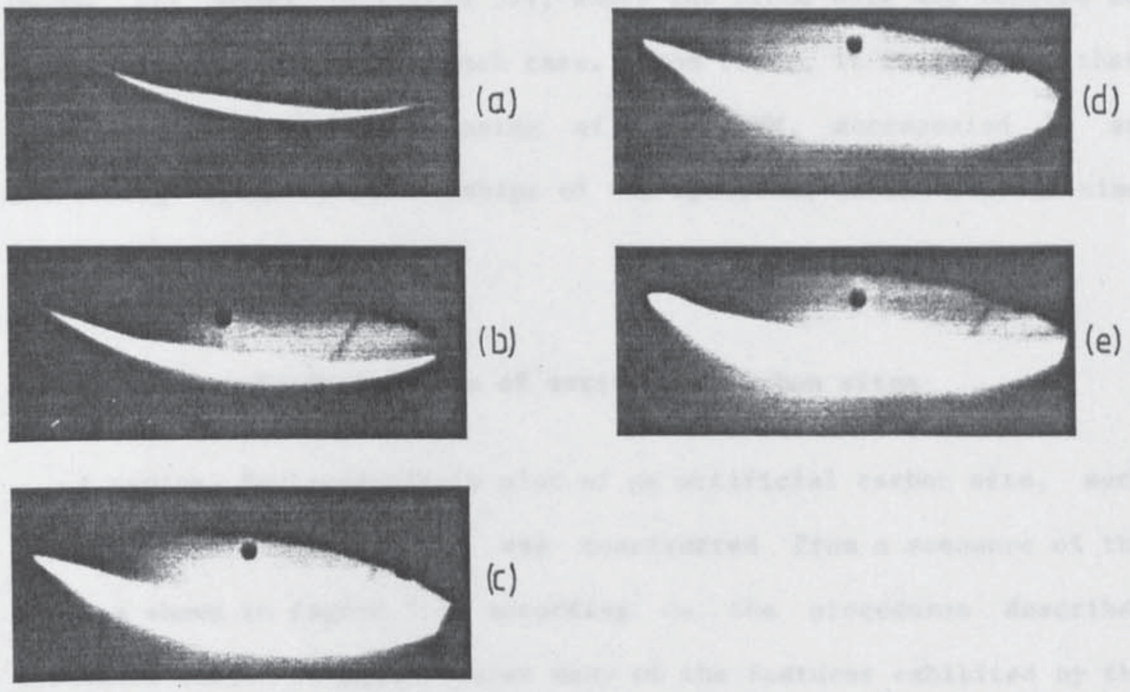

Fig. 5.8 A single-segment image of an artificial carbon site recorded under increasing field conditions.(site 2).

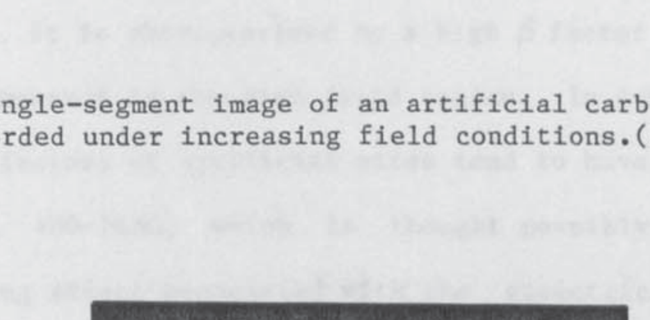

Fig. 5.9 The superimposed electron spectra recorded from the emission images shown in the sequence of figure 5.8.(site 2).

images are shown in figure 5.9, where the probe hole was located at the centre of the image in each case. From these, it is apparent that there is a gradual broadening of the FWHM, accompanied by an increasing symmetry in the shape of the spectrum, as the overall size of the image increases.

5.2.4 Fowler-Nordheim plots of artificial carbon sites

A typical Fowler-Nordheim plot of an artificial carbon site, such as shown in figure 5.10, was constructed from a sequence of the spectra shown in figure 5.6 according to the procedures described elsewhere [32]. It again shares many of the features exhibited by the natural sites previously studies by Latham and co-workers [9,24,25]. In particular, it is characterised by a high β factor and a tendency to curve downwards in the high field region. In contrast to natural sites, the β factors of artificial sites tend to have higher values, ranging from 400-1600, which is thought possibly to result from a field enhancing effect associated with the geometrical configuration of a flake-like particle sitting on an electrode surface [33]: however, it is probable that this is not a complete explanation. In addition, it is frequently found that the high-field kink in the F.N. characteristic is more pronounced than with natural sites [33]; in such cases, the F.N. plot has two distinct linear regions, characterised by different β values. To give an idea of the F.N. characteristics found with artificial carbon sites, Table 5.1 summaries the values of the β factor, emission area and regression factor, calculated from F.N. plots of 7 sites. The fact that the regression factors deviate from 1 is believed to be partly due to the instabilities of a site, but mainly as a consequence of the F.N. points in the high-field region breaking away from the straight line

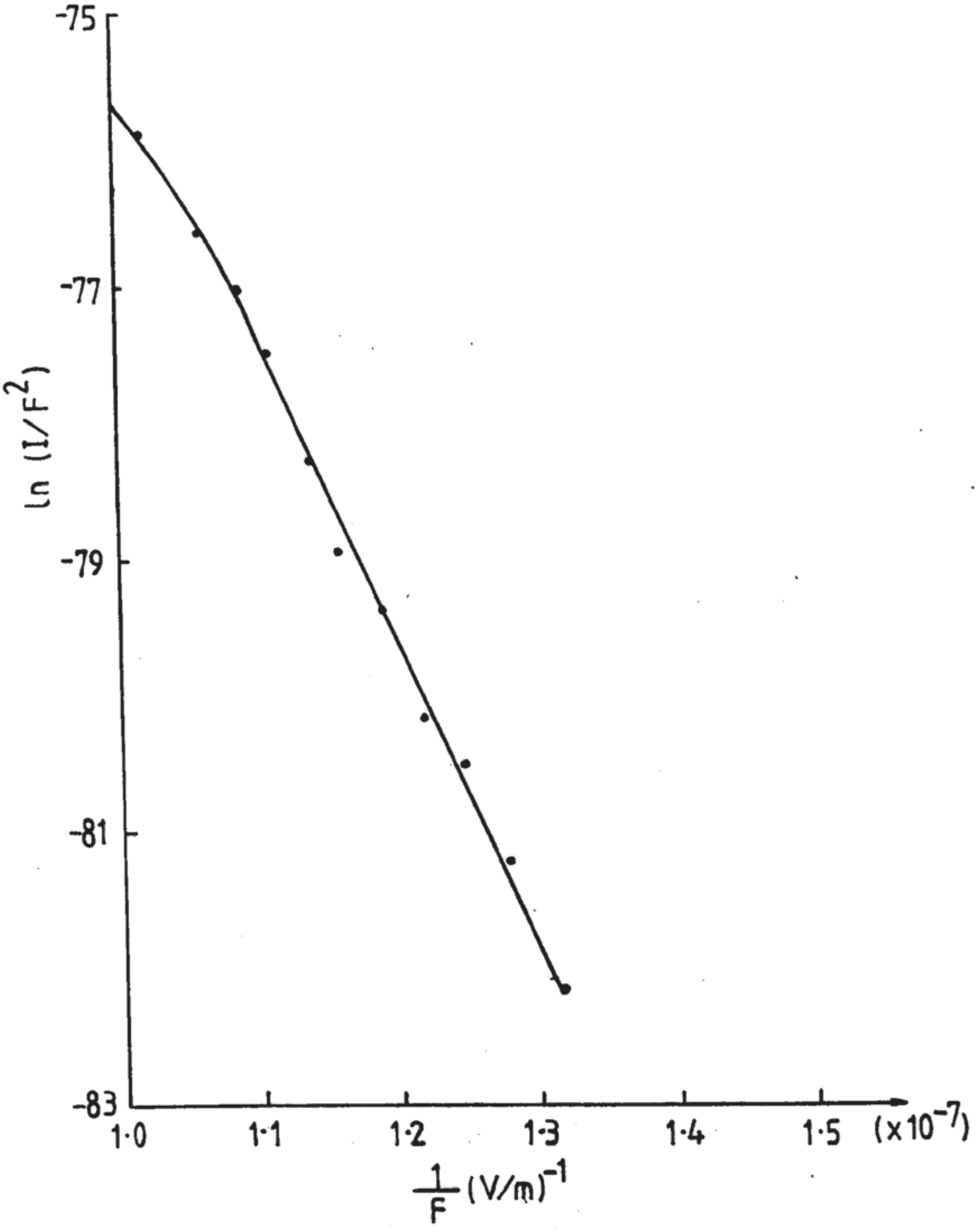

Fig. 5.10 The F.N. plot of the artificial carbon site.

Table 5.1

materials	β	A (m^2)	|R|
Cu	1211	1.921×10^{-16}	0.9322
Cu	1321	2.010×10^{-17}	0.9213
Al	1165	1.798×10^{-16}	0.9555
Cu	1128	4.132×10^{-18}	0.8967
Cu	690	2.050×10^{-16}	0.9827
Cu	562	2.573×10^{-16}	0.9872
Cu	1223	2.052×10^{-17}	0.9788

that characterises the low field range.

5.3. An investigation into natural sites on the surface of broad-area electrodes

Having made detailed observations of the characteristics of the artificial carbon sites, the direction of the study was switched to answer the important question of whether or not similar phenomena occured with natural sites. In fact, from a series of measurements on a range of specimens of different materials such as Mo, Al, stainless steel and particularly Cu, it was found that at least 25 - 30% of natural sites exhibited emission image characteristics similar to those observed with artificial carbon sites. In addition, this detailed study of emission sites on a range of mechanically and chemically polished cathode materials showed that their general characteristics were not significantly influenced by the choice of electrode material or surface processing. Accordingly, the properties to be described in the following sections are to be seen as typical of a process that could occur on any electrode material.

5.3.1. Emission image characteristics

Referring to figure 5.11, which presents three typical emission images, figure 5.11a is a typical emission image of a natural site on a bulk carbon specimen. This image was recorded at the relatively high gap-field of 18.4 MV/m, which was necessary for this particular site in order to draw sufficient current to give a visible image on the phosphor screen. Although its resolution is consequently poor, it can nevertheless be seen that the image consists of a group of "arc-like" segments. Figure 5.11b is a typical emission image recorded from a natural site on the surface of a copper electrode. Most of the

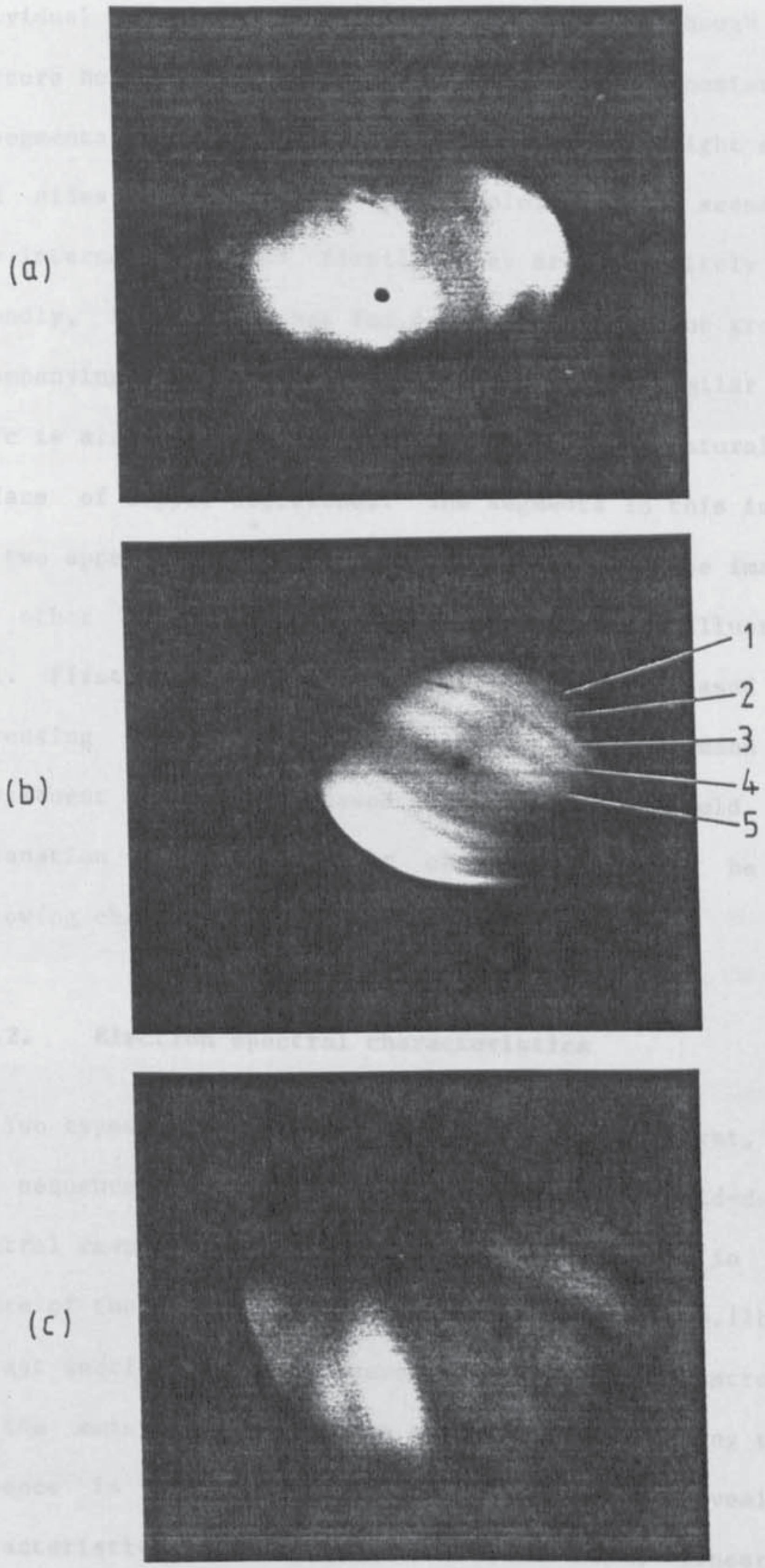

Fig. 5.11 Examples of electron spectra and emission images of the second type of natural site.

individual segments are clearly resolved although those below the aperture hole overlap. Furthermore, the image consists of two groups of segments, situated with respect to the upper right and lower left hand sides of the aperture probe hole. It also seems that they have some internal relation: firstly, they are oppositely oriented, and secondly, it seems that for each segment in one group, there is an accompanying segment in the other group with a similar radius. Figure 5.11c is also a typical image recorded from a natural site on the surface of copper electrodes. The segments in this image, apart from the two upper ones, are orientated randomly. These images also share two other important properties that are not illustrated in figure 5.11. Firstly, the overall size of an image increased gradually with increasing applied field, and secondly, the mean radii of their constituent segments increased with the applied field. The physical explanation of these latter observations will be considered in a following chapter.

5.3.2. Electron spectral characteristics

Two types of measurement are reported. The first, represented by the sequence of figure 5.12, measures the field-dependence of the spectral response from a fixed point in the image; in this case the centre of the inner segment, labelled 5 on figure 5.11b. As mentioned in last section, such a sequence can be used to construct an F.N. plot of the emission site. Thus the plot corresponding to this spectral sequence is presented in figure 5.13, and reveals the typical characteristic with a low-field (<12 MV/m) linear region with a field-enhancement factor of $200 < \beta < 1000$, and a non-linear high-field region. An equal, if not more important, feature of the evidence of figure 5.12, is that it reveals firstly how the position

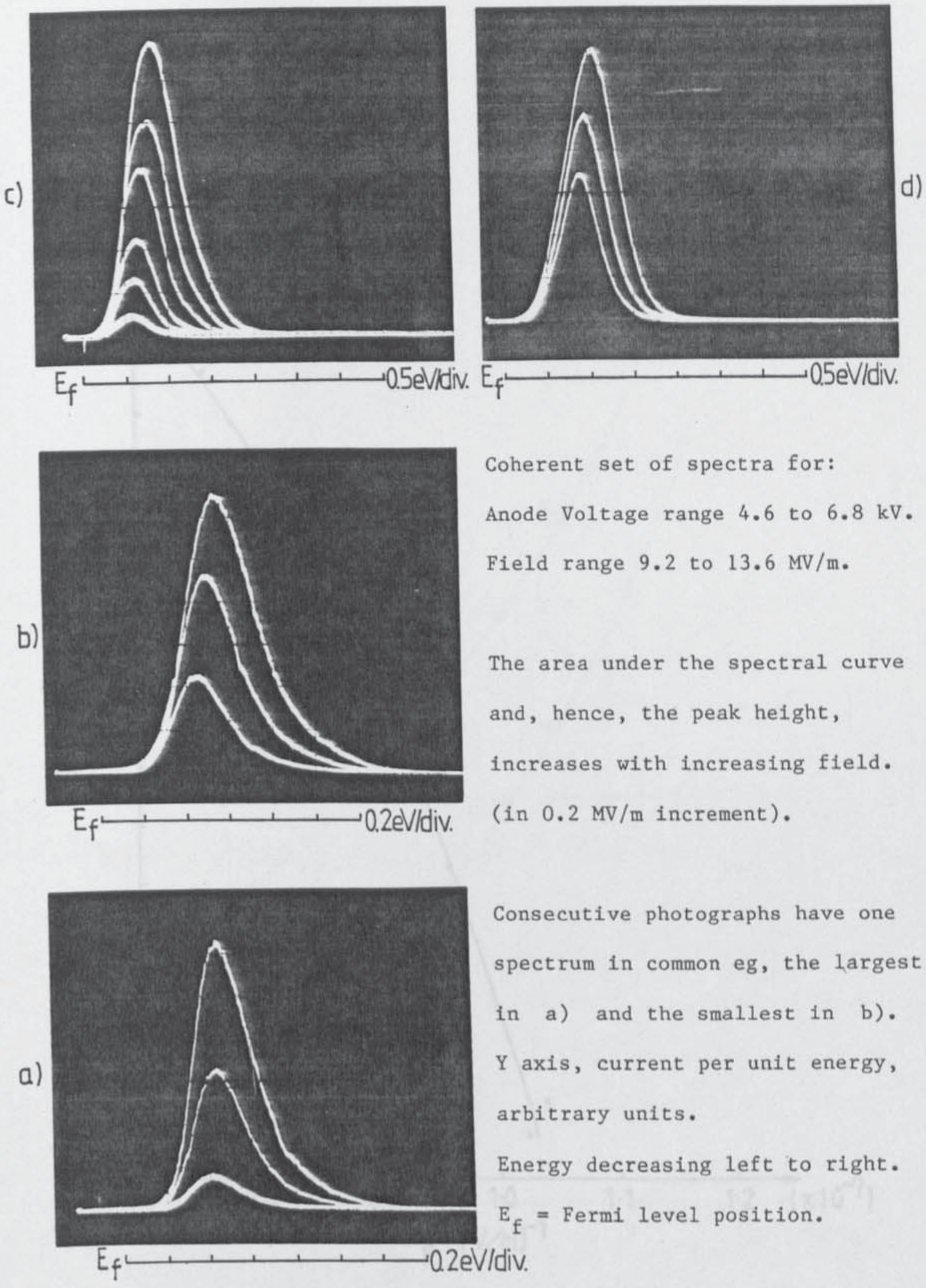

Coherent set of spectra for:
Anode Voltage range 4.6 to 6.8 kV.
Field range 9.2 to 13.6 MV/m.

The area under the spectral curve and, hence, the peak height, increases with increasing field. (in 0.2 MV/m increment).

Consecutive photographs have one spectrum in common eg, the largest in a) and the smallest in b).
Y axis, current per unit energy, arbitrary units.
Energy decreasing left to right.
E_f = Fermi level position.

Fig. 5.12 A sequence of spectra recorded from segment 5 of figure 5.11 b (site 3).

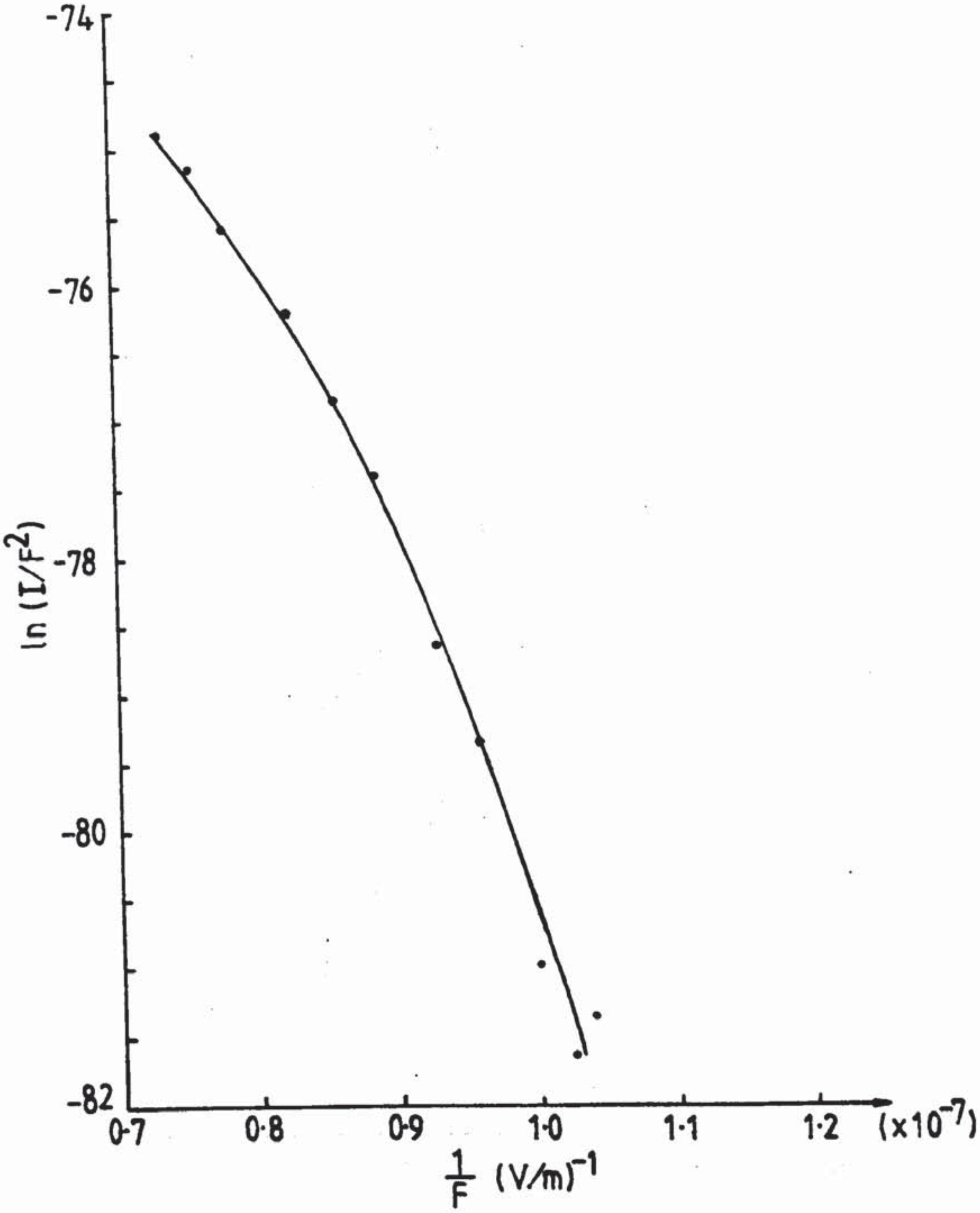

Fig. 5.13 **The F.N. plot of the emission from segment 5 of figure 5.11 b.(site 3).**

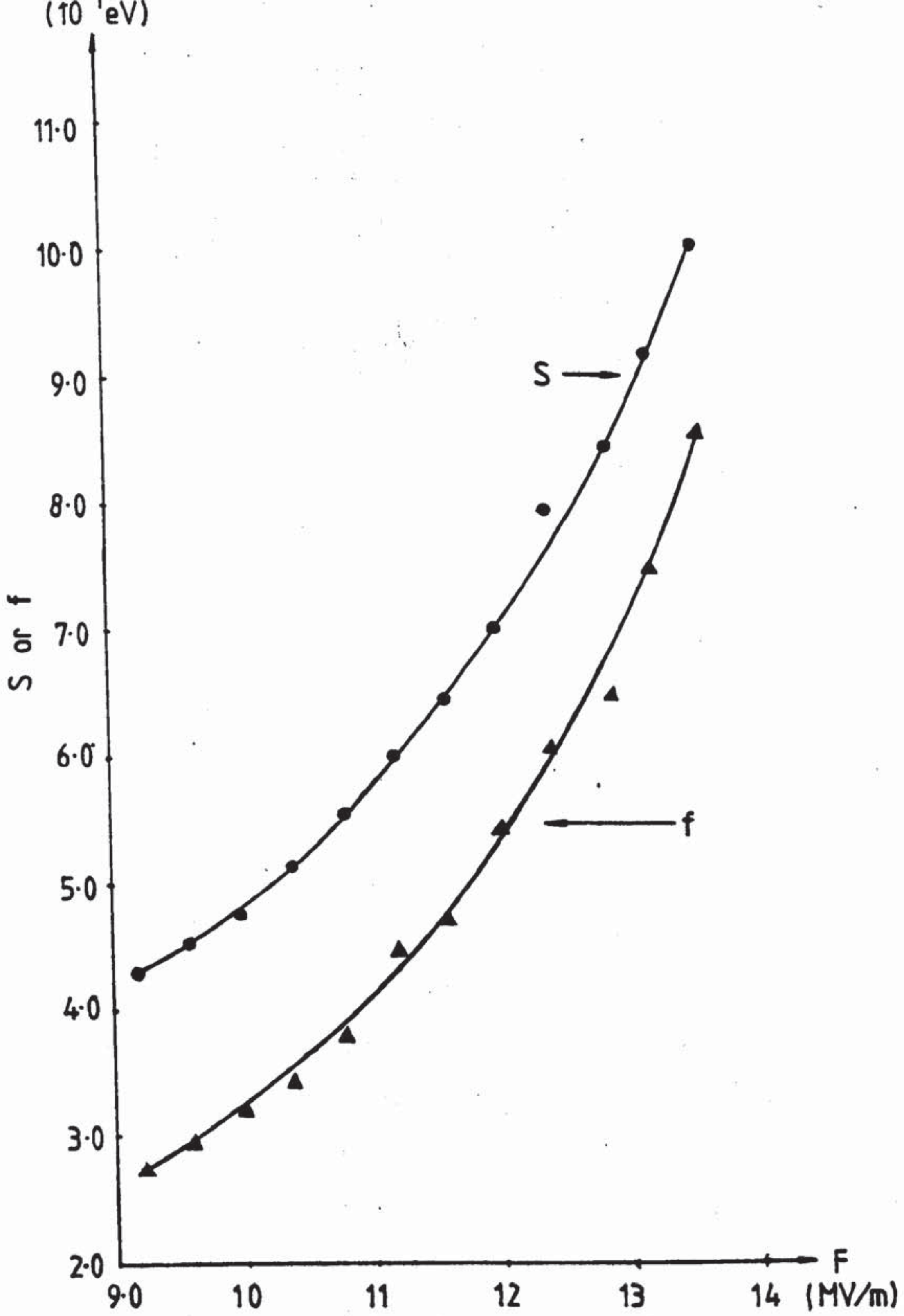

Fig. 5.14 The field-dependence of the spectral shift and FWHM buit up from a sequence of spectra shown in figure 5.1 .(site 3).

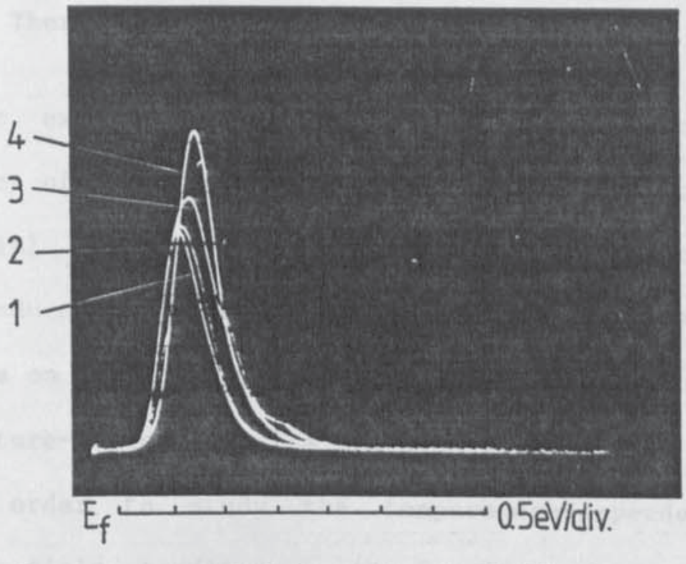

Fig. 5.15 Spectra recorded from the individual segments of figure 5.11 b at a constant field of 8 MV/m.(site 3).

of the spectral peak shifts to lower energies with increasing field, and secondly how the spectral half-width (FWHM) also increases with increasing field. These effects are illustrated graphically in figure 5.14 and show how both the shift S and half width increase slowly at low fields (<8 MV/m), but more rapidly at high fields. However, it was found that the FWHM of some of the sites exhibits a field-dependence that was converse to that of the shift.

The second type of constant-gain spectral measurement, which is illustrated in figure 5.15, investigated how the spectral response varied from segment to segment. Thus, with reference also to figure 5.11b , it will be seen that there is a marked increase in the emission current density between the outer and innermost segments, coupled with a small but significant shift of the spectra maxima towards low energies. However, it is important to note that the magnitude of the shift involved in this latter effect is very much less than that observed between the individual spots of the image shown in reference 31.

5.4. Thermal stimulation of emission

This experiment was carried out in order to reinforce the existence of similarities in the emission behaviour of natural and artificial carbon sites, and to confirm the existance of a field-induced hot electron emission mechanism. Thus the measurement was made on both a natural and an artificial carbon site: this was the temperature-dependence of a spectrum [106,107].

In order to study the temperature-dependence of spectra under constant field conditions, it is first necessary to follow the room-temperature procedure described in section 5.1 for locating a chosen site on-axis opposite the anode probe hole. The specimen was then slowly heated to the maximum required temperature of ~700 K, with sufficient time being allowed for out-gassing and the chamber pressure to return to $< 10^{-9}$ mbar. Having set the gap to its required value (usually 0.5 mm), the field was slowly applied until the emission image of the axially located site was again visible on the phosphor screen. A chosen segment of the image could then be located over the probe hole and the other parts of the spectrometer facility were set ready to record a spectrum. At this stage, the heater power supply was cut off to avoid any voltage drop appearing across the electrical feedthrough. This precaution was necessary since the current flowing to the heater was normally ~0.5 A, which is sufficient to develop a voltage drop across the heater that would significantly affect the spectral shifts recorded at high-temperatures. By progressively lowering the temperature and making corrective adjustments to the gap width, constant-field spectra could be recorded from the same image feature over the full range of temperature.

Thus, figure 5.16 presents a typical spectral sequence recorded

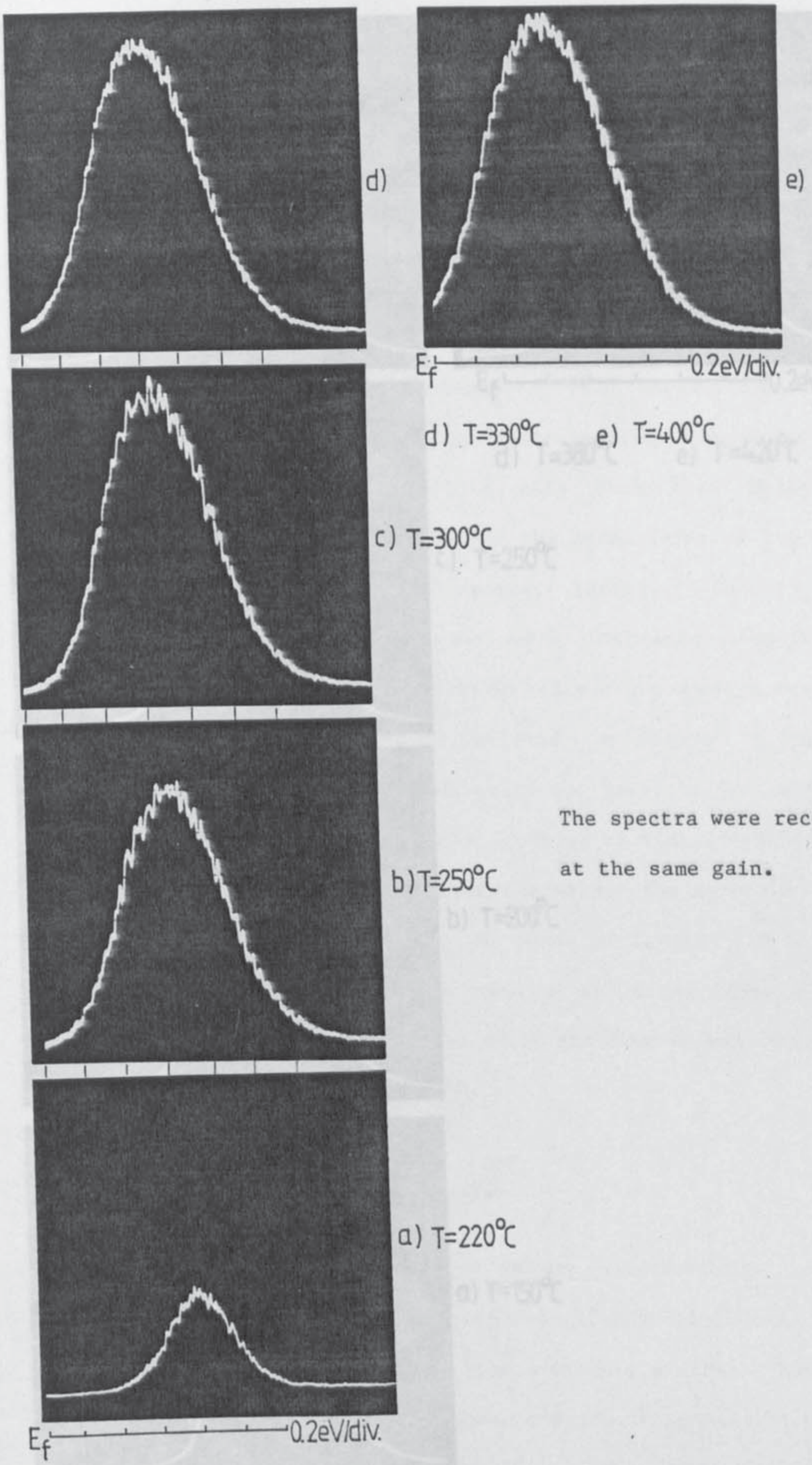

The spectra were recorded at the same gain.

Fig. 5.16 Spectra of a type 2 natural site on the surface of a Cu electrode recorded at temperatures ranging 300 K to 700 K at a field of 12.4 MV/m (site 4).

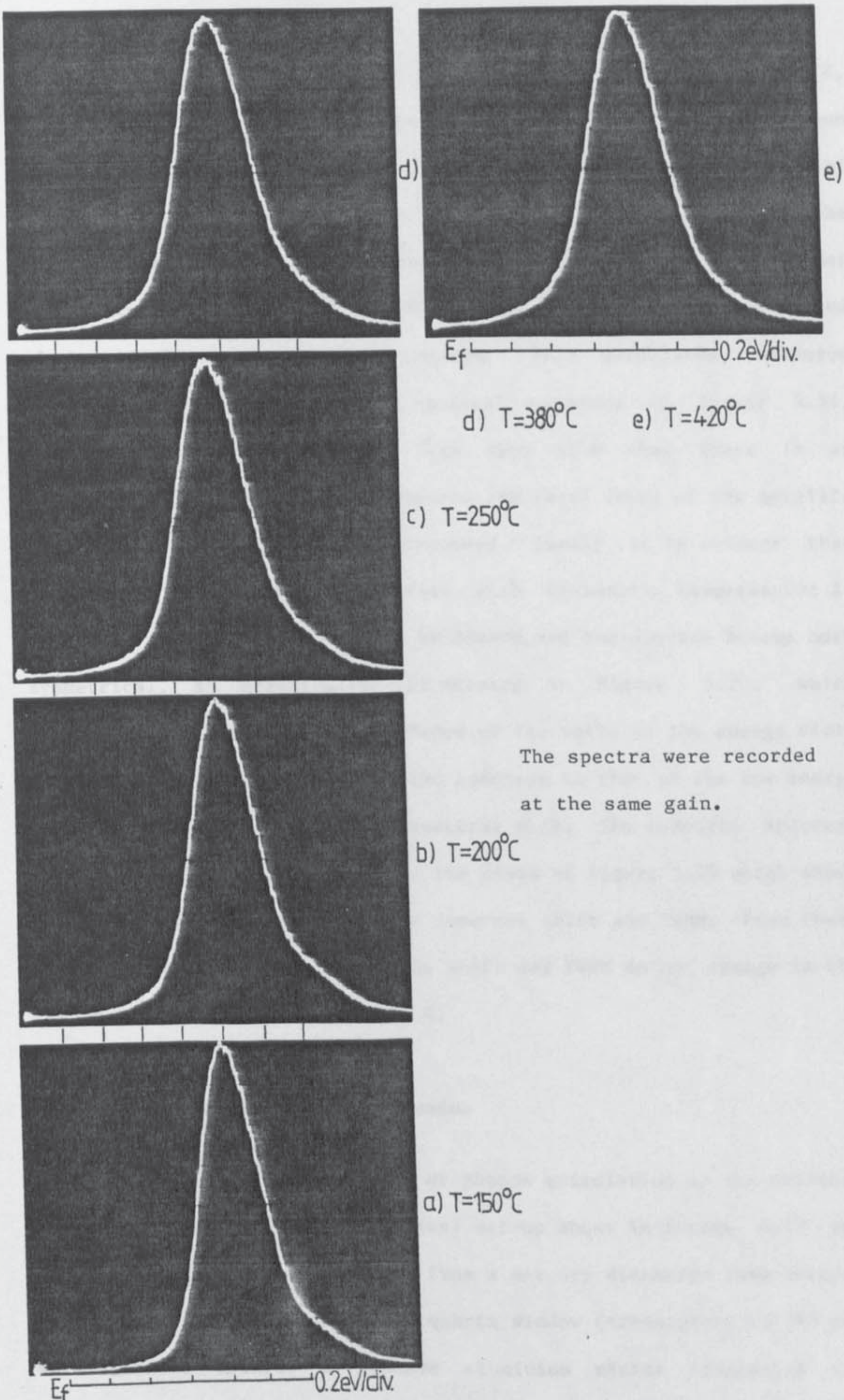

The spectra were recorded at the same gain.

Fig. 5.17 Spectra recorded from an artificial carbon site at temperatures of ~300 K to ~700 K (site 5).

from a natural site over the temperature range of 300 K to 700 K, while figure 5.17 shows a sequence of spectra of an artificial carbon site recorded at the same range of temperatures. From a comparison of these spectra, it can firstly be seen that the area, and hence the emission current,increases with temperature. This effect is further illustrated in figure 5.18, which presents the temperature dependence of the emission current under constant field conditions, measured directly from the complete spectral sequence of figure 5.16. Secondly, the spectra of figure 5.16 also show that there is an apparent shift in the peak towards the Fermi level of the metallic substrate as the temperature is inceased. Lastly, it is evident that the shape of the spectra varies with increasing temperature; in particular, the spectral FWHM is broadened and the spectra become more symmetrical, as graphically illustrated in figure 5.20, which represents the temperature dependence of the ratio of the energy width of the high energy tail of the spectrum to that of the low energy tail: both measured against the spectral peak. The complete spectral sequence has been used to compile the plots of figure 5.19 which shows the temperature-dependence of the spectral shift and FWHM. From these plots, it should be noted that the shift and FWHM do not change in the temperature range of 300 K - 400 K.

5.5. Photo-stimulation of emission

To investigate the effects of photon stimulation on the emission mechanism, the modified experimental set-up shown in figure 4.13 was employed. Here, optical photons from a mercury discharge lamp entered the chamber through a special quartz window (transparent to UV) and were directed towards a concave aluminium mirror (replacing the previous phosphor screen), which focuses them onto the cathode surface

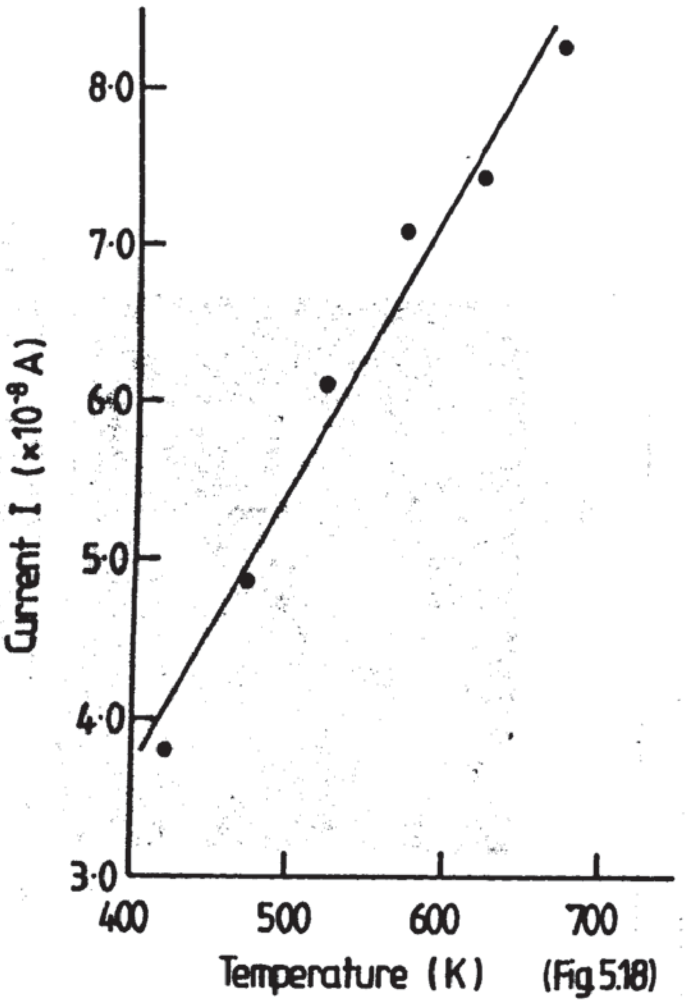

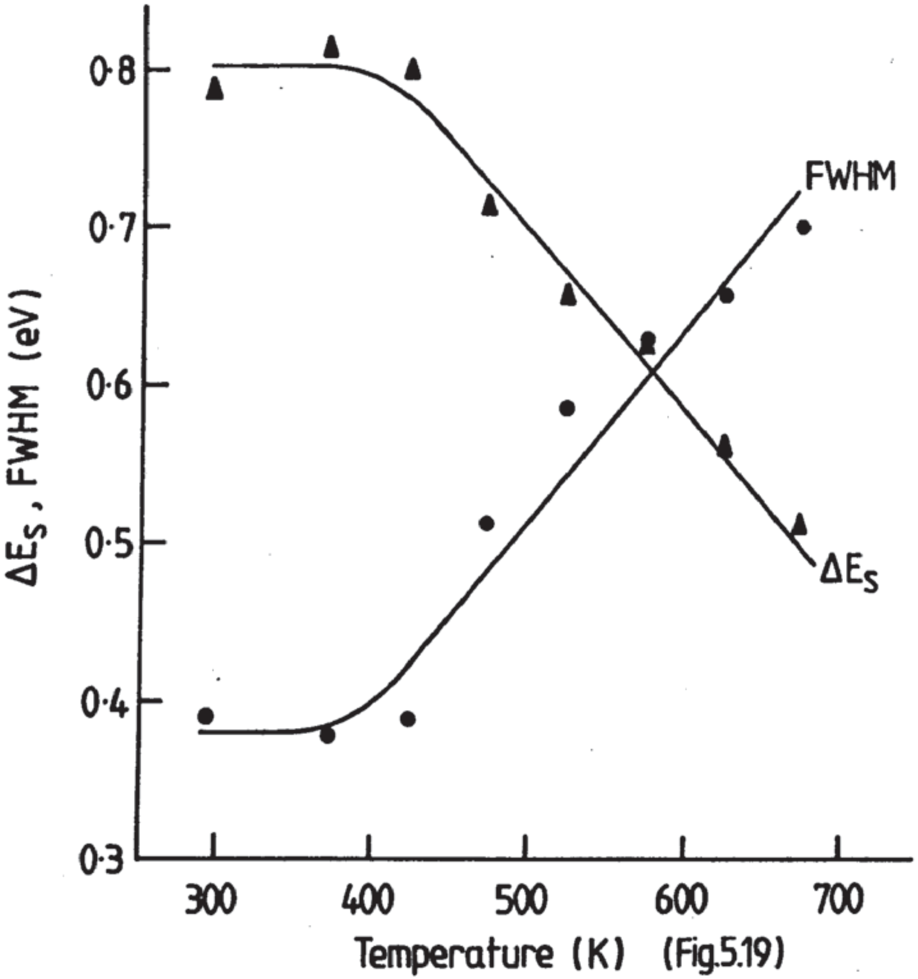

Fig. 5.18 Temperature-dependence of emission site current at a constant field of 12.4 MV/m.(site 4).

Fig. 5.19 Temperature-dependence of the spectral shift S, and half-width FWHM, at a constant field of 12.4 MV/m.(site 4).

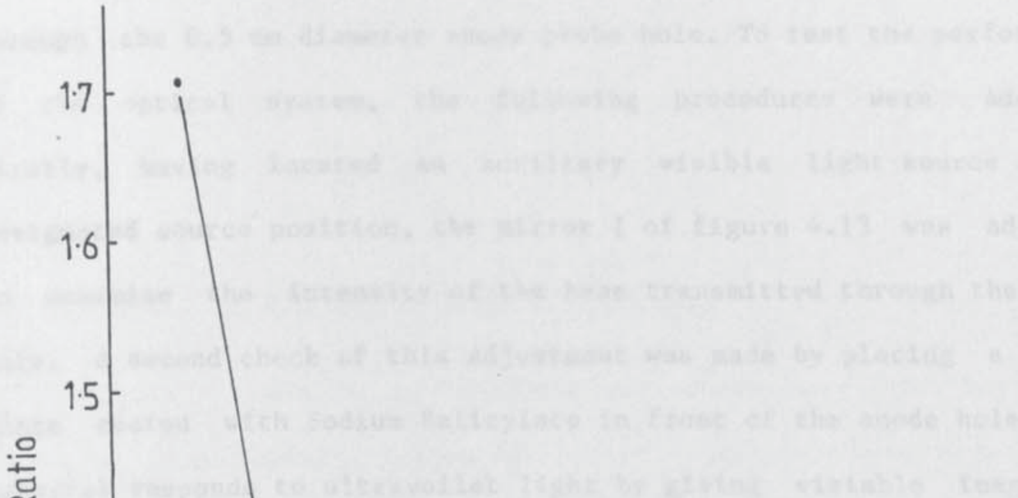

Fig. 5.20 The temperature dependence of the spectral shape.(site 5).

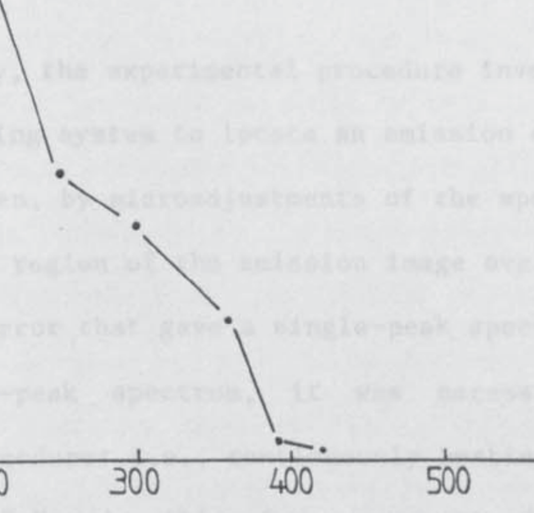

Fig. 5.21 Spectra recorded with and without UV radiation at a constant field of 11 MV/m.(site 6).

through the 0.5 mm diameter anode probe hole. To test the performance of the optical system, the following procedures were adopted. Firstly, having located an auxiliary visible light source at the designated source position, the mirror 1 of figure 4.13 was adjusted to maximise the intensity of the beam transmitted through the anode hole. A second check of this adjustment was made by placing a glass plate coated with Sodium Salicylate in front of the anode hole: this material responds to ultravoilet light by giving visiable image, so that the lamp could be further adjusted to give the brightest spot on the coated plate.

As previously, the experimental procedure involved firstly using the specimen scanning system to locate an emission site opposite the probe hole, and then, by microadjustments of the specimen position, to "blindly" locate a region of the emission image over the probe hole in the aluminium mirror that gave a single-peak spectrum. To obtain a repeatable single-peak spectrum, it was necessary to follow a time-consuming procedure: i.e., continuously heating the specimen at a temperature of ~700 K and waiting for a pressure of $< 10^{-9}$ mbar of the chamber at this specimen temperature ,so that a site can become more stable. This is an important procedure, otherwise, any apparent effect could be attributed to spurious variations in emission current. Then, the specimen was eventually cooled down to room temperature. After re-preparing the system to a pressure of $< 10^{-9}$ mbar, a stable, single-peak spectrum is recorded on a storage oscilloscope under "dark" conditions, the quartz window is then opened to UV radiation (λ=350 nm) and the spectrum again recorded under identical field conditions. Thus, figure 5.21 presents typical spectra which were measured respectively with and without ultraviolet radiation under a constant field of 11 MV/m. From inspection of this figure, it is evident that the emission current has been significantly increased by the UV radiation. The physical implication of this observation will be discussed in next chapter.

5.6 A study of gap-dependence of the β factor

In earlier studies of prebreakdown conduction and breakdown phenomena, experimental measurements of the gap-dependence of the β factor of the Fowler-Nordheim plot were reported by a number of authors. For example, Alpert [108] attributed it to a field enhancement effect of emitting sites on the edge of an electrode. Later, Jüttner [109] employed an anode probe hole technique to show the effect and to study sites and was therefore able to establish that the effect could not be related to the field enhancement of a site. Thus, Jüttner considered that the effect was associated with the voltage and therefore named it the Total-Voltage effect. However, this effect would not be expected by the FIHEE model and so it was decided to make the following measurements to establish whether the effect existed since a positive result would question the validity of the model.

The measurement benefitted from two techniques, viz., the direct measurement of the emission current from the spatial-resolved spectra, and the computer-aided plotting of the potential distribution in a test gap, including the influence of the anode probe hole. Since a sequence of spectra are measured from a single spot or segment, the spatial resolution of the analysis is better than the previous measurement; e.g. Jüttner could only construct an F.N. plot of a single site which might have consisted of several sub-spots or segments. Also, the latter field-plotting technique has provided a correction to the electrical field on the surface region of a cathode

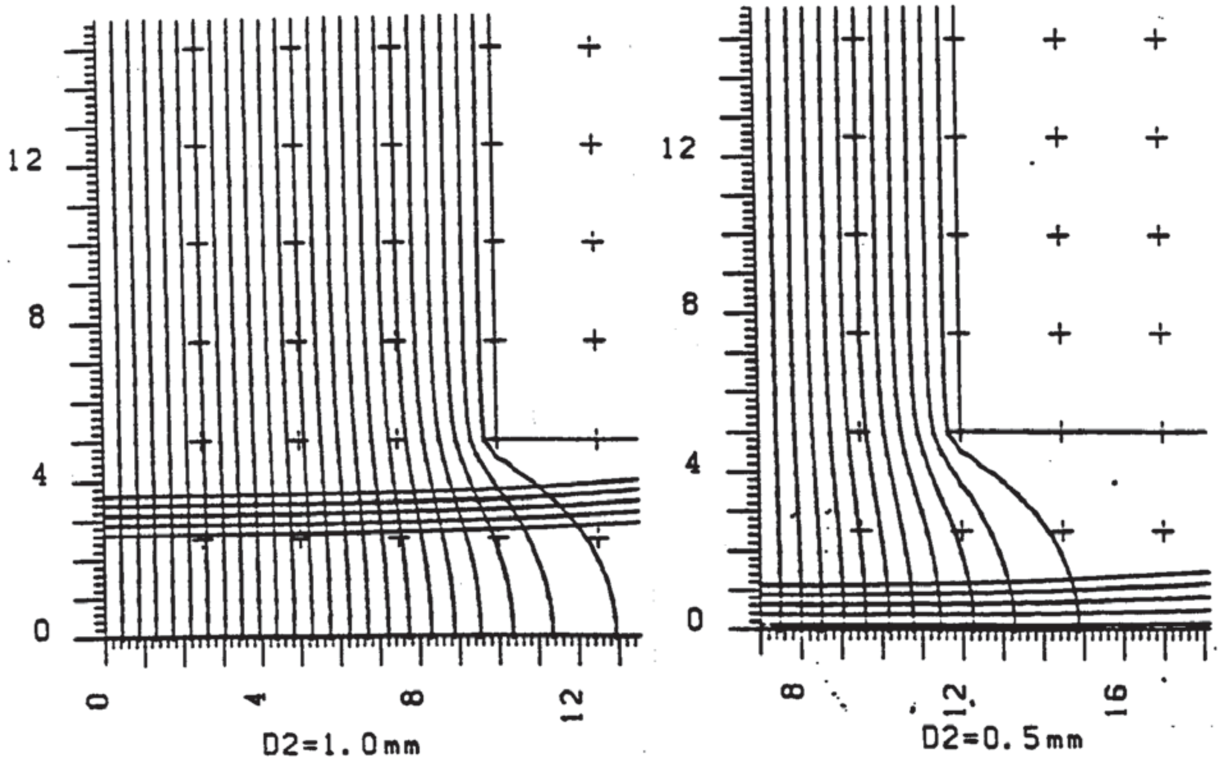

D2=1.0mm

D2=0.5mm

Fig. 5.22 Potential distribution on the cathode surface region opposite an anode probe hole.

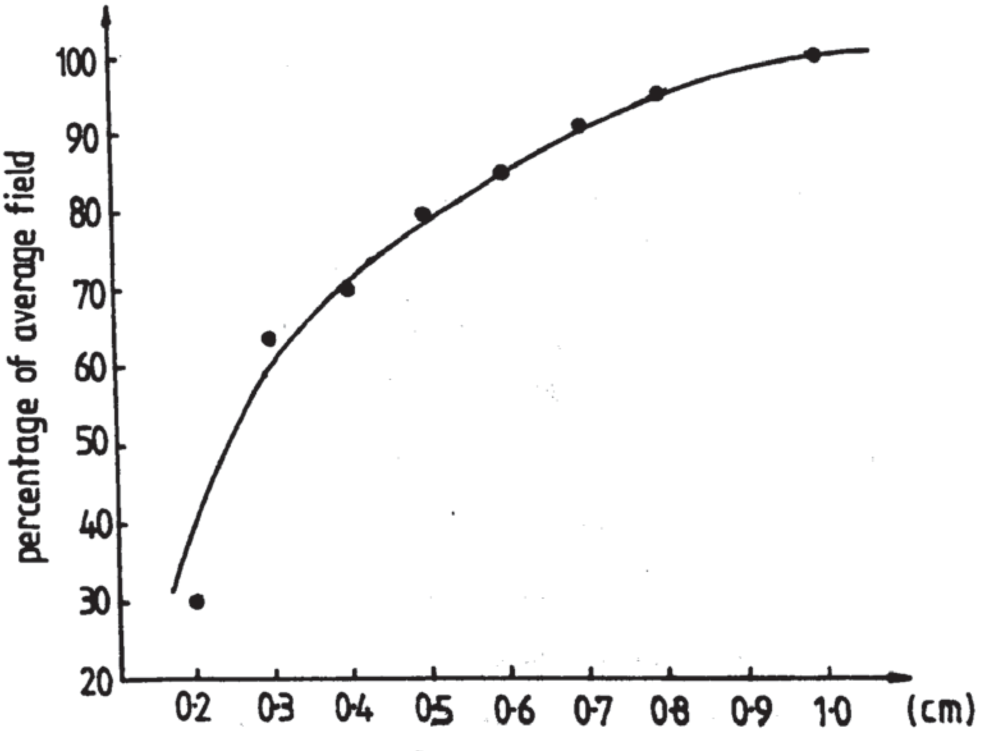

Fig. 5.23 The variation of the macroscopic gap field on the cathode surface region opposite an anode probe hole.

opposite an anode hole. To illustrate the existence of the variation of the field in this region, figure 5.22 shows the potential distributions of two test gaps of different spacings. It will be seen that the field in the region specified above is weaker than the average at gap separations of less than 1.0 mm, while the difference between the average and that of this region decreases with the increasing of gap-separation up to 1.0 mm. By measuring the distance between the cathode surface and the equipotential line nearest to this surface, these differences can be ultimately determined and they are shown by the curve in figure 5.23.

Thus, figure 5.24a illustrates how the β factor increases with the gap separations ranging from 0.45 to 0.75 mm when the reduction of field resulting from the presence of the anode hole is not taken into account. In particular, the differences between the maximum and the minimum, and between the maximum and the average, are ~260 and ~130 respectively. On the other hand, figure 5.24b shows another plot where the field reduction was taken into account, i.e. there is no significant increases of the β factor. Further calculation shows that the deviations of this latter plot are < 5%, which is to be expected when the former technique is used [32].

Therefore, this measurement apparently shows that there is no Total-Voltage effect and also suggests that earlier positive results were a consequence of ignoring the variation of the field. However, the shortcoming of this measurement is that it only represents a narrow range of the gap separation. Nevertheless, it suggests the effect may be ignored for measurements where the gap separation is bigger than 1 mm for an anode hole of 0.5 mm, since in this range, the variation of the field on the cathode surface has been shown experimentally to be insignificant.

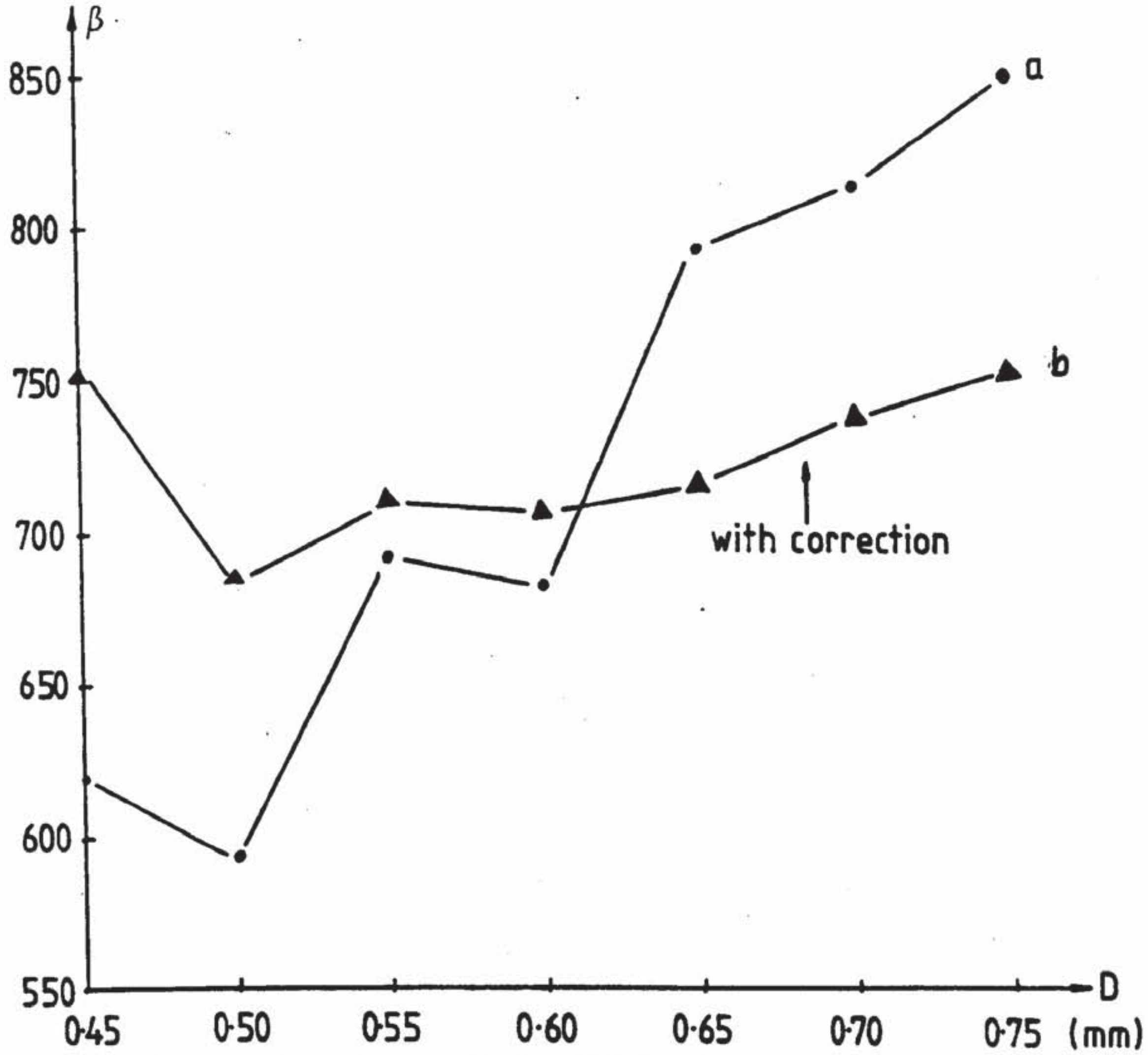

Fig. 5.24 The dependence of the field enhancement factor β upon the gap spacing: (a) without correction for field variation, (b) with correction for field variation.(site 7).

5.7. The electronic recording of an emission image

The electron energy-selective display technique described in section 4.3 was firstly used to replace the conventional optical method of imaging an emission image. To reproduce the visual appearance of an optical image, the electronic system must operate in an "open window" mode; i.e. where the energy window is > 2eV, so that all electrons transmitted by the probe hole are collected. In this way an electron image could be recorded on a storage oscilloscope. In order to assess the performance of the technique, examples are presented of both the "electronic" image, that is recorded in a storage oscilloscope, and the "optical" image that is photographed from the phosphor screen. Thus, figure 5.25.1a presents an image of a site, which only consists of a single spot, whilst figure 5.25.2a another image of a single segment of a natural site. As can be seen, they closely resemble their "optical" images shown in figure 5.25.1b and 5.25.2b respectively. It can be seen, for example from figure 5.25.2, that the non-homogeneity of the inner edge of the segment is clearly shown in the "electronic" image and that the curvature of the outmost edge of the segment can be measured to be very similar to its "optical" one. However, the capability of the facility is not limited to the above particular situations. Thus, figure 5.25.3 is a typical image of a multi-spot site. It can be seen, from figure 5.25.3, that to show the diffused edges of the three spots (see figure 5.25.3b), the "electronic" image gives a random distribution of dots in these edges. Equally, figure 5.25.4a presents just such an "electronic" recording of a typical multi-segment image which is seen to closely resemble its "optical" equivalent shown in figure 5.25.4b. In fact, a comparision of the two images reveals that the "electronic" recording, with its far greater electron detection sensitivity, contains more structural detail than the diffuse optical recording.

5.8 The energy-selective analysis of emission images

Since the spectrometer is a differential type, the energy window could be gradually changed from a minimum value of ~25 meV, determined by the resolution of the spectrometer to 10 eV. Consequently, the spatial distributions of electrons of different selected energies can be recorded as a "bright" image on a storage oscilloscpe by selecting an appropriate energy-window.

5.8.1. Analysis using a narrow energy-window

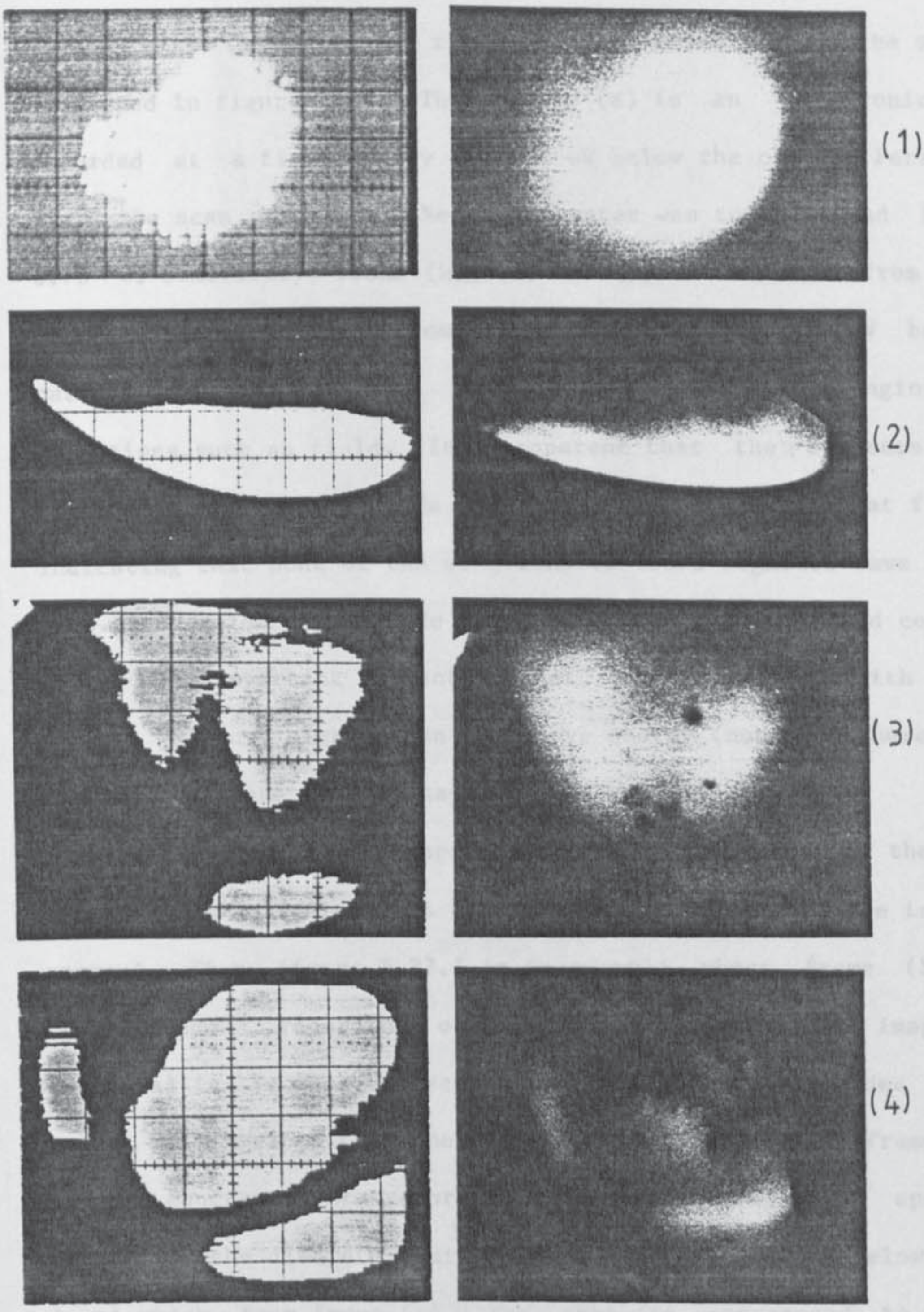

Fig. 5.25 Examples of emission images: (a) recorded from a phosphor screen with the conventional "optical" method, (b) recorded from a storage oscilloscope with the electron-energy selective display facility.

A first example of the analytical capability of the system is presented in figure 5.26. Thus, frame (a) is an "electronic" image recorded at a fixed energy of 0.53 eV below the cathode Fermi level; i.e., the scan voltage of the spectrometer was tuned to and fixed at 6.76 V. Similarily, frame (b), (c) and (d) was recorded from the same image at fixed "energy windows" of 0.47, 0.42 and 0.37 eV below the cathode Fermi level respectively without changing other conditions,such as field. It is apparent that the segments on the right and left hand side of the image disappear at frame (d), indicating that none of the electrons of these segments have an energy of 0.37 eV below the cathode Fermi level under these field conditions. It is also important to mention that, other recordings with energies of the "window" higher than the above energy (not shown here) did not display the segments that had previously disappeared.

The facility was also applied to a comparison of the spatial distribution of electrons of different energies that are in a single segment. Thus, figure 5.27.1 is an example where frame (b) is an "open window" recording of a typical single-segment image, whilst frame (a) is the energy spectrum of the emission recorded with the probe hole located near the convex edge of the image. Frames (c) and (d), in contrast, were recorded respectively with the spectrometer tuned to the discrete energies of 1.5 eV and 0.71 eV below the Fermi level which, from frame (a), are seen to correspond to identical current values, but on the opposite slopes of the energy distribution. Under these conditions, the width of the energy window is determined by the resolution of the spectrometer, i.e. ~ 25 meV. From a comparison of frames (c) and (d), in conjuction with (b) of figure 5.27.1, it will be seen that the lower energy electrons (transmitted at a scan voltage of 7.73 V) have a wider spatial distribution, and

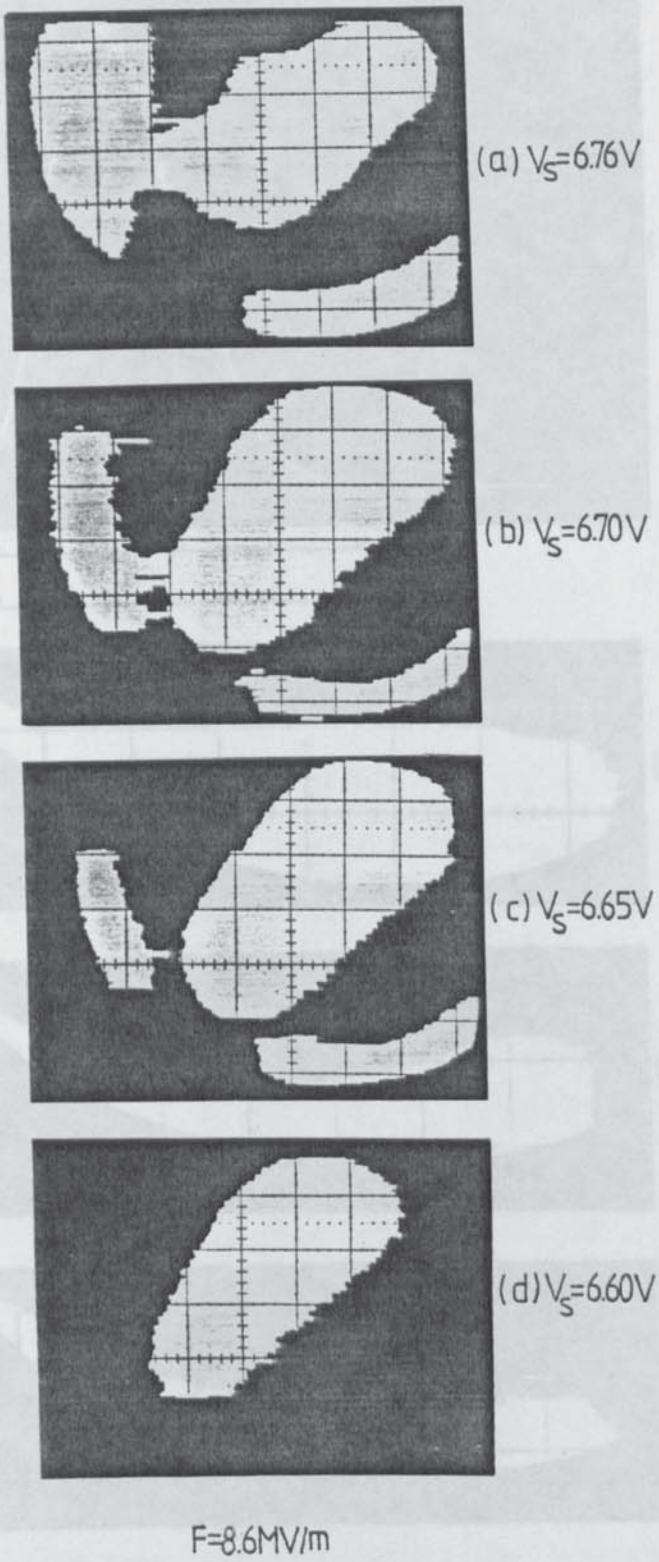

Fig. 5.26 The spatial distributions of electrons of a multi-segment image, recorded with different "energy windows" of the spectrometer.(site 8).

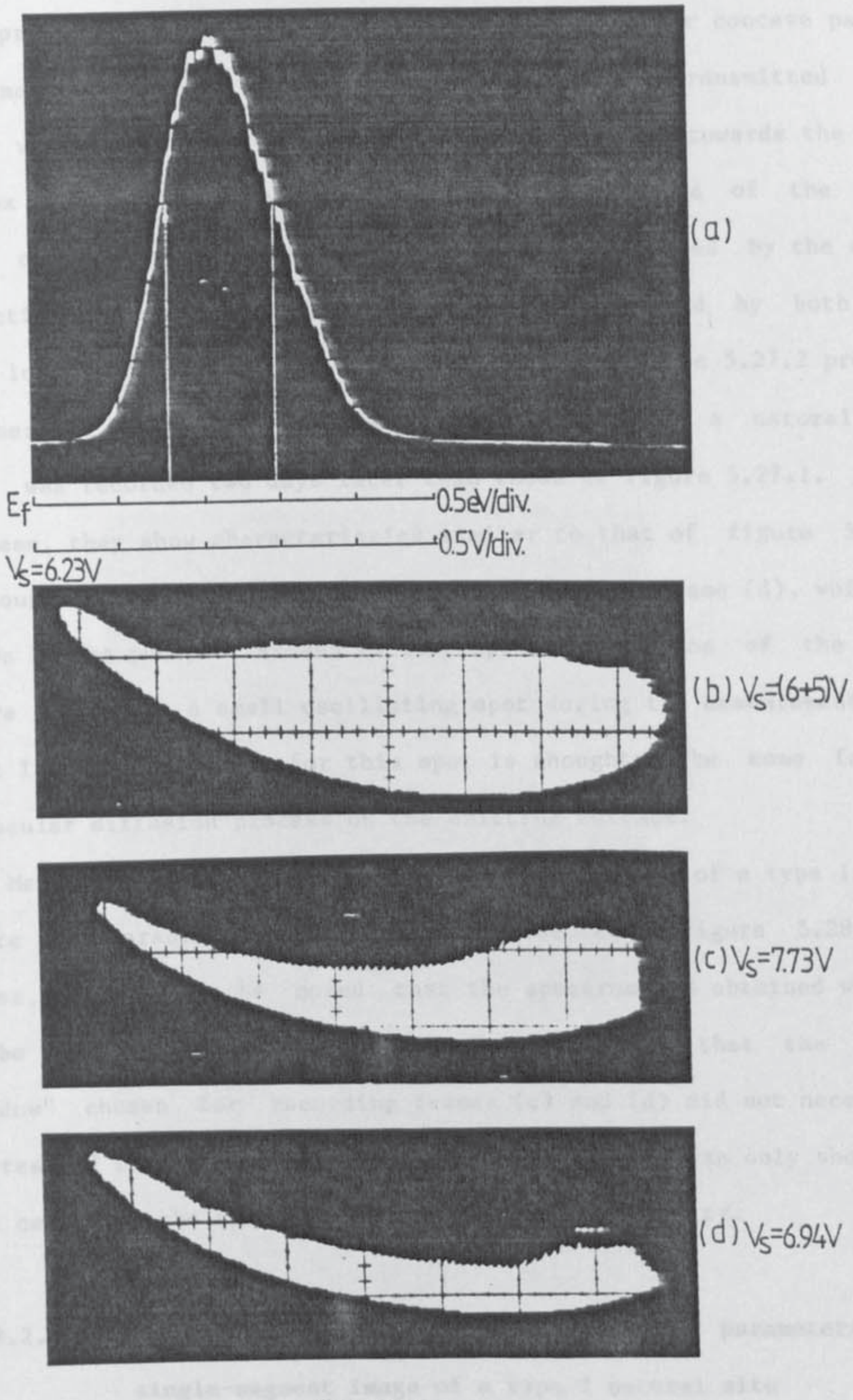

Fig. 5.27.1 The spatial distributions of electrons of a single segment, recorded with different "energy windows" of the spectrometer.(site 9).

are predominately responsible for forming the inner concave part of the image: conversely, the high energy electrons (transmitted at a scan voltage of 6.94 V) are preferentially located towards the outer convex edge. It is also significant that the profile of the outer edge of the segment appears to remain unaffected by the energy selection procedure; i.e. indicating that it is imaged by both high and low energy electrons. In a similar way, figure 5.27.2 presents another set of results from a single-segment image of a natural site that was recorded two days later than those of figure 5.27.1. As can be seen, they show characteristics similar to that of figure 5.27.1, although a "clump" shows up in the inner edge of frame (d), which was shown by the phosphor screen to correspond to a region of the image where there was a small oscillating spot during the measurement. The most likely explanation for this spot is thought to be some form of molecular diffusion process on the emitting surface.

Measurements were also made on a single spot of a type 1 image, where a comparable set of results are presented in figure 5.28. For these, it should be noted that the spectrum was obtained with the probe hole located at the "centre" of the spot, and that the "energy window" chosen for recording frames (c) and (d) did not necessarily correspond to the same current density. Thus, they can only show that the centre of the spot has the highest current density.

5.8.2. The field-dependence of geometrical parameters of a single-segment image of a type 2 natural site

The application of the electron energy-selective display facility to a study of the influence of the applied field on the geometrical structure of a segment has two obvious advantages over the optical method. On the one hand, because the technique can be used to record

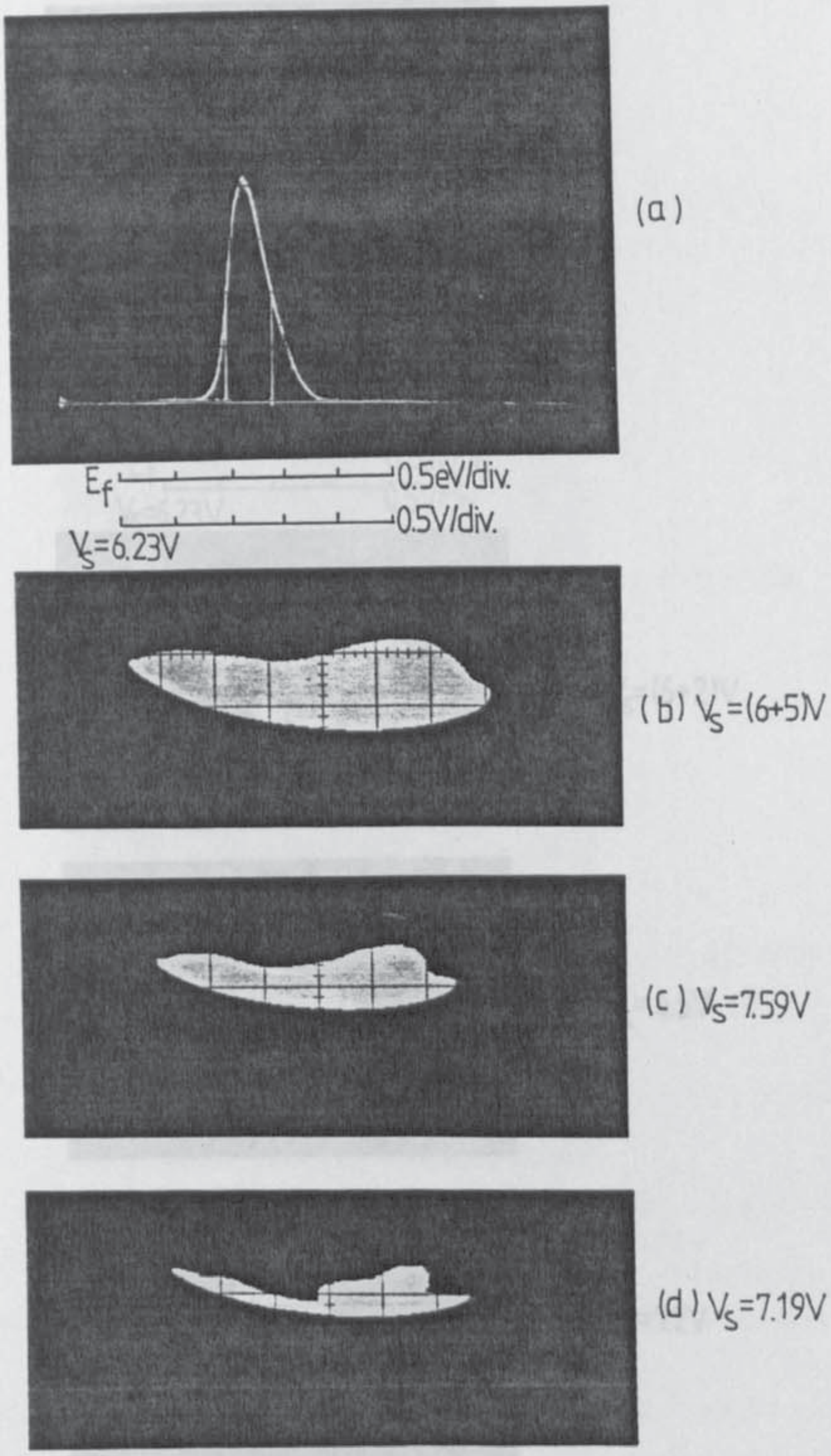

Fig. 5.27.2 The spatial distributions of electrons of a single segment, recorded with different "energy windows" of the spectrometer.(site 9).

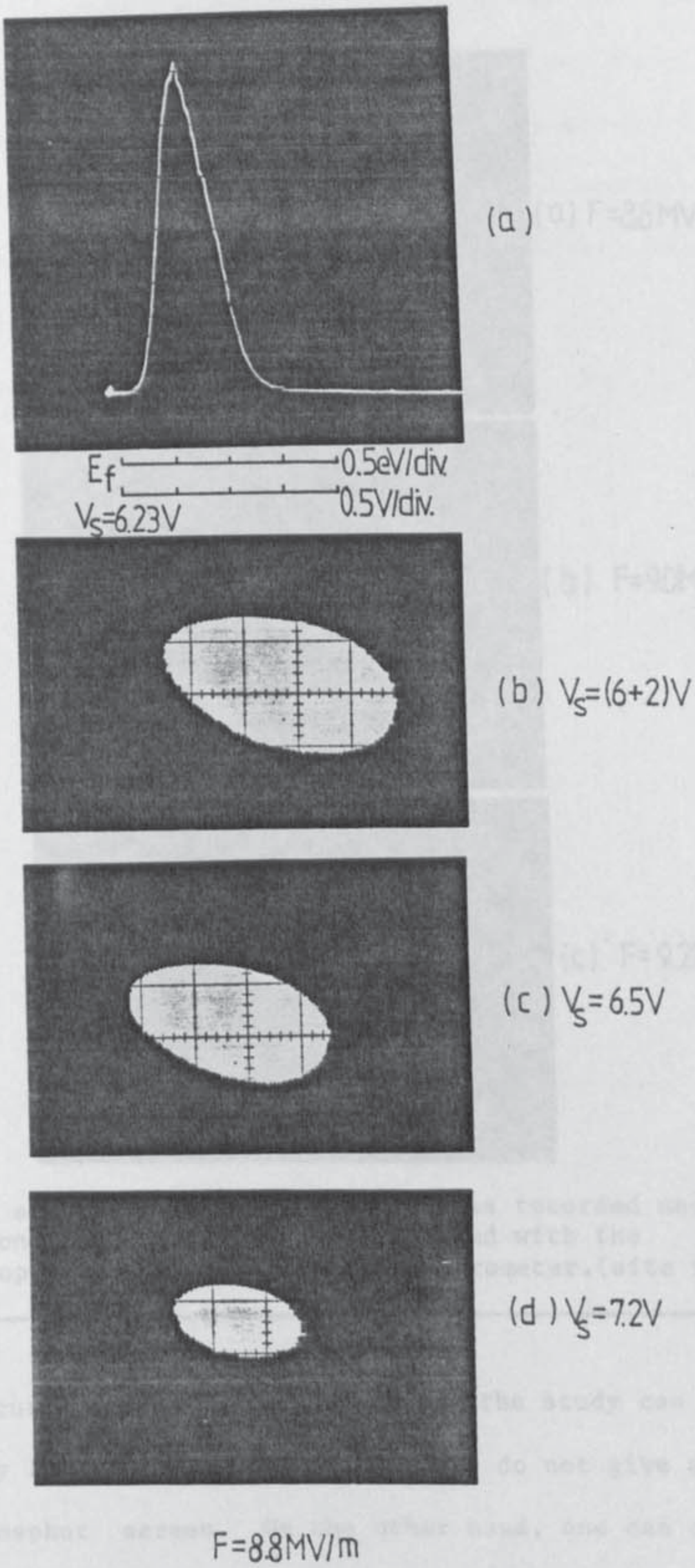

Fig. 5.28 The spatial distributions of electrons of a single spot, recorded with different "energy windows" of the spectrometer.(site 10).

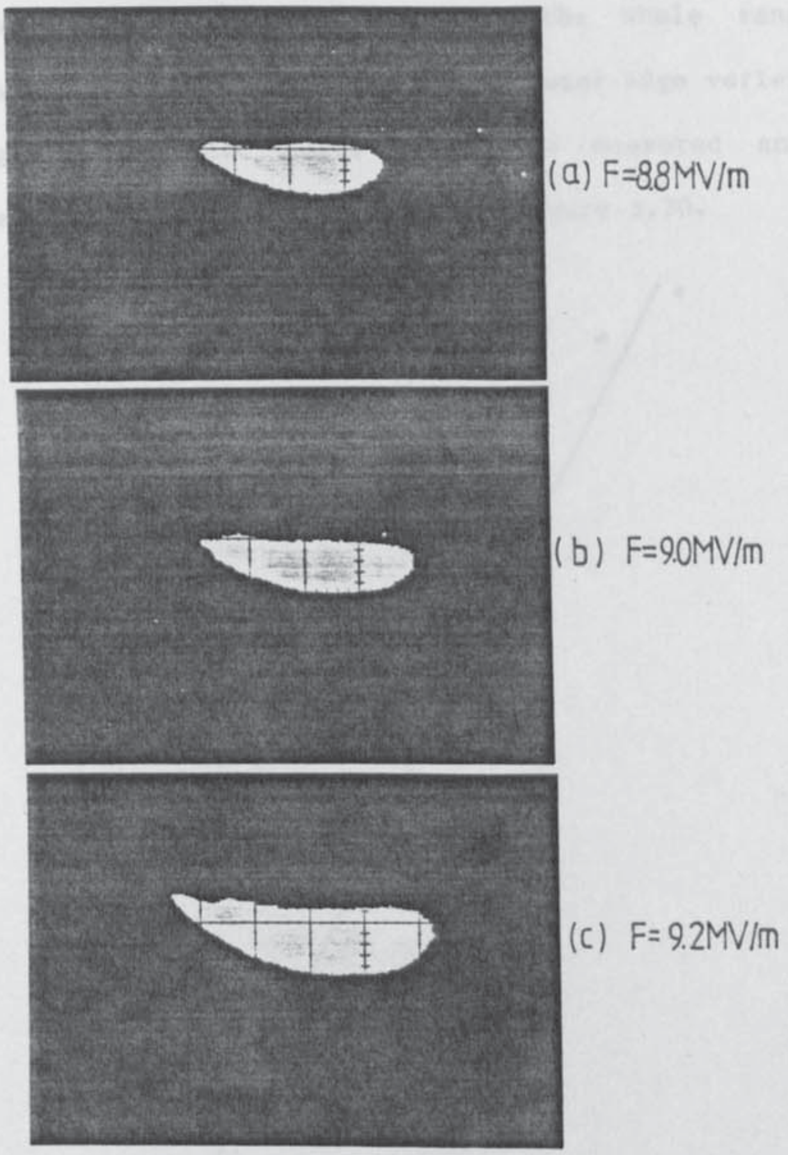

Fig. 5.29 A series of single-segment images recorded under condition of increasing field and with the "open-window" mode of the spectrometer.(site 9).

---

a very low current-density electron beam, the study can be extended to a relatively low fields at which electrons do not give a visible image on the phosphor screen. On the other hand, one can obtain a "true" image by avoiding the effect of the non-homogeneity of the phosphor screen which may give rise to a distored image.

Thus, in figure 5.29 a coherent sequence of recorded images at fields ranging from 8.8 MV/m to 11.6 MV/m are presented. They illustrate, firstly, how the overall size of an image increases with the field; secondly, how the outer edge remains well-defined while, in contrast, the inner edge changes randomly over the whole range of field and finally, how the curvatures of the outer edge varies with field. The length of the arc edges were also measured and the field-dependence of the length is presented in figure 5.30.

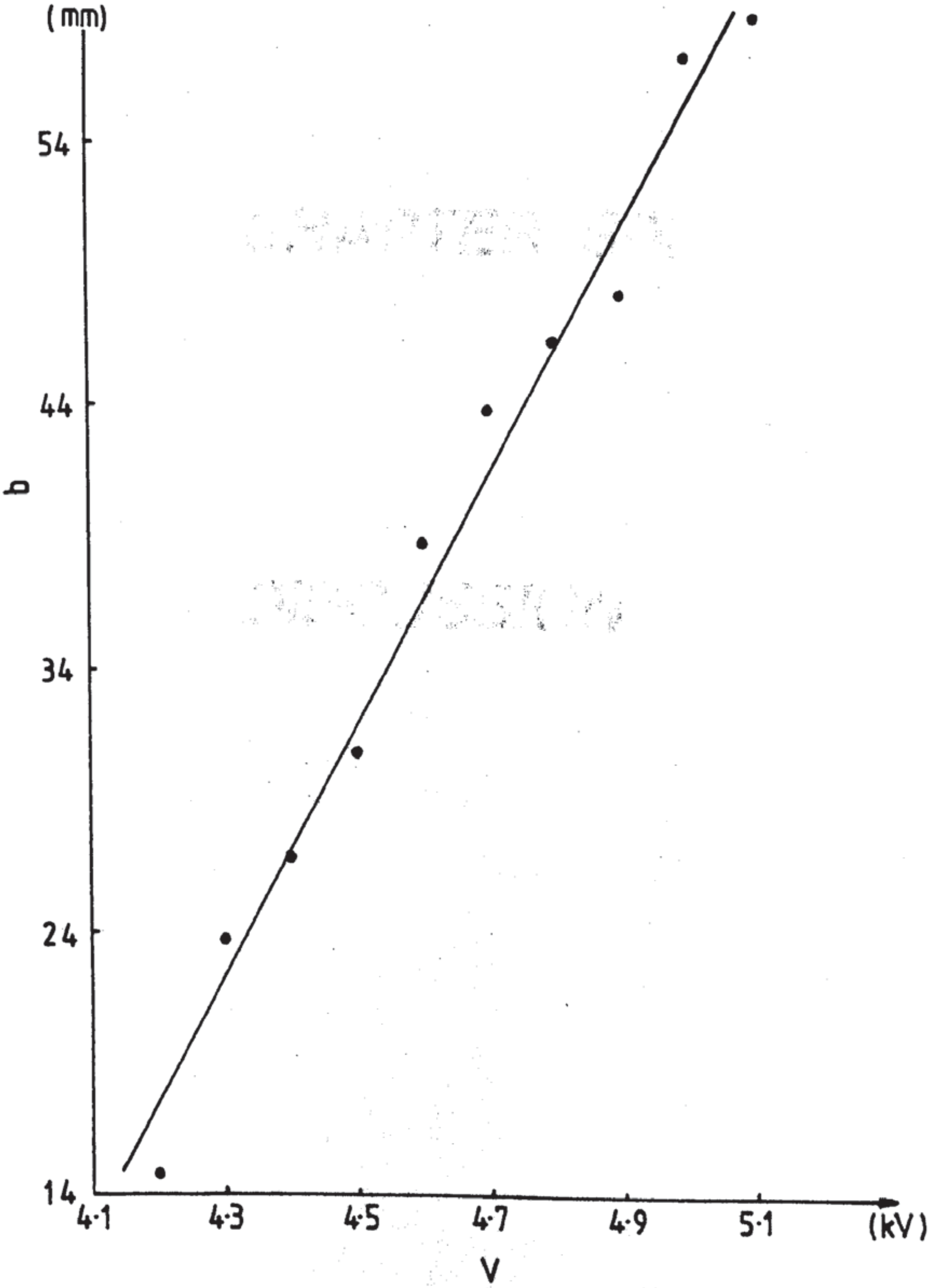

Fig. 5.30 The field dependence of the length of the outer arc edge of the images shown in figure 5.29.(site 9).

CHAPTER SIX

DISCUSSION

6.1. General observations on the principal experimental findings

In previous chapters, a wide range of evidence has been presented, both theoretical and experimental, which contradicts the existing model. For the purpose of the following discussion, it would be helpful to summarise the important experimental findings that have emerged from this investigation.

(i) Both the field emission imaging and electron energy-selective display techniques have revealed that two types of emission site exist, which are characterised by distinctive emission images. Apart from those giving a diffuse spot-like image (type 1) discussed by Bayliss & Latham [9], a second type of image has been identified (type 2) which consists of arc-like elements, and is similar in character to those observed by Simmons et al from purpose-fabricated MIM devices [8]. Furthermore, the new technique has revealed that (a) the geometrical parameters of the arc-like elements are field-dependent; (b) individual arc-like elements of a composite image can have different electron energy distributions; (c) the two types of site have different current density distributions within a sub-spot or a segment; (d) the majority of high energy electrons are found near the sharp convex edge of a segment, whilst conversely, the ill-defined concave region of the image is composed mainly of low-energy electrons.

(ii) The electron energy spectra sampled from individual segments of type 2 sites have characteristics similar to those obtained from the individual spots of the type 1 sites studied by Bayliss et al [9,32], and described in section 2.3. These include the single-peak characteristic, the field dependence of the spectral shift and FWHM. It is particularly important to note that all electrons are emitted from energy states below the cathode Fermi level. In addition, the switch-on behaviour and the I-V characteristic, as represented by an

F.N. plot, have also shown no significant difference from those obtained from type 1 sites.

(iii) Artificial emission sites formed by depositing graphitic carbon particles on an ambiently or intentionally oxidised electrode surface have been shown to have emission characteristics that are similar to those obtained from type 2 natural sites.

(iv) The similarities referred to in (iii) above have been reinforced by thermal and phonton stimulation studies which have demonstrated how an emission site responds to these external influences.

Thus, the central finding of this investigation is the existence of a type of emission site that gives an image consisting of arc-like elements. We shall now discuss why some sites give rise to this type of "geometrical" image, rather than an assembly of ill-defined diffuse spots and the physical mechanism by which they are formed. Several effects can be rapidly excluded. Firstly, it is not a consequence of an electron optic effect associated with the field emission imaging system, since both types of emission image have been revealed by the system under similar operating conditions. The suspicion that a single segment may result from a shielding effect by the wall of the cylindrical lense element was also eliminated by moving the cathode; i.e. by micro-adjusting the position of a site opposite the anode hole to check whether or not there is any change in the size or radius of a segment. Secondly, it is not the result of a shadow effect from the particles on the electrode surface, since one can not see how this effect can explain the formation of multi-segment images. Thirdly, it is not a consequence of an "aperture" diffraction effect (e.g. from a pinhole in the top electrode). There are three reasons to support this latter contention.

(a) Figure 5.15 shows that the electrons forming different segments of an image have different energies, i.e. as illustrated by the significant peak displacements among spectra recorded from neighbouring segments. This finding has also been confirmed by an equivalent result shown in figure 5.26, obtained with the energy-selective display facility, which shows how two segments disappear when the spectrometer is tuned to energies higher than a certain value. It follows from this reasoning that the segmental images are not a consequence of the conventional coherence effect.

(b) It has also been shown that the spatial distribution of the electron current density does not have the form predicted by the Huygen´s principle, namely that the cèntral part of the diffraction pattern should correspond to the region having highest current density. Although figure 5.15 indicates that the current density increases gradually towards the inner segment in the image, it is not a typical situation, since it is obvious that on its opposite side, the current density of the outer segment is seen to be higher than that of the more inner segments.

(c) All of the arc-like elements subtand an angle of < 180°.

Finally, it can be assured that the effect is not caused by an inhomogeneity in the phosphor screen, since the electron energy-selective display technique has also displayed a similar arc-like structure.

Considering these images from a different point of view, it is firstly very important to reiterate that the emission characteristics are similar to those observed with artificial carbon sites. With this type of emission regime, as discussed by Latham et al [33], graphitic carbon particles are deposited on an ambiemtly oxidized electrode surface, and consequently can be expected to form MIM microstructures where the field induced hot electron emission mechanism will be able to operate. In this context, as discussed in section 3.3.4, Simmons et al [8] have demonstrated that there is a certain range of field, in which hot electrons may be emitted into vacuum following a coherent scattering process at the edge of the top metal layer of a MIM microstructure, and as a consequence, give rise to emission images consisting of arc-like elements. The geometrical similarities between the emission images obtained from MIM device structures and those presented in the last chapter have been established in detail in references 105 and 107; more recently, however, data collected from the studies involving the new spatial analysis technique have also confirmed that the images from the present emission sites have the spatial distribution of electrons predicted by the diffraction theory of Simmons et al [8,88]. On the basis of this evidence, it is believed that the type 2 emission image comes from a similar emission regime and thus strongly suggests that MIM microstructures occur naturally on the surface of broad-area electrodes.

In fact, for the coherent scattering process to occur successfully, the top layer is required to be conducting, otherwise, it would not be possible for electrons to be emitted through an insulating layer at different angles. With a MI structure, for example, it would be necessary to assume that many discretely orientated channels are formed in this layer, which seems unlikely, according to present experimental observations. Secondly, it is apparent from measurements of the energy distribution of electrons in the arc-like image that the emission regime must involve some kind of insulating structure since all of the electrons are definitely emitted from the energy states below the cathode Fermi level. Thirdly, the micropoint anode probe technique of Athwal & Latham [5] or Niedermann et al [6], already described in chapter 2, have revealed that the emitting particles frequently contain metallic elements and are seen to be charged under a scanning electron microscope. On the basis of the above considerations, a modified FIHEE model will now be presented, as it operates with MIM microstructures. The essentials of this model have been qualitatively outlined in previous publications [105,107,114], but here a more detailed consideration will be given to the physical processes involved.

6.2. The modified FIHEE model

6.2.1. The emission regime

Figure 6.1 is a schematic illustration of the emission regime associated with the type of MIM microstructure which is assumed to occur naturally on the surface of broad-area electrodes. The general features of this structure are that a polycrystalline metal layer of thickness of > 50 Å in the direction of the applied field which is assumed to sit on top of an insulating particle or inclusion having a thickness of 50-1000 Å in the field direction, and also to be electrically insulated from the substrate electrode. The top metal layer of this structure will mainly play the role of an isolated conducting sheet, and could therefore change the field distribution as illustrated; in particular, it could act as an antenna and enhance the field locally across the junction where it forms a contact with the electrode surface. Also, since the insulating layer will initially block the transport of carriers from the substrate metal, this field enhancement will eventually lead to a significant voltage drop across the insulating layer between the conducting sheet and the metal substrate. In principle, the field enhancement can be calculated accurately: however, for simplity, it is assumed that the potential of the conducting sheet of height $h=l+d$ (see figure 6.1b) will be equal to that of equi-potential surface that is situated at a distance of h above the cathode surface. Accordingly, the field enhancement in the

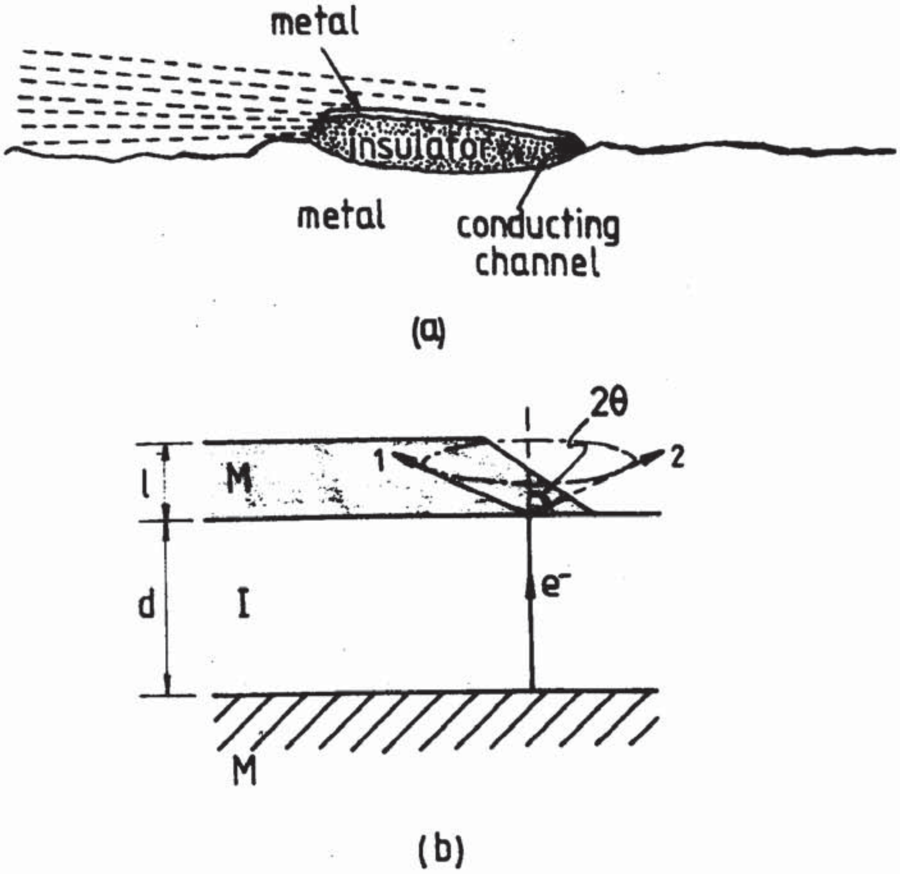

Fig. 6.1 The emission regime of the modified FIHEE model.

insulating layer will be of magnitude of h/d, where d is the thickness of the insulating layer. In particular, at the Metal-Insulator-Vacuum triple junction, enlarged in figure 6.1b, the enhancement will exceed the average value across the contact region. Therefore, it is likely that conduction channels will be formed preferentially in this region when the electrical field is applied to the gap.

6.2.2. **The swich-on mechanism**

This alternative qualitative model is based on the same important experimental findings of the earlier FIHEE model. These are that two conditions are usually required to initiate a switch-on process; namely a voltage "surge" superimposed on some threshold gap-voltage. In addition, we shall also consider the observed form of the I-V characteristic associatied with the switch-on process, i.e., as illustrated in figure 5.3. Furthermore, we should reiterate the fundamental fact that a conduction channel has a conductivity that is very much higher than the surrounding un-formed dielectric region.

It is now assumed that the conditions of the interface between the cathode and insulator are similar to that suggested by the earlier model; i.e., the interface forms a blocking contact, and that there will be one or more microscopic locations on this interface where the local electronic conditions present a favourable tunnelling contact. As proposed by Dearnaley [59] for an oxide dielectric, these could be created by local concentrations of oxygen vacancies, which would then provide high concentration of donors. It is further assumed that the dielectric is some form of compound, such as a metal oxide, that consists of a heavier metal atom and light oxygen atom.

As with the earlier model, and illustrated by figure 6.2a, electrons will tunnel into the conduction band of the insulator once the applied field reaches a certain value, and subsequently travel under the influence of the high penetrating field. Thus, according to the discussion in section 3.3 and Fischetti [75], they will be heated to some energy that will depend on their mean free path and the strength of the electric field. However, they will eventually be cooled by giving up their energy to the local lattice [75]. Then, as suggested by Dearnaley [59], if the local temperature of the lattice is $> 5T_\theta$, where T_θ is the Debye temperature of the lattice, the oxygen atom of the compound can vibrate and break away from its molecular bond to leave the hearvier metal atom behind. The calculation for a alkaline metal oxide, given by Dearnaley [59], indicates that the relatively low temperature of 1100° C, i.e. < 5 eV, would be sufficient for this process, where such an energy would be readily gained by the electrons in such high fields [75]. It follows that

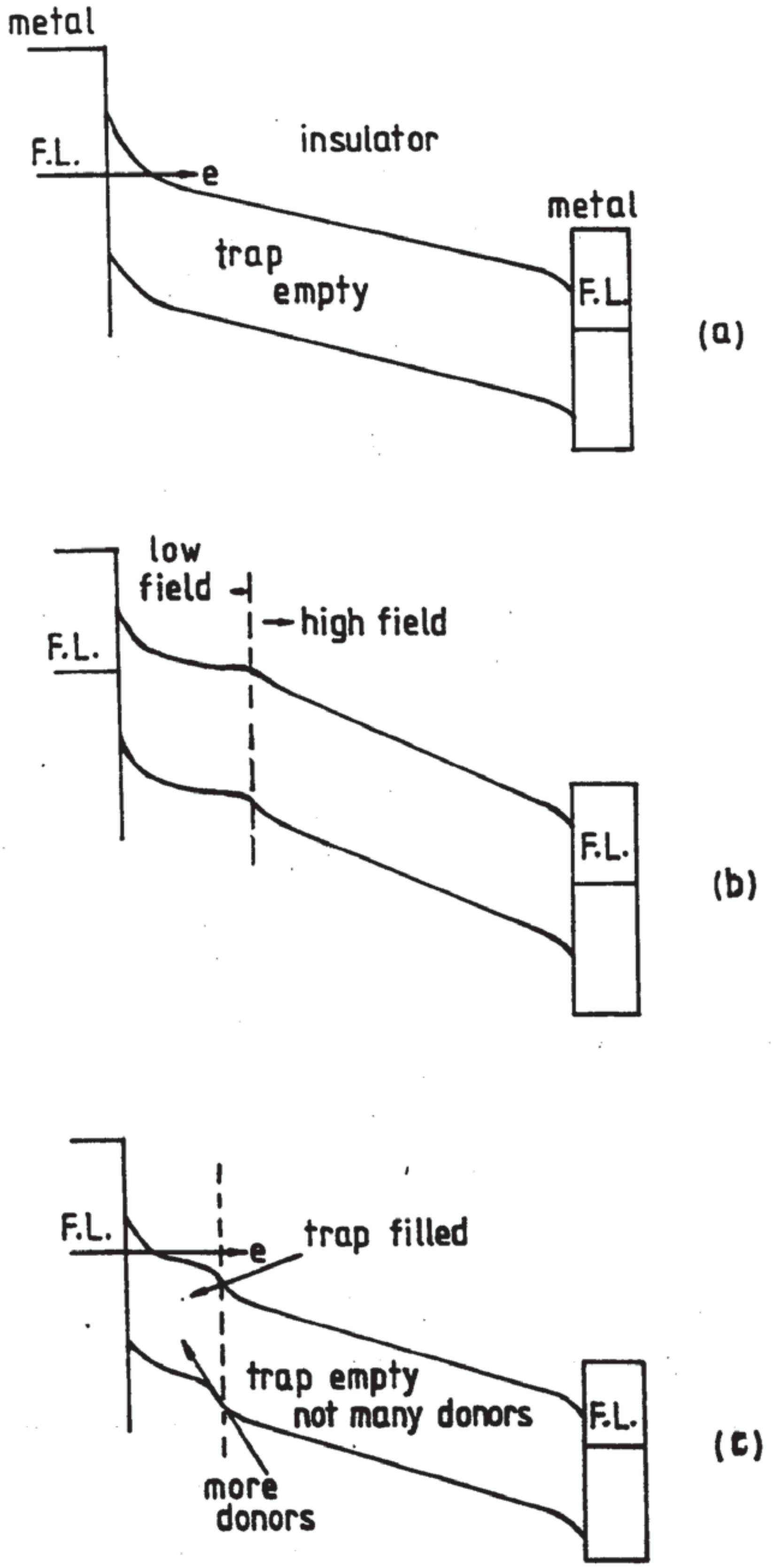

Fig. 6.2 The energy band diagrams showing the switch-on process.

once this process is complete, the cooled electrons will be trapped in a region having a length comparable to their mean free path, where the number of the donor centres, and consequently the conductivity of the "formed" region will be dramatically increased. Accordingly, the potential drop across the region would decrease and it may be assumed that under the existing applied field conditions, electrons can no longer tunnel through the contact. This situation is illustrated in figure 6.2b, which also shows that, in contrast to the formed region, the unformed region is under the influence of a high field. In order that electrons may tunnel through the contact, travel to the end of the formed region, and then be heated in the region right next to the previously formed region, the external field has to be further increased until a situation indicated by figure 6.2c is realised. This process will be repeated until the formed region (conduction channel) "grows" to the interface between the insulator and top metal lyer. At this stage, a further increment of the external field would result in a burst of electrons injected into the vacuum. Since these electrons will not be trapped, the potential drop across the insulator will not be readjusted as before, the emitted current will flow freely. Since the conductivity of the channel has been increased, it follows that this current will increase dramatically whilst the external field remains applied. Thus, to reduce a current to a reasonable value, it is necessary to decrease the gap voltage of 2-3 kV. Finally, this process will lead to an energy band diagram of figure 6.3 [115]. It is also important to note that the hot electrons produced by the above cyclic process could possibly acquire a lucky drift [116], and possibly escape into vacuum [117]. However, this would not correspond to a steady conduction, so that it would be difficult to determine how many "lucky" electrons exist. This could

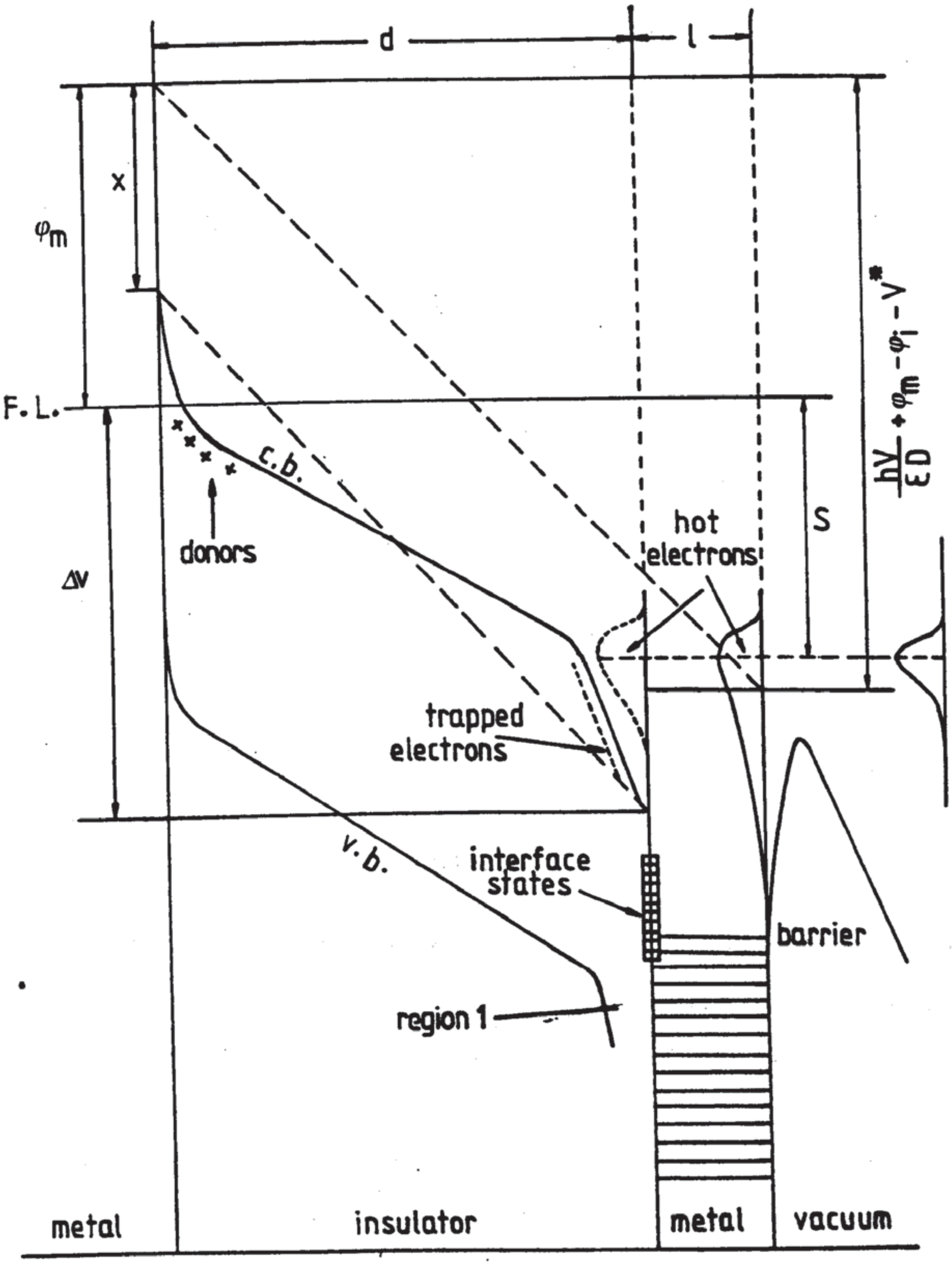

Fig. 6.3 The energy band diagram of a "on" state conduction channel associated with an MIM microstructure.

explain why we usually observe a very unstable I-V characteristic during the switch-on process (see figure 5.3).

This model utilizes most of ideas of the filament model proposed by Dearnaley [59]. However, as a developement, it gives an interpretation of the energy band diagram. Furthermore, it overcomes the difficulties of the earlier model in explaining the permanent change in the conductivity of a conduction channel and the lack of experimental evidence of a re-switch on phenomenon. However, the type of conduction channel proposed by this model could be "poisoned" if the pressure of the vacuum chamber is too high; e.g. > 10^{-8}mbar where the concentration of oxygen molecules in the air may be high, as has been observed in MIM devices. A "poisoned" channel will have a low conductivity and may even relax back to the previous state. In addition, this model also overcomes the difficulty of the switch-on model of Athwal et al [26], which had to assume an unlikely electron energy (i.e., > 5 eV) for initiating an avalanch process.

6.2.3. Generation of hot electrons

It is still assumed, as with the earlier model [9], that the spectral peak is at the energy position that corresponds to the "knee" of the conduction band bottom in the vicinity (region 1) of the interface between the insulator and the top metal layer. It follows from figure 6.3 that the voltage dropped across the bulk of the insulator is approximately equal to the spectral shift as measured from the cathode Fermi level to the spectral peak; however, as discussed elsewhere [32] most of the voltage dropped across the insulator will be in the two interface regions. For example, the voltage across the interface region 1 can be calculated in a way similar to that suggested by Bayliss et al [9]; i.e.

$$\Delta V = \frac{h}{d}\,\frac{V_o}{D}\,\frac{d}{\epsilon} + \chi - \varphi_i - S - V^{*} \qquad (6.1)$$

where V_o is the applied gap-voltage and the other parameters are as previously defined. It should be noted that on the right hand side of the equation, the first term has been appropriately changed to represent the new emission regime and h/d has been taken as the approximate field enhancement factor.

It is, therefore, possible to estimate the value of the electric field in the most important region of the emssion regime, and accordingly to judge, with the help of the existing theoretical and experimental results already described in chapter 3, what sort of the electron-phonon interaction mechanism may be involved. Thus, assuming that the thickness of the insulating layer is 10^{-7}m, and noting that the maximum spectral shift obtained from a typical spectral measurement, such as presented in figure 2.10, is ~1 eV, it follows that the electric field in the bulk of the insulator will be < 10 MV/m. Since this field value is much less than the threshold field for electron heating in the conduction band of SiO_2 recently measured by DiMaria et al [92], it can be assumed that the electrons will be "cooled" down by the interaction of electron-acoustic or electron-optical phonons. However, the electric field in the interface region 1 may be very high since, as can been seen from the band diagram, it is a strong accumulation region. In fact, the voltage drop across it has been estimated in the early model to be more than 20 V in the normal steady emitting state [32], so that under these conditions, the "effective" thickness of the region may be expected to be approximately equal to the Debye length L_b as indicated by [118]. Thus, with $L_b = [K_bT/e^2(N_b+P_b)]^{1/2}$, where N_b and P_b are the bulk electron and hole density respectively, and taking $\epsilon = 4$ and $(N_b + P_b)$

= 10^{23} m^{-3} as a typical values, L_b will be ~ 3×10^{-8}m, so that the electrical field could be as high as 6×10^{8}V/m if it is assumed that the voltage across the region is ~20 V. It follows, therefore, that hot electrons can be expected to be generated in this region. As predicted by Ridley [74] and Fischetti [75], it can now be assumed that the dominant electron-phonon interaction is the acoustic mode, and also that the thickness of the accumulation region is approximately equal to the Debye length L_b within the range of the applied field. This latter approximation could be a very good one since it has been indicated [118] that, for a strong accumulation region, when $V \rightarrow \infty$, the thickness changes very slowly so that it is approximately equal to the L_b. Thus, the electric field in this region can be expressed in the form of

$$F_1 = \frac{\Delta V}{L_b}$$

$$= \frac{1}{L_b} \quad \frac{h}{d} \; \frac{V_o}{D} \; \frac{d}{\epsilon} + \chi - \varphi_i - S - V^* \qquad (6.2)$$

Also, according to the section 3.3.3.(iii), the hot electron temperture can be expressed in the form $T_e = XF_1$ which, from equation 6.2 above becomes

$$T_e = \frac{X}{L_b} \quad \frac{h}{d} \; \frac{V_o}{D} \; \frac{d}{\epsilon} + \chi - \varphi_i - S - V^* \qquad (6.3)$$

This is an important relation and will be used in the following section.

6.2.4. Hot electron emission into vacuum following coherent scattering

It follows from the above discussion that the hot electrons generated in the interface region will attempt to escape into the vacuum. However, as discussed by Simmons et al [8], they will be coherently scattered in the top metallic layer and that, unless they have sufficient energy, determined by the Bragg equation, will be back-scattered into the insulator. In fact, even when the electric field has been increased to the point where forward scattering is possible, such as in the direction 2 shown in figure 6.1b, an electron will not be able to escape into the vacuum if its path length in the top electrode is longer than its mean free path, i.e., 20-50 Å [120]. However, as discussed by Simmons et al [8], this restriction can be relaxed if a channel terminates at a position near to a triple-junction region such as shown in figure 6.1b.

Thus, electrons that are diffracted in a direction 2, and have a velocity vector parallel to the insulator-metal interface which is large enough for them to surmount the surface potential barrier of the metal, will be emitted into the vacuum and form an arc-like segment. Experimental evidence suggests that, in many cases, channels form in clusters in the triple-junction region, so that a typical image such as shown in figures 5.5 and 5.11, will consist of several segments. For the ideal situation where the properties of these channels, and their associated geometrical field enhancement, are the same, electrons associated with different segments in an image would be expected to have the same energy distribution. In practice, it is usually impossible to achieve the above conditions, so that the measured total energy distributions from the separate segments will be slightly different, as shown in figures 5.15 and 5.26. Furthermore, if the electron current is monochramatic, it would form a sharp arc-like segment; however, since electrons, in fact, have a finite energy distribution, the segment usually appears to be diffuse with an ill-defined trailing edge.

It follows from this reasoning that, with an increase in the electrical field, more and more electrons will have enough energy to emerge from the surface. Consequently, the overall size of a segment will increase, and accordingly its spectral half-width will be broadened, which is equivalent to saying that the effective electron temperature T_e has increased. This model also indicates that the orientation, size and position of the arc-like segments within an image will most likely depend upon the shape of the top metal layer and the positions of the channels.

With this idea in mind, it is possible to talk more about the multi-segment image. Thus, the image presented in figure 5.11b, could, for example, reflect the shape of the top metal layer, where figure 6.4b attempts to represent the microstructure at edges of the top electrode from which electrons are emitted. There are two possible ways in which electrons could be emitted from this structure and give rise to the image. Firstly, as illustrated in figure 6.4a, an array of the conduction channels could exist, where each gives rise to a cone of emitted electrons that have velocity componants in both directions 1 and 2. It then follows that the arc-segments on opposite sides of the probe hole (see figure 5.11b) that have the same curvature may be considered to come from same conduction channel so that the shortest separation of the two arcs and the magnification of the imaging system can be used to estimate the width of the microstructure. Secondly, as illustrated in figure 6.4c, where it is again assumed that a cluster of conduction channels exist, electrons can only be emitted in one direction since, in the opposite direction, the length of the layer is longer than the electron mean free path. It follows that the width of the microstructure can be estimated from the separation of two central segments; i.e. (0.5 mm)/M for this particular image, where M is the total mignification of the imaging

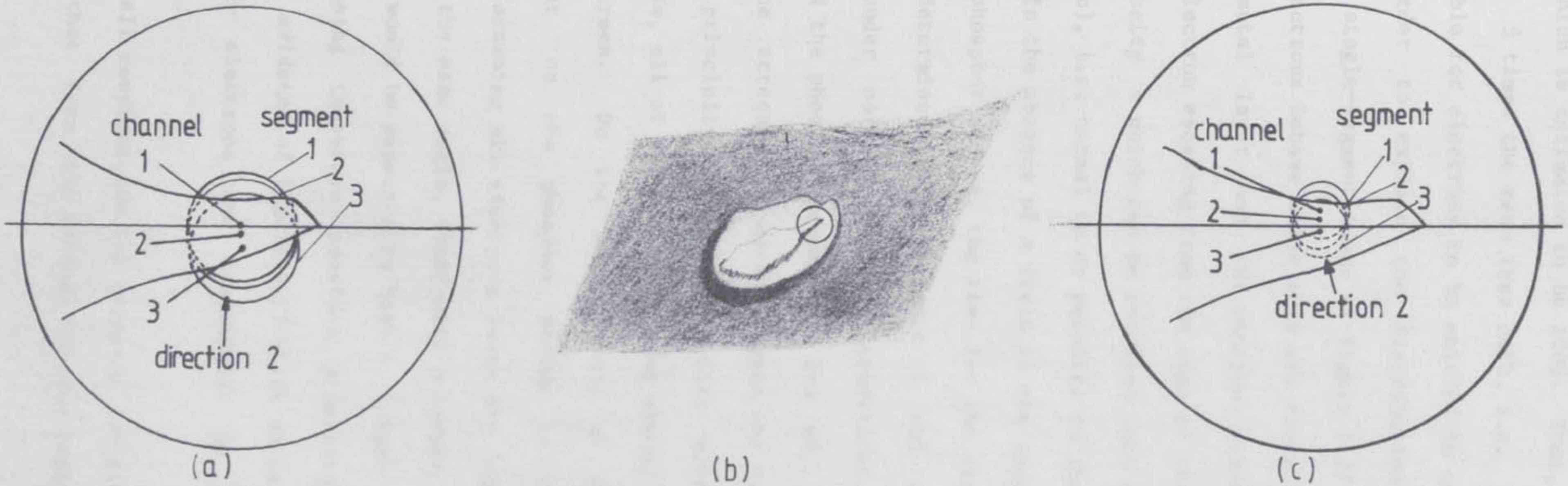

Fig. 6.4 The proposed topographitic feature of a top metal layer and conduction channel arrangement that may be associated with the emission image shown in figure 5.11b.

system, which is estimated to be 2000. Thus, the width is $\sim 2.5\times10^{-7}$ m which is 5 times the mean free path, i.e. 50 Å. Therefore, it is only possible for electrons to be emitted in one direction.

In order to explain the distribution of the spectral energy within the single-segment image of figure 5.27, we have to consider how the electrons behave while they are travelling between the edge of the top metal layer and the phosphor screen. Referring to figure 6.5a, an electron escaping from the edge of the top metal layer has a total velocity v which can be resolved into components $v_\perp$ and $v_\parallel$ (see figure 6.5b), i.e. normal to or parallel to the plane of the substrate surface. In the absence of a field in the space between the cathode and the phosphor screen, the time for the electrons to travel to the screen is determined by the distance L and $v_\perp$ (see figure 6.5a). However, under normal operating conditions, i.e. with the cathode earthed and the phosphor screen at 2-3 kV, an electron is swept towards the screen after escaping into the vacuum, where the transit time Δt is principlly determined by this accelerating voltage. In other words, all of the electrons take almost the same time to arrive at the screen. On the other hand, $v_\parallel$ determines the lateral displacement on the phosphor screen in the time interval Δt. Therefore, assuming all electrons leave the edge of the top metal layer at the same angle, those with a larger $v_\parallel$, i.e.the high energy electrons, would be expected to have a larger lateral displacement. This reasoning therefore provides a qualitative explanation of the experimetal evidence of figure 5.27 which shows how the majority of high energy electrons are distributed in the convex edge of the segment.

We shall consider now the physical origin of the low energy electrons that form the diffuse concave region of the image. These

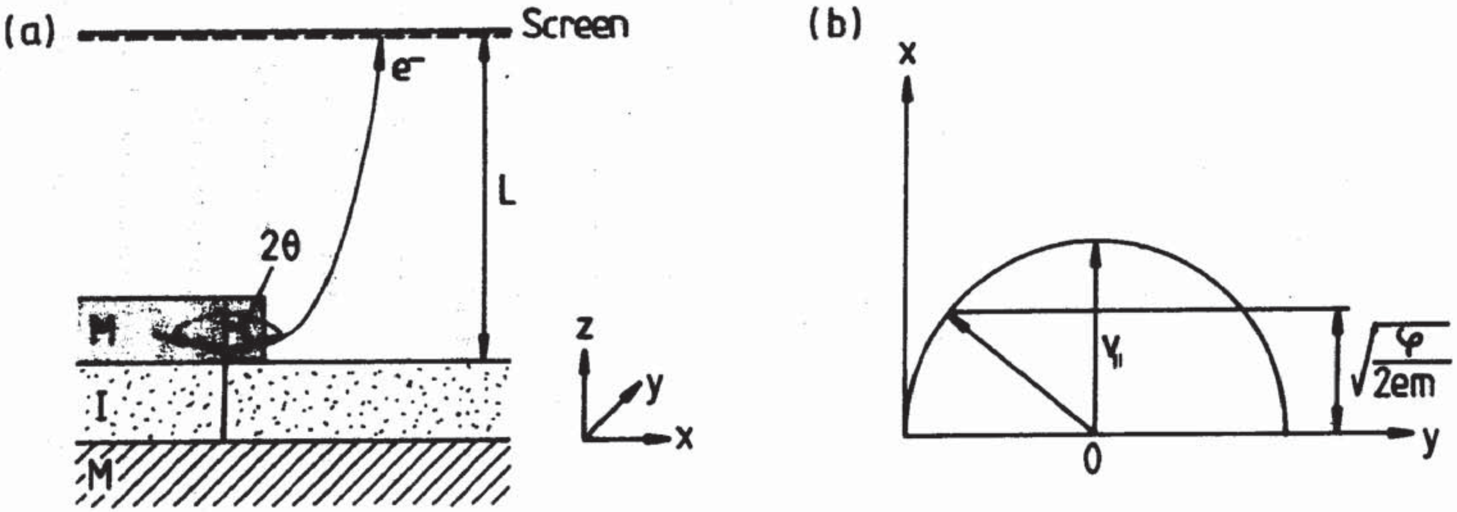

Fig. 6.5 A simplified imaging system.

are assumed to occuring from incoherent scattering processing in the top electrode. Thus there will be both high and low energy electrons that have undergone one or more scattering process, loosing several tens or hundreds of meV at each event. It follows from this reasoning, and the concept outlined in the previous paragraph, that these processes will lead to a transfer of electrons from the convex to the concave region of the image. This energy-selective analysis has therefore not only provided further support to the original emission model, but has also revealed the existence of an important associated process.

Associated with this "steady emitting state" of a MIM microstructure, there is apparently a negative charge effect in the top metal layer, since it is electrically "floating". Such a microstructure can in fact be considered as a leaky micro-capacitor, although it is very difficult to directly apply standard electrodynamic theory to accurately evaluate the magnitude of the charge residing in the top layer. In principle, however, an analogue model of such a capacitor would be as shown in figure 6.6, i.e. where the anode, cathode and top metal layer, which is inserted into between the anode and cathode, are considered as infinite metal planes. A calculation can be made, and it predicts that the magnitude of the charge will be proportional to the applied gap voltage, and have a rather complicated relationship with the thicknesses of the insulating and top metal layers, and with the conductivity and permittivity of the insulating layer.

It follows that the existence of these negative charges will change the field enhancement on the surface of the top metal layer and, hence, in the conduction channel. Since the increase in magnitude of the negative charges on the surface of the top metal layer results

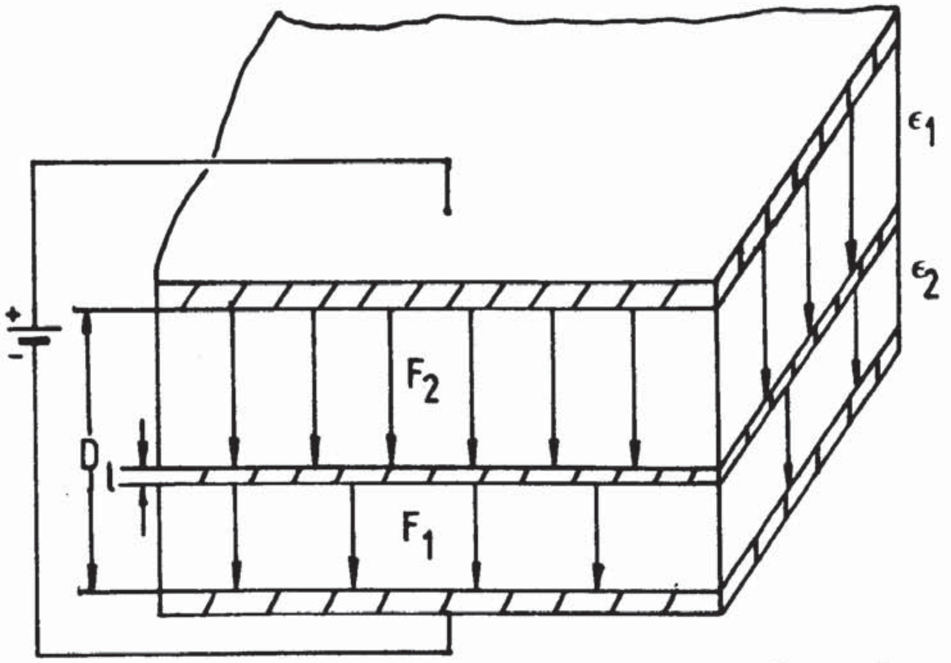

Fig. 6.6 A model capacitor analogure to test gap where there are MIM microstructures on the cathode surface.

in an increase in the number of field lines terminating at the surface, the local field increases; accordingly, the voltage drop across the anode and the top metal layer increases. However, since the potential difference between the anode and cathode remains constant, the voltage drop across the channel underneath the top metal layer will decrease. It is also noted that the increase in value of the former is equal to the decrease in value of the latter. Neverthless, a variation of the field enhancement within a range of fields of 1-2 kV, with which a measurements were usually carried out, is likely to be less than 2 times, since the number of negative charges, and hence, the local field, are proportional to the applied gap voltage. Therefore, it is unlikely that the local field increases to a high enough value to field-emit the electrons from states near or below the Fermi level of the top metal layer.

Another effect associated with the negative charges is related to the attractive force P_f between the anode and the top metal layer. We may assume that this force will have the same form as that for the parallel plane capacitor; namely, $P_f = Q^2/2\epsilon A$, where Q is the total surface charges, A the area of the planes and ϵ the dielectric constant, so that as Q increases, P_f increases. In some cases, for example an artificial carbon site which is not strongly ahering to the electrode surface, P_f can be bigger than the force making a particle ahere to the surface, so that the particle can be pulled off; this will be especially true when the electrode surface is set vertical. In fact, artificial carbon particles have been found to disappear from time to time during measurements. After a particle flies away, the emission image disappears or becomes very faint, and the current decreases if the voltage remains the same. On the other hand, emission images consisting of diffuse spots would appear after increasing the voltage to a certain value; i.e. it seems that the conduction channels in the insulating medium remain "on". However, it is possible that the site disappears completely since the insulating medium is possibly "taken" away by the metal layer. It is also noted that during the thermal stimulation measurement, this effect is even more obvious.

6.2.5. The energy distribution

From the above qualitative model, it could be anticipated that an electron spectrum would be composed by two components; i.e., consisting of both coherently and incoherently scattered electrons. As a result of incoherent scattering processes, the electron energy distribution in the surface of the top metal layer is likely to be changed from that in the interface between the insulator and top metal layer, i.e., as illustrated in figure 6.3. In order to obtain the form of this electron energy distribution, it is necessary to know the density of the electron states and the distribution function f_e. Since the electrons we are concerned with are essentially "free" in the metal, the density of states can still be expressed as that formulated by the Free Electron theory. However, there is not a suitable distribution function that is widely accepted for describing hot electrons: thus Ning [117] has suggested that they should be described by the Maxwellian function, whilst Conwell [71] has used the symmetrical Boltzmann's distribution function. Here, we shall assume that the Boltzmann distribution function is valid in our case. It then follows that the emitted electron energy distribution derived by Bayliss et al [9], and described in section 3.2.3, can now be applied to the new experimental data provided some modifications are made that take account of our new theoretical considerations. In particular, the spectral half width FWHM can still be experssed in the following form:

$$f = \frac{2.328N - 1.303}{N - 1} K_b T \qquad (6.4)$$

which is accurate for $1.2 < N < 4$. Substituting equation 6.3 into the above expression results in the following

$$f = \frac{2.328N - 1.303}{N - 1} K_b \frac{X}{L_B} \frac{h}{d} \frac{V_o}{D} \frac{d}{\epsilon} + \chi - S - \varphi_i - V^* \qquad (6.5)$$

This equation may be simplified if the constant terms are expressed as

$$X/L_b = \alpha_1 , \quad \text{and} \quad B_1 = (hD/\epsilon), \quad G_1 = \alpha_1(\chi - \varphi_I - V^*)$$

and where one lets $N = 1.3$ as assumed by Bayliss et al [9], so that

$$f = 5.47 \text{ x } \alpha_1\{B_1V_o - S] + G_1 \qquad (6.6)$$

which is clearly a linear function of the variable $B_1V_o - S$. It is important to notice that the constant α_1 that was unknown in the earlier model, has here been related to the electronic parameters of the conduction channel.

6.2.6. The emission current density

It follows from the above discussion, that the expression for the emission current density of Murphy & Good [65] can be applied to our situation, as in the earlier FIHEE model; i.e.,

$$J = \frac{4\pi me}{h^3} \frac{\pi/N}{\sin(\pi/N)} K_b T^2 \exp\left[\frac{-(\varphi - b(F/a_1)^{1/2}}{K_B T}\right] \tag{6.7}$$

where all the parameters have been defined in section 3.2.3. Now, by substituting for T from (6.3) in the above equation, the density J can be expressed in the new form: i.e.,

$$J = \frac{4\pi me}{h^3} \frac{\pi/N}{\sin(\pi/N)} K_b \left\{\frac{X}{L_b} \quad \frac{h}{d} \frac{V_o}{D} \frac{d}{\epsilon} + \chi - \varphi_i - S\right\}^2$$

$$\times \exp\left[\frac{-[\varphi - b(F/a_1)]^{1/2}}{K_b\{\chi/L_b[(h/d)(V_o/D)d/ \quad + \chi - \varphi_i - S]\}}\right] \tag{6.8}$$

so that the emitted current I, defined as J A_e will be given by

$$I = 1.62 \times 10^{14} A_e \frac{\pi/N}{\sin\pi/N} [\alpha_1(B_1 V_o - S) + G_1]^2$$

$$\times \exp\left[\frac{-\{\varphi - b[B_1 V_o/(a_1 D)]^{1/2}\}}{\alpha_1[B_1 V_o - S] + G_1}\right] \tag{6.9}$$

which is in a form similar to that of the earlier model, except that the constant terms are newly defined.

This current is, of course, influenced by the electron transport processes in the insulator. Therefore, the transition from the contact-limited (for the low fields) to the bulk-limited (for the high fields) can still be expected provided the conditions where high densities of both donors and traps are satisfied. However, in the region of an I-V plot where the bulk conduction is dominant, one can expect to observe either a field-dependent I-V characteristic, where the Poole-Frenkel mechanism is operating, or the saturation of the emission current, where an optical phonon scattering mechanism is

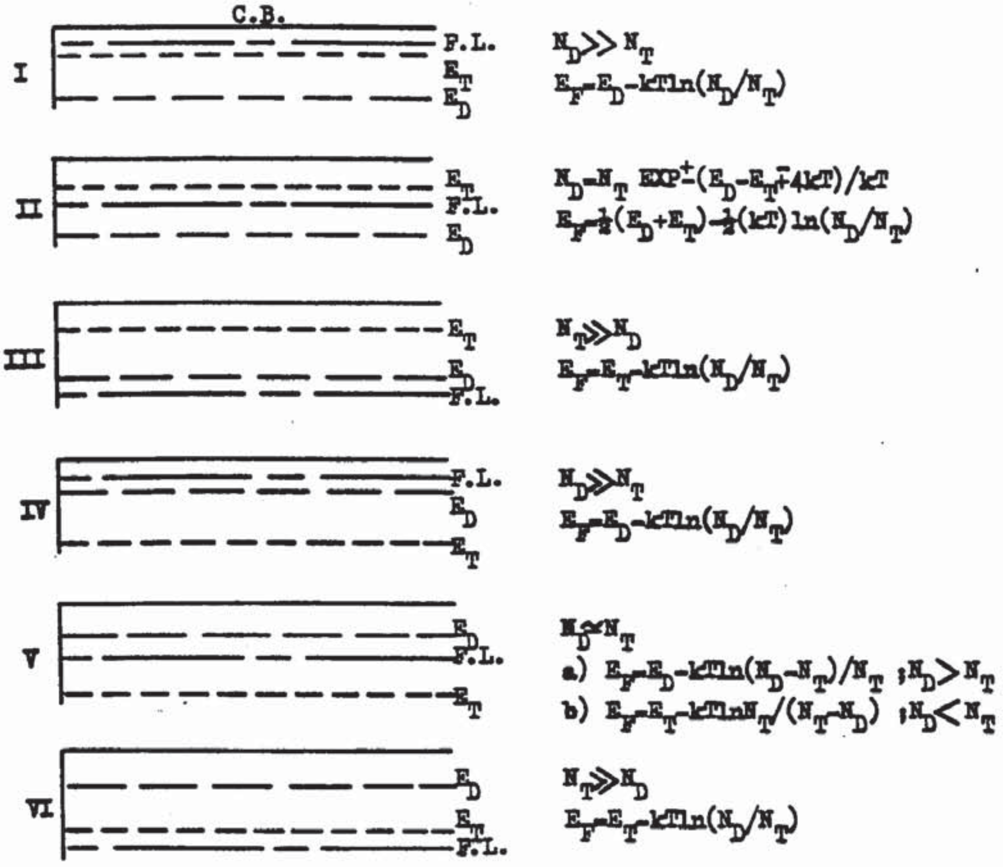

INSULATOR BAND MODELS.
The relationships between N_D,N_T and E_F alongside each diagram are the conditions for that particular energy configuration, assuming $n < N_T$ and non-degenerate positioning of E_F.

Fig. 6.7 The possible band structures proposed for MIM devices. (form Simmons [66]).

---

dominant. For a particular insulating layer, the question of whether the Poole-Frenkel mechanism or the optical phonon scattering process is dominant depends on the ratio of the donor density to the trap density, and also on the nature of the traps. Therefore, from among six possible band structures (figure 6.7) discussed by Simmons [66], those shown in III and V will give rise to a field-independent conductivity if the traps are assumed to be neutral. In this case, as predicted in section 3.3.3, the drift velocity of electrons will be field-independent, so that the current will become saturated when the LO-phonon scattering mechanism becomes dominant. This provides an explanation for the current saturation effect observed by Latham &

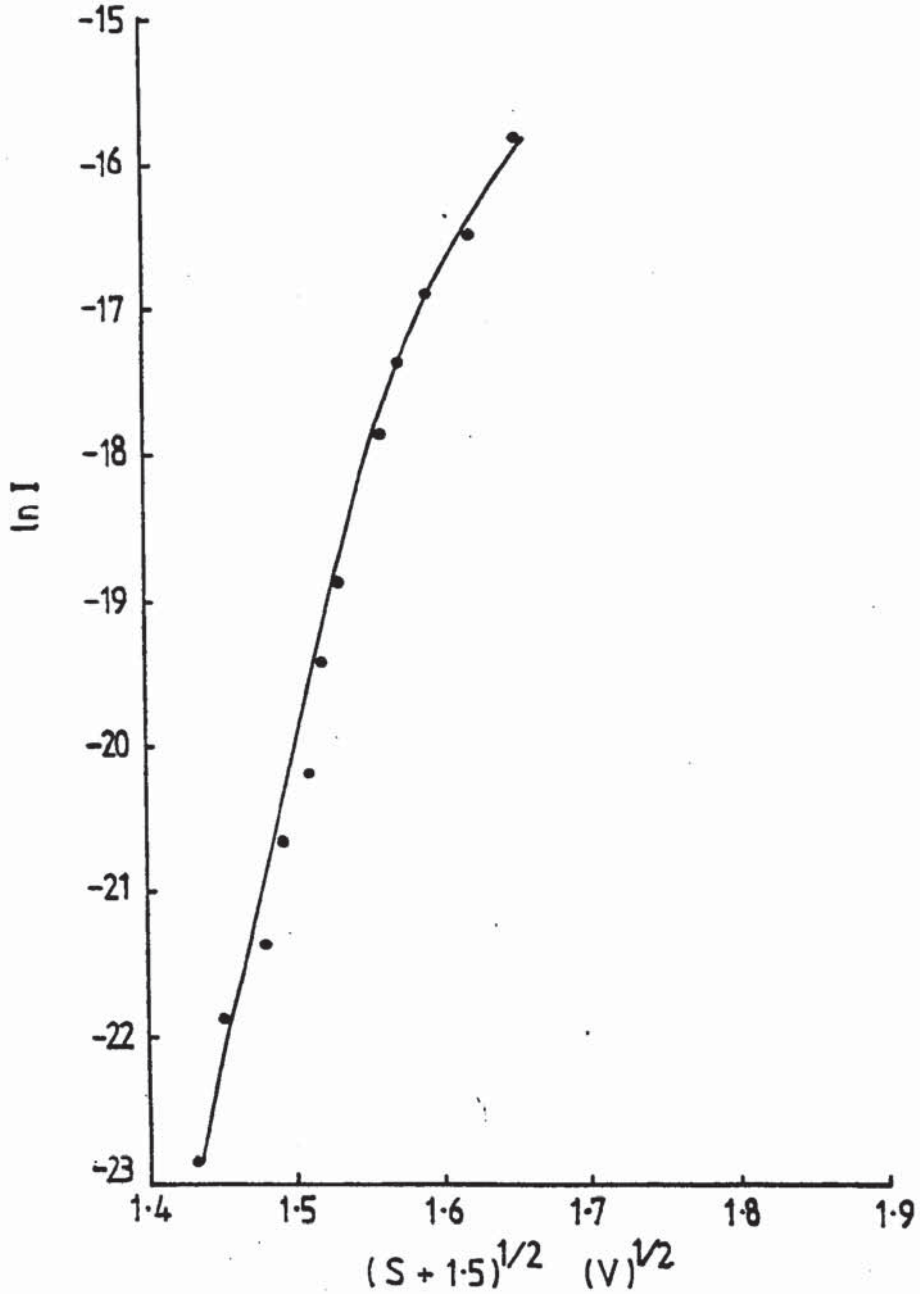

Fig. 6.8 The current-voltage characteristic of a typical artificial carbon site.(site 1).

Mousa [67] with their MIV regime.

6.3. The spectral data analysis

The spectral data described in chapter 5 can now be quantitatively analysed in terms of the above discussion. The construction of a lnI against $(S + \varphi_i - \chi)^{1/2}$ plot is straight forward provided that a value of $\varphi_i - \chi = 1.5$ eV is assumed. An optimum solution to equation 6, however, involves following the procedures suggested by Bayliss et

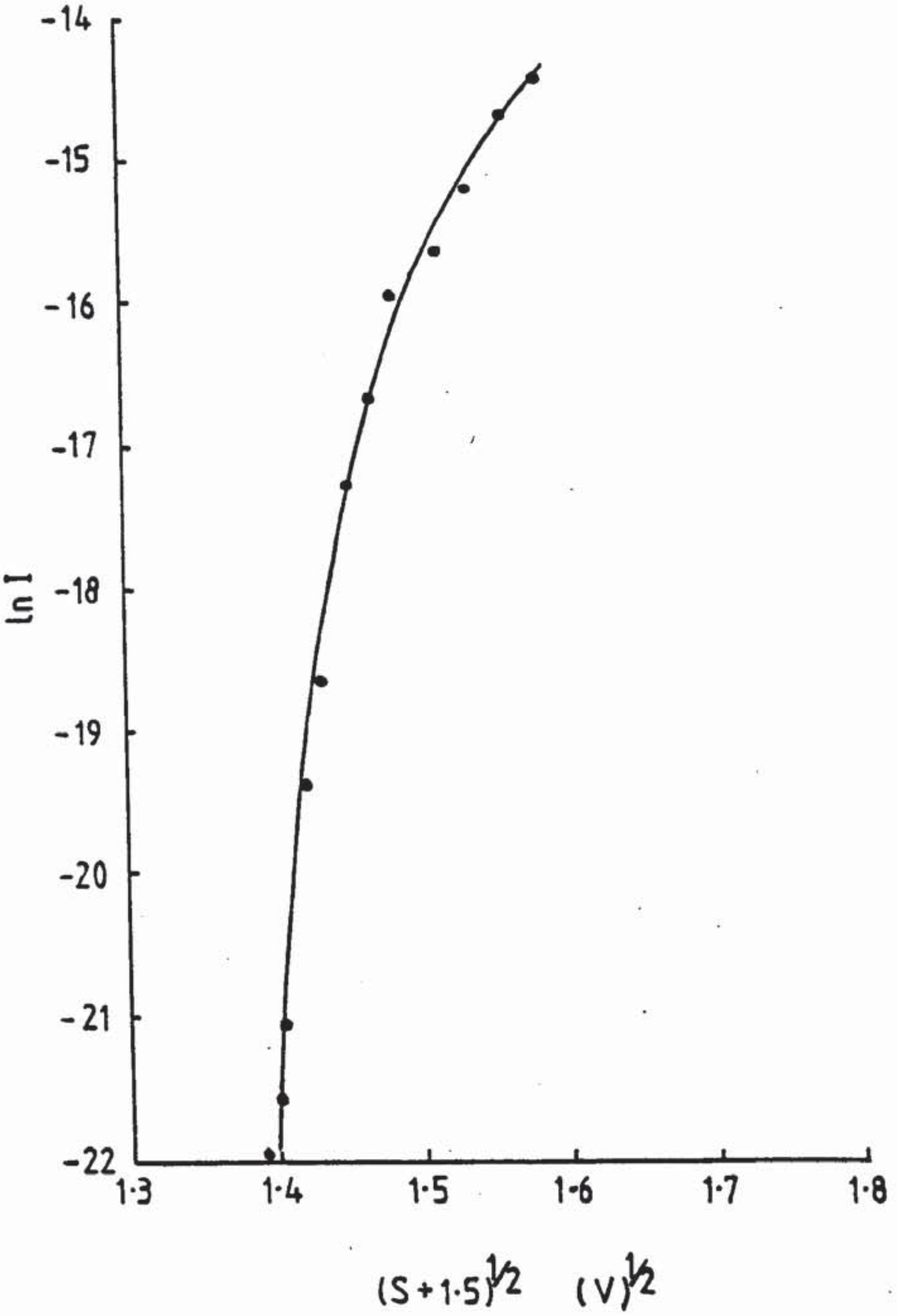

Fig. 6.9 The current-voltage characteristic of a typical type 2 natural site.(site 3).

al [9] with the use of a desk-top computer. Thus, a least-square fitting procedure is performed and a simple statistical regression coeffecient (R) is calculated for assumed values of B_1. Values of R will then range from -1 to +1 depending on the slope of the line; a perfect fit to the data is indicated if $|R| = 1$ for the optimized B_1 value, but R values exceeding 0.98 usually indicate acceptable

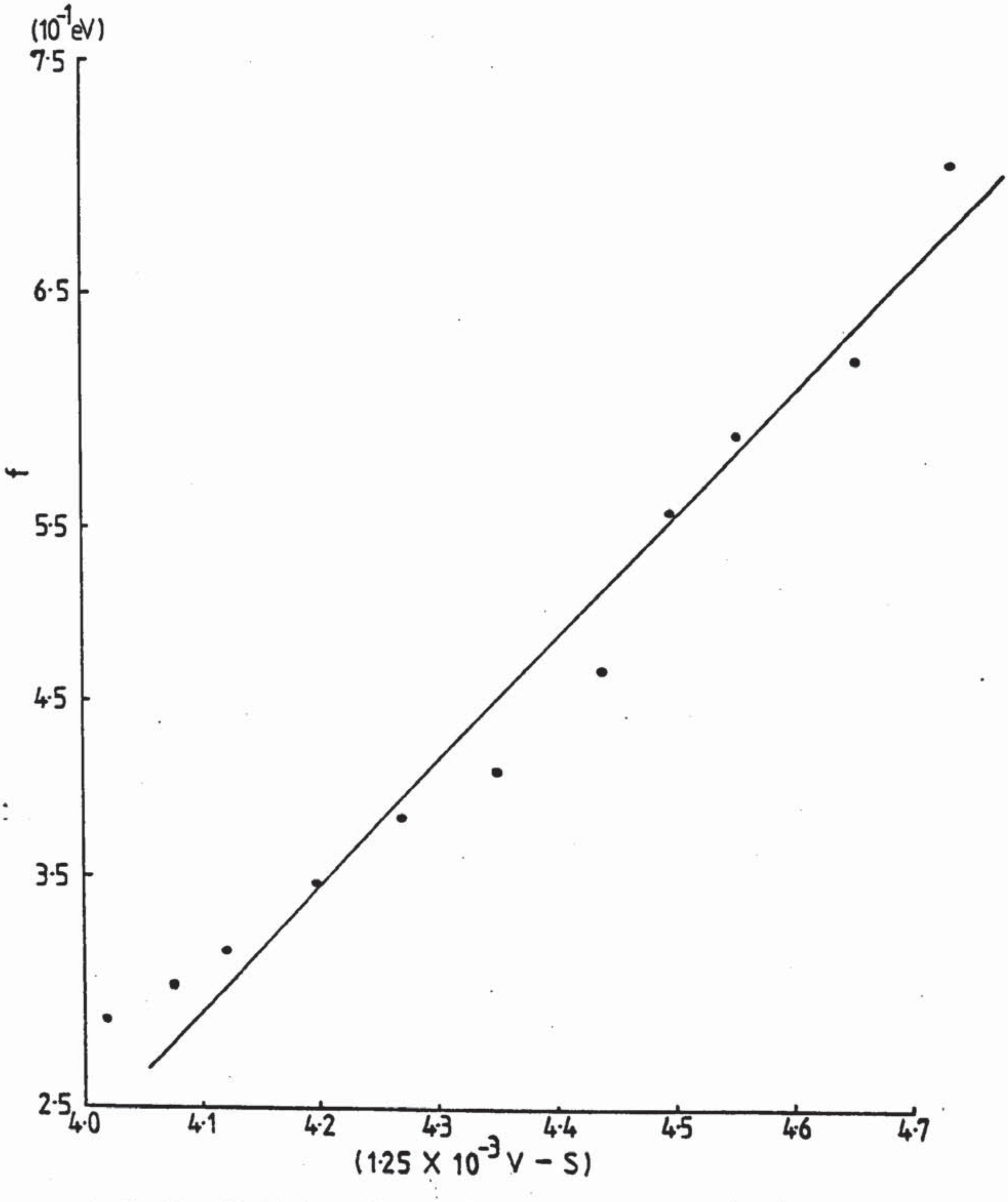

Fig. 6.10 The field-dependence of spectral half width of a typical artificial carbon site with the applied field.(site 1).

straight lines which then yield α_1 and G_1 as their slope and intercept values.

Two examples, illustrated by figures 6.9 and 6.11, are constructed from the spectral data of the type 2 natural site shown in figure

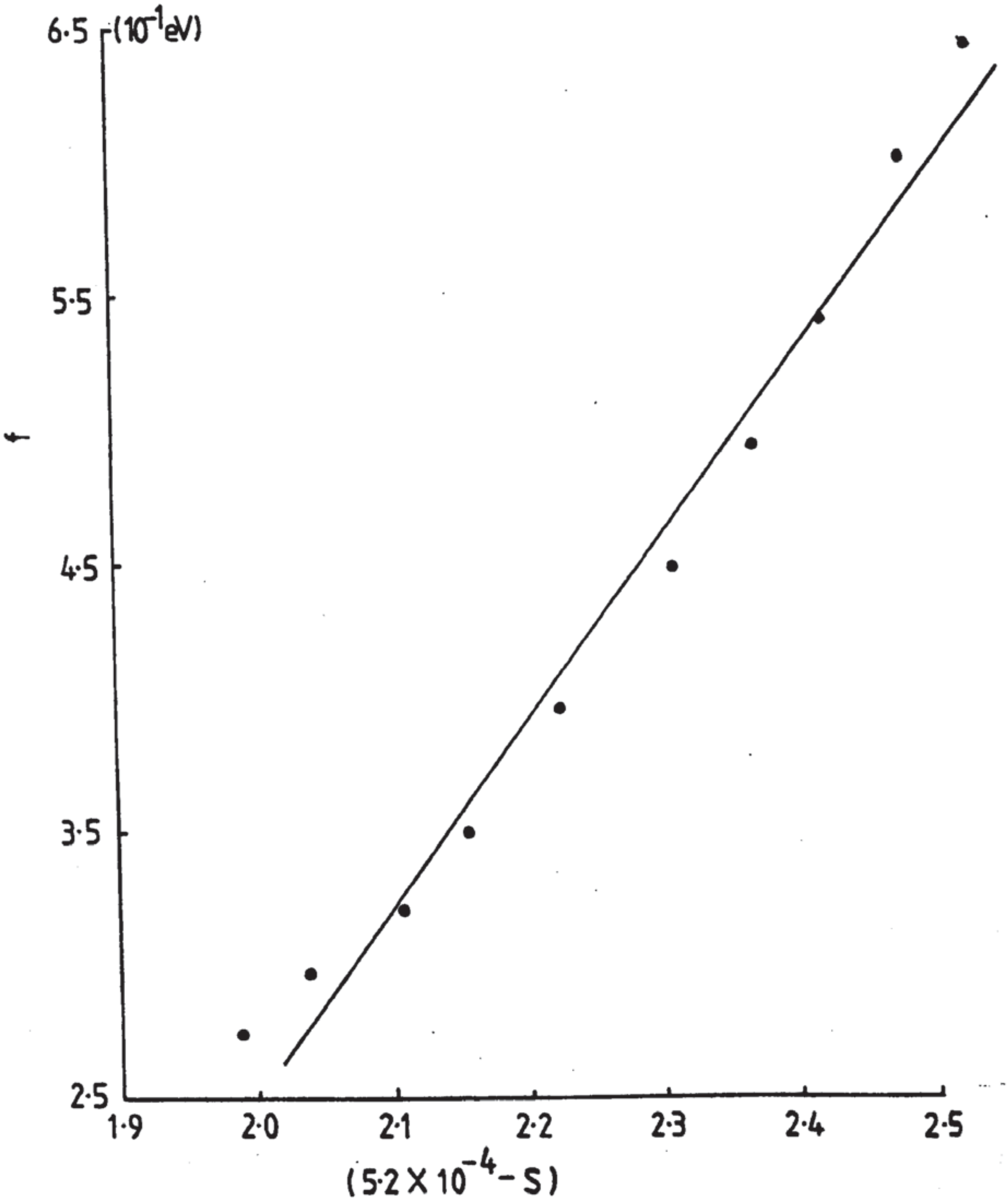

Fig. 6.11 The field-dependence of spectral half-width of a typical type 2 natural site with the field.(site 3).

5.12, whilst figure 6.8 and 6.10 are constructed from the artificial graphitic carbon site shown in figure 5.6. As can be seen, they have similar feature to those of Bayliss et al, described in section 3.2.3 and have the characteristics predicted by the analysis of section

6.2.4 and 5; i.e. a straight line for a plot of f versus (B_1V_o - S) and a curved line for the plot of lnI versus $(S + 1.5)^{1/2}$. However, the kink in a plot of f versus [B_1V_o - S] and the extended region of the plot of lnI versus $(S + 1.5)^{1/2}$ corresponding to complete bulk-limited conduction have not been revealed. This is not supprising, since the spectra have not indicated any obvious transition. This analysis therefore reinforces the reasoning of sections 6.2.3, 6.2.5 and 6.2.6.

6.4. The effect of the thermal and photo stimulation of emission

The model will now be used to explain the experimental results of the thermal and photo stimulation of emission described in sections 5.4 and 5.5.

Considering first the thermal stimulation of the emission current, it is apparent that at a constant field, more electrons will have the possibility of being emitted through the potential barriers at both the MI interface between the metal substrate and the insulator and the MV interface between the top metal electrode and the vacuum (i.e. due to Richardson-Schottky effect) when the specimen is heated above room temperature. As a further consequence of the increase of temperature, the carrier concentration in the insulator will increase since more electrons will acquire the necessary energy to escape from the trap centres into the conduction band. This will result in a decrease in the voltage drop across the insulator, and a modification of the MI barrier until an equilibrium state is achieved. The external result of these adjustments will be an increase in the emission current, i.e. as is found experimentally.

These same processes will also lead to the other variations in the electron energy spectra shown in figure 5.16 and 5.17. Firstly, the peak of a spectrum will be shifted towards the Fermi level as a result of the decrease in voltage-drop across the insulator. It will however be noted that in the range of temperature from 300 K to about 400 K, the spectra shows no obvious shift; i.e. apparently indicating that there are no trap centres in the energy regio between the bottom of conduction band and 0.1 eV below it. Secondly, the spectrum will become more symmetrical and the FWHM broadened as the cathode temperature increases the density of states function opposite the top of the vacuum potential barrier,i.e. as occurs in conventional thermionic emission.

We shall now consider three possible processes by which photons, under constant field conditions, conld stimulate the basic emission mechanism. (a) If the photons only penetrate a short distance into the top metal layer, they may be absorbed by electrons which will then have enough energy to surmount the surface potential barrier and so enhance the emission. It follows that this interaction will tend to charge the top metal electrode positively, thereby increasing the field across the insulator and hence the flux of electrons tunnelling from the metal substrate. (b) If the photons can penetrate to the bulk insulator region, they may stimulate the electrons from trap centres. However, unless this process occurs in the vicinity of the conduction channel, it is unlikely that stimulated electrons will significantly influence the emission current. (c) If the photons can penetrate through the insulating medium to the metal substrate, they will be able to enhance the emission current by either exciting photoelectric electrons from the metal substrate, or exciting electrons in the metal to higher energy levels so that more of them will be able to tunnel into the conduction band of the insulator. From the present experimental data it is not possible to say whether all or only one of the above mechanisms contribute to the effect shown in figure 5.21.

CHAPTER SEVEN

CONCLUSIONS

7.1. The principal experimental findings

In the previous chapters a wide range of experimental findings have been presented. These were obtained using a sophisticated UHV field emission electron spectrometer which was specially modified to provide an additional spatially-resolved electron energy selective display facility. The accumulated data reveals that the emission images of electrons field emitted from the prebreakdown emission sites can be divided into two types: type 1, which accounts for 70-80% of sites, is seen to consist of an apparently random distribution of diffuse spots, whilst the image of type 2 has a more geometrical form, consisting of several arc-like segments. Furthermore, the geometrical parameters of an arc-like segment of an image have been found to vary with the applied field: this has been confirmed by measurements made with the spatially-resolved energy-selective display technique. In particular, it has been established that the electron energy spectra of single segments are always single-peaked, and shifted below the Fermi level of the substrate electrode: furthermore, both the spectral shift and half width (FWHM) are field-dependent. Studies have also been made on artificial emission sites formed by depositing graphitic carbon particles on the ambiently or intentionally oxidised surfaces of broad-area electrodes. These sites have been shown to be strongly emissive, but more important, have characteristic emission images and energy spectra that are similar to those of type 2 natural sites described above. In addition, both natural and artificial sites have been found to be sensitive to thermal stimulation ($T < 400^{\circ}$ C) and external photons ($\lambda < 35$ Å).

It is particularly significant that type 2 images had not been previously identified in earlier studies of prebreakdown electron emission process from vacuum-insulated broad-area high-voltage electrodes. In fact, as will be summarised below, this new evidence has strongly challenged an existing field-induced hot electron model which had been shown to account for most of the previous experimental findings.

7.2. Theoretical considerations

A critical review has been given of the early FIHEE model, which highlighted its limitation. This included a discussion of the physical mechanisms by which hot electrons interact with phonons and how they are coherently scattered in a metal layer and subsequently led to a modified FIHEE model. This new model has been compared with its earlier version [9], and shown to have several special features.

(1) It can qualitatively explain the characteristic arc-like segmental appearance of the newly identified type 2 emission image.

(2) It offers a better qualitative "switch-on" model that is more consistent with the experimental observations.

(3) It provides a clearer physical picture of the interaction of electrons with phonons, and thus accounts for both the transport of electrons in the bulk of the insulator of a MIM microstructure and the generation of the hot electrons; two processes that were not really considered in the earlier model. As a result, it has predicted that, for certain energy band structures of a formed insulator, it should be possible to observe a saturation of the emission current.

(4) It broadly allows the application of most of the important equations of the early model to the new spectral data, since the qualitative analysis has suggested that the new emission regime has a similar physical basis; i.e., both models assume the existence of a dielectric medium in contact with the metal substrate. More important, new considerations have led to the conclusion that a

constant α_1 that was not identified in the early model, can be related to the electronic parameters of a conduction channel.

(5) Finally, this model has been supported by experimental evidence from the measurement of the thermal and photo stimulation of the emission.

7.3. Suggestions for future work

A follow-up programme to the present investigation would broadly concentrate on two main aspects. Firstly, it would implement and extend further improvements to the instrumentation in order to provide the possibility of more refined and versatile experiments, and secondly it would develop the present theoretical considerations with the aim of obtaining a more detailed understanding of the fundamental physical processes involved.

Thus, immediate progress could be made by obtaining more information about the coherent scattering process of hot elecrons. Here, the first interesting and very useful experiment would be to measure the spatial distribution of electrons of a given energy that form an image consisting of multiple arc-like segments. This would provide physical information about whether there is a relation between the energy and the geometrical parameters such as radius of the segments. A second experiment would be to analyse the spatial distribution of the current density of electrons of a given energy that form a single segment, in particular, to obtain more information about those electrons responsible for forming the ill-defined inner-edge of the segment. This would provide more information about the incoherently scattered electrons. However, before embarking on these investigations, it would be highly desirable to refine the electron energy-selective display system; in particular, there is a need to improve the data acquisition system. One way to achive this would be to replace the present storage oscilloscope by the combination of a commercial digital oscilloscope and a microcomputer system. With such a system, the data acquisition process would be carried on in more accurate and rapid way.

One other important objective of any future experimental investigation into the origin of the prebreakdown electron emission from broad-area electron would be to more precisely identify the local microscopic region from which electrons are emitted into vacuum. The present investigation has indicated that there could possibly be two emission regimes, viz. MIV and MIMV microstructures. In the latter case, the experimental evidence presented in previous chapter has suggested that in the MIM emission regime, electrons might be emitted into the vacuum from a triple junction at the edge of the top layer. To clarify this important aspect of the emission process, a high priority should be given to the development of a high resolution electron optical imaging technique for directly observing the topographic location of an emission site. It seems that a number of experiments carried out in situ with a scanning electron microscope [5,21], including the refined anode probe system of Niedermenn et al [6] have indicated that, with the commercial available resolution of such instruments, it is difficult to directly identify the precise point of emssion.

However, there is a possibility that the idea of using thermionic emission imaging to record sites, i.e. the experiment demonstrated by Latham et al [110], could be developed into a technique that would provide the required information. The limitation of the original version of the technique is that thermionic electron emssion has a low current density, so that there is a difficulty in imaging the emission current by using a phosphor screen. An alternative approach could be to use a photoelectric emission imaging system employing a high brightness commercial gas discharge ultra violet source: in fact, instrumentation for such a system has been constructed in the course of this programme although at present, it has not yet been commissioned. With such a facility, two additional experiments would be possible: The first would be a photo stimulation study, similar to that described in section 5.5, but where greater emphasis would be placed on measurements of the relaxation of hot electrons and the influence on their associated spectra. The second would be to display the spatial distribution of the hot electrons by using the energy-selective display system. Finally, it should be noted that, in fact, a similar approach has been successfully applied to studies of electron emission from thin films [112].

To complement such a future experimental programme, some theoretical work would be also necessary. Here, a particularly valuable study would be a Monte Carlo simulation of the electron energy distribution in the interface region between the insulator and the top metal layer. Following this, a further simulation could be undertaken of the energy distribution of those hot electrons which undergo the scattering processes (both coherent and incoherent process) in the top metal layer. For this latter study, it would be assumed that coherently scattered hot electron are emitted into vacuum without changing their distribution, while some of the incoherently scattered electrons could surmount the surface barrier and some of them are emitted into vacuum according to the Fowler-Nordheim tunnelling theory. It follows that in practice, these two components of the hot electrons will overlap and give rise to the measured electron energy distribution. The principal value of such an analysis is that it would provide a theoretical verification of the field-induced hot electron emission model. Finally, it should be observed that this theoretical work would not only be meaningful to the present type of study, but also to those working on MIM electron sources.

REFERENCES

1. Latham R V, "High voltage insulation: the physical basis", (Academic Press, London), (1981).

2. Noer R J, Appl. Phys. A (Germany), **A28**, No.1, 1-24, (1982).

3. Fowler R H & Nordheim L, Proc. Roy. Soc. **A119**, 173-81, (1928).

4. Chatterton P A, Proc. Phys. Soc. Lond. **88**, 231-245, (1966).

5. Athwal C S & Latham R V, Proc. IX-DEIV, Physica, **104C**, 46-49, (1981).

6. Niedermann P H, Sankaraman N and Fischer ø, Proc. Second Workshop on RF-Superconductivity, Geneva (Switzerland), (ed. H. Lengeler), 583-596, (1984).

7. Modinos A, "Field, thermionic, and secondary electron emission spectroscopy", (Plenum Press, New York and London), (1984).

8. Simmons J G, Verderber R R, Lytollis J, and Lomax R, Phys. Rev. Lett., **17**, No.13, 675-677, (1966).

9. Bayliss K H and Latham R V, Proc. Roy. Soc., London, **A403**, 285-311 (1986).

10. Millikan R A & Sawyer R A, Phys. Rev., **12**, 167-170, (1918).

11. Millikan R A & Lawitsen C C, Proc. Nat. Acad. Sci. (USA), **14**, 45-49, (1928).

12. Boyle W S, Kisliuk P & Germer L H, J. Appl. Phys., **26**, 720-725 (1955).

13. Little R P & Smith S T, J. Appl. Phys., **36**, 1502-1504, (1965).

14. Tomaschke H E & Alpert D, J. Vac. Sic. Tech., **4**, 192-198, (1967).

15. Little R P & Whitney W T, J. Appl. Phys., **34**, 2430-2432, (1963).

16. Powell H P S & Chatterton P A, Vacuum, **20**, 419-429, (1971). Pivovar L I & Gordienko V I, Sov. Phys.: Tech Phys., **7**, 908-912, (1963).

17. Pivonar L I & Gordienko V I, Sov. Phys.: Tech Phys., **7**, 908-912, (1963).

18. Cox B M, C.E.G.B. Laboratory Note R/M/N, 1021, (1979).

19. Hurley R E, J. Phys. D: Appl. Phys., **13**, 1121-1128, (1980).

20. Cox B M & Wort D E J, Vacuum, **22**, 453-455, (1972).

21. Cox B M, J. Phys. D: Appl. Phys., **8**, 2065-2073,(1975).

22. Hurley R E & Dooley P J, J.Phys. D: Appl. Phys., **10**, L195-L201, (1977).

23. Hurley R E & Dooley P J, Vacuum, **28**, 147-149, (1978).

24. Allen N K & Latham R V, J. Phys. D: Appl. Phys., **11**, L55-L57, (1977).

25. Athwal C S & Latham R V, Proc. IX-DEIV, Physica, **104CA**,189-195,(1981).

26. Athwal C S & Latham R V, J. Phys. D: Appl. Phys.,**17**, 1029-1043, (1984).

27. Niedermann P H, Ph.D. Thesis, Geneva University, Switzerland, (1986).

28. Klyarfell B N & Pokrovskaya-Soboleva A S, Sov. Phys., **15**, 149-152, (1970).

29. Alfrey G F & Taylor J B, Brit. J Appl. Phys, **6**, Suppl. 4, S44-s49, (1955).

30. Hurley R E, J. Phys. D: Appl. Phys., **12**, 2247-2252, (1979).

31. Bayliss K H & Latham R V, Vacuum, **35**, 211-217, (1985).

32. Bayliss K H, Ph.D. Thesis, Aston University, U K, (1984).

33. Athwal C S, Bayliss K H, Calder R & Latham R V, IEEE Trans. Plasma Sci., **PS-13**, 226, (1985).

34. Noer R J, Niedermann P H, Sankaraman N, Fischer ø, J. Appl. Phys., to be published, (1986).

35. Baker F S, Holber A R and Williams J, Nature, **239**, 96-97, (1972).

36. Lea C, J. Phys. D: Appl. Phys., **6**, 1105-1114, (1973).

37. Latham R V & Wilson D A, J. Phys.E: Sci. Instrum, **15**, 1083-92, (1982).

38. Latham R V & Wilson D A, J. Phys. D: Appl. Phys., **16**, 455-63, (1983).

39. Erikson G F & Mace P N, Rev. Sci . Instrum., **54**, 586-90, (1983).

40. Hurley R E, Private communication, (1978).

41. Castle J E, J. Vac. Sci. Technol. A1 (2), (1983).

42. Zharinov V P et al, Phys. Met. Metall., **52**, No.1, 123-7, (1981).

43. Good R H & Müller E W, "Handbuck der Physik" (Springer-Verlag, Berlin), **21**, 176-231, (1956).

44. Van Oostrom A G J, Philips Res. Reports Suppl. No. 1, (1966).

45. Schottky W, Physik. Z., **14**, 63, (1923).

46. Miller H C, J. Franklin Inst., **282**, 382-8, (1966).

47. Miller H C, J. Franklin Inst., **289**, 347-51, (1969).

48. Gadzuk L W & Plummer EW, Rev. Mod. Phys., **45**, 487-548, (1973).

49. Young R D, Phys. Rev., **113**, 110-114, (1959).

50. Müller E W, Z. phys., **106**, 541-550, (1937).

51. Dyke W P & Dolan W W, Field emission, in Advances in Electronics and Electron Physics, **8**. Academic Press, (1956).

52. Gomer R, Field emission and field ionization, Cambridge, Massachusetts, Harvard University Press, (1961).

53. Müller E W, J. Appl. Phys., **26**, 732-737, (1955).

54. Ehrlich C D & Plummer E W, Phys. Rev. B, **18**, 3767-3771, (1978).

55. Hurley R E, J. Phys. D: Appl. Phys., **12**, 2229-2245, (1978).

56. Halbritter J, Appl. Phys. **A 39**, 49-57, (1986).

57. Allen N K, Ph.D Thesis, Aston University U K, (1979).

58. Athwal C S, Ph.D Thesis, Aston University U K, (1981).

59. Dearnaley G, Stoneham A M & Morgon D V, Rep. Prog. Phys., **33**, 1129-91, (1970).

60. Hickmott T W, J. Appl. Phys., **37**, 4380-8, (1966).

61. Dearnaley G, Thin Solid Films, **3**, 161-4, (1969).

62. Halbritter J, IEEE Trans. EI-**18**, 204, (1983).

63. Simmons J G & Verderber R R, Pro. Roy. Soc. A.**301**, 77-102, (1967).

64. Simmons J G, J. Phys. D: Appl. Phys., **4**, 613-657, (1971).

65. Murphy E L & Good R H, Phys. Rev., **102**, 1464-1473, (1956).

66. Simmons J G, Phys. Rev., **166**, No.3, 912-920, (1968).

67. Latham R V & Mousa M S, J. Phys. D: Appl. Phys., **19**, 699-713, (1986).

68. Halbritter J, Private communication, (1985).

69. Reggiani L, Topics in Applied Physics, **58**, (1985).

70. Kittel C., Quantum Theory of Solids, (Wiley, New York), (1983).

71. Conwell E M, High Field Transport in Semiconductors, (1967).

72. Ridley B K, Quantum Theory of Semiconductors, (1982).

73. Fröhlich H, Proc. R. Soc. London, Ser. A **160**, 230 (1937); **172**, 94 (1939); Adv. Phys., **3** 325 (1954).

74. Ridley B K, J. Appl. Phys. **46**, 998 (1975).

75. Fischetti M V, DiMaria D J, Brorson SD, Theis TN and Kirtley J R, Phys. Rev. B, **31**, 8124-8142, (1985).

76. Harrison W A, Phys. Rev. **104**, 1281, (1956).

77. Callen H B, Phys. Rev., **76**, 1394 (1949).

78. Ziman J M, Principles of the Theory of Solids (Cambridge University. Press, Cambridge) 205, (1972).

79. Shockley W "Electrons and Holes in Semiconductors" (Van Nostrand, Princeton, New Jersey), (1950).

80. Mead C A, J. Appl. Phys., **32**, 642-52, (1961).

81. Mead C A, Phys. Rev. Letters, **8**, NO.2, 56-7, (1962).

82. Cohen J, J. Appl. Phys., **33**, 1999-2000, (1962).

83. Cohen J, Appl. Phys. Letters, **1**, 61-2, (1962).

84. Kanter H & Feibelman W A, J. Appl. Phys., **33**, 3580-8, (1962).

85. Collins R E & Davies L W, Solid-State Electronics, **7**, 445-53, (1964).

86. Nelson OL & Anderson D E, J. Appl. Phys., **37**, 66-76 (1966).

87. Verderber R R & Simmons J G, The Radio and Electronic Engineer, 347-351, (1967). Phys. Rev. Letters, **17**, No. 13, 675-7, (1966).

88. Simmons J G & Verderber R R, Appl. Phys. Lett, **10**, No. 7, 197-199,(1967).

89. Gould R d & Collins R A, Appl. Phys. Lett., **16**, No.10, 393-395, (1970).

90. Gould R D & Hogarth C A, J. Phys. D: Appl. Phys., **8**, L92-L95, (1975).

91. Yankelevitch Yu B, Vacuum, **30**, No. 3, 97-107, (1979).

92. DiMaria D J, Theis T N, Kirtley J R, Pesavento F L Dong D W, & Brorson S D, J. Appl. Phys., **57**, No. 4, 1214-1238, (1985).

93. Purcell E M, Phys. Rev., **54**, 818-826, (1938).

94. Mousa M S, Ph. D. Thesis, Aston University, UK, (1985).

95. Brorson S D, Dimaria D J, Fischettic M V, Pesavento FL, Solomon & Dong D W, J. Appl. Phys., **58**, No.3, 1302-1313, (1985).

96. Kuyatt C E & Plummer E W, Rev. Sci., **43**, 108-111, (1972).

97. Braun E, Forbes R G, Pearson J, Pelmore J M & Latham R V, J.

Phys. E: Sci. Inst., **11**, 222-228, (1978).

98. Allen N K, Athwal C S & Latham R V, Vacuum, **32**, No. 6, 325-332, (1982).

99. Heddle D W O, Keesing R G W & Kurega J M, Proc. Roy. Soc. London, A **334**, 135-147 (1973).

100. Grivet P, Electron optics, 80-81, (1969).

101. Young R D & Kuyatt C E, Rev. Sci. Inst., **39**, 1477-1480, (1968).

102. Young R D & Muller E W, Phys. Rev. **113**, 115-120, (1959).

103. Klemperer O, Barnett M E, Electron optics, 3rd edition, Cambrige University Press, (1971).

104. Rogowski W, Archiv. Fur Elektrotechnik, **12**, 1-15, (1923).

105. Xu N S & Latham R V, J. de. Physique., **C2**, 67-72, (1986).

106. Xu N S & Latham R V, J. de. Physique, **C2**, 73-77, (1986).

107. Xu N S & Latham R V, J. Phys. P: Appl. Phys., **19**, 477-482, (1986).

108. Alpert D., Lee D A, Lyman E M & Tomasckke. J. Vac. Sci. Technol.,**1**, 35-50, (1964).

109. Jüttner B, Wolff H & Pech P, Proc. 8th Int. Conf. Phenom. Ionised Gases, 70, (1967).

110. Walters C S, Fox M W & Latham R V, J. Phys. D: Appl. Phys., 7, 911-919, (1974).

112. Blessing R & Pagnia H, Phys. Stat. Sol., (b) **110**, 537-542, (1982).

113. Latham R V, Vacuum, **32**, 137-140, (1982).

114. Xu N S & Latham R V, Proc. of 33rd IFES (Berlin), (1986).

115. Mott N F, Phil, Mag. **32**, 159-171, (1975).

116. Ridley B K, J. Phys. C: Solid state., **16**, 3373-3388, (1983).

117. Ning T H, Solid-State Electronics, **22**, 273-282, (1978).

118. Many A, Goldstein Y & Grover N S "Senmiconductor Surfaces". North Holland Publislis Ning Co., Amsterdum.

120. Kanter H, Phys. Rev. BI, 522, (1970).

ACKNOWLEDGEMENTS

This work would not have been possible without a grant from the government of the People´s Republic of China; accordingly, I would like to thank them. I would also like to thank the CVCP of the British Government for granting me an Oversea Research Student Award. In particular, I would like to thank my Supervisor, Dr R V Latham for many helpful discussions, and his constant encouragement during the course of the work. I would also like to thank my wife Dr Yini Chen for her help, support and encouragement. In addition, I would like to thank Mr A.P.O. Collis from EEV Ltd. for his assistance in ploting the potential distributions and electron trajectories, i.e. those presented in figures 4.15 and 5.22. Finally, I would like to record my appreciation of the opportunity to study at the University of Aston, and in particular, for the help I recieved from the technical service and personnel including, Messrs. H. Arrowsmith, A.E. Marriott-Reynolds and B. Lawrence, in the Department of Electrical & Electronic Engineering and Applied Physics.